REPORT DOCUMENTATION PAGE

Form Approved
OMB No. 0704-0188

1. REPORT DATE *(DD-MM-YYYY)*	2. REPORT TYPE	3. DATES COVERED *(From - To)*
08/31/2013	Final report	01-01-2009 until 08-31-2013

4. TITLE AND SUBTITLE
Final Report for ONR Award Number N00014-09-1-0549
Multi-Point Hermes Acoustic Modem for High-Speed, High-Frequency Acoustic Communications with Low-Frequency Acoustic Control Loop for Real-Time Transmission of AUV-Carried High-Resolution Images and Navigation Data in Support of Ship Hulls Inspection

5a. CONTRACT NUMBER
N/A

5b. GRANT NUMBER
N00014-09-1-0549

5c. PROGRAM ELEMENT NUMBER
N/A

6. AUTHOR(S)
Beaujean, Pierre-Philippe

5d. PROJECT NUMBER
N/A

5e. TASK NUMBER
N/A

5f. WORK UNIT NUMBER
N/A

7. PERFORMING ORGANIZATION NAME(S) AND ADDRESS(ES)
Florida Atlantic University – Department of Ocean and Mechanical Engineering
Building 36, 777 Glades Rd, Boca Raton FL 33431

8. PERFORMING ORGANIZATION REPORT NUMBER

9. SPONSORING/MONITORING AGENCY NAME(S) AND ADDRESS(ES)
Office of Naval Research
875 North Randolph Street
Arlington, VA 22203-1995

10. SPONSOR/MONITOR'S ACRONYM(S)
ONR

11. SPONSOR/MONITOR'S REPORT NUMBER(S)
N/A

12. DISTRIBUTION/AVAILABILITY STATEMENT
DISTRIBUTION STATEMENT A. Approved for public release; distribution is unlimited.

13. SUPPLEMENTARY NOTES
N/A

14. ABSTRACT
This final report provides the technical description and field performance of Hermes, a high-frequency underwater acoustic modem for high-bit rate data communications.

15. SUBJECT TERMS
Underwater, Acoustic, Modem, High-frequency, High bit rate.

16. SECURITY CLASSIFICATION OF:			17. LIMITATION OF ABSTRACT	18. NUMBER OF PAGES	19a. NAME OF RESPONSIBLE PERSON
a. REPORT	b. ABSTRACT	c. THIS PAGE			Pierre-Philippe Beaujean
U	U	U	UU	94	19b. TELEPHONE NUMBER *(Include area code)* (954) 924-7051

Final Report for ONR Award Number N00014-09-1-0549

Multi-Point Hermes Acoustic Modem for High-Speed, High-Frequency Acoustic Communications with Low-Frequency Acoustic Control Loop for Real-Time Transmission of AUV-Carried High-Resolution Images and Navigation Data in Support of Ship Hulls Inspection

High-Data Rate, High-Frequency Acoustic Communications with Acoustic Control Loop for Real-Time Transmission of ATR Images, Mosaics, Three-Dimensional Images and Vehicle Status Data in Support of Ship Hulls Inspection in Complex Areas

Dr. Pierre-Philippe Beaujean
Florida Atlantic University – Department of Ocean and Mechanical Engineering
Building 36, 777 Glades Rd, Boca Raton FL 33431
Phone: (561) 297-0530 Fax: (561) 297-3885 Email: pbeaujea@fau.edu

http://www.ome.fau.edu/center-of-acoustics-vibration

Table of Content

List of Figures

List of Tables

1. System Overview

The Hermes underwater acoustic modem consists of a topside component and an underwater (wetside) component. Together these components implement two underwater acoustic communication channels: a very high bit rate broadband data uplink and a low bit rate command downlink. Figure 1 contains the overall system block diagram for the acoustic communications link. Figure 2 and Figure 3 show the actual equipment.

1.1 Very high bit rate broadband data uplink

The very high bit rate broadband data uplink operates in the frequency band from 262.5 kHz to 375 kHz, and achieves true data rates of up to 87,768 kbps and a maximum range of 180 meters using a high power transducer (Jetasonic H320) or 130 meters using a small, low-power transducer (ITC-1089D). In this report, the low-power transducer is used. It tolerates Doppler-based motion up to 2 m/s. The uplink moves broadband multiplexed data from the wetside component to the topside component. The data originates from the AUV platform, its subsystems, and other sources. Data sources include cameras, sonars, pressure sensors, and serial port communications, as well as the modem's own status and performance metrics. On the wetside, digital source data samples are multiplexed, encoded into modem symbols and then modulated into digital modem samples. These digital modem samples are converted into analog modem signals and transmitted in one-way acoustic transmissions up the very high bit rate uplink. On the topside, acoustic modem signals are received from the very high bit rate uplink. The analog modem signals are filtered, sampled and down converted into digital modem samples. These samples are demodulated into modem symbols, and decoded into the digital data samples. The digital data samples are demultiplexed and displayed to the operator or distributed to other topside destinations.

1.2 Low bit rate command downlink

The low bit rate command downlink operates in the frequency band from 62 kHz to 87 kHz, and achieves true data rates of up to 4,223 bps. It tolerates Doppler-based motion up to 2 m/s and is designed to exceed the range of operation of the high bit rate acoustic uplink. The downlink moves low bit rate multiplexed data from the topside component to the wetside modem. The data originates from a topside user interface or other topside sources as command-and-control messages and configuration data for the AUV platform and its subsystems, including cameras, sonars and sensors, as well as the modem's own configuration data. On the topside, commands and modem configuration is multiplexed, encoded into modem symbols and then modulated into digital modem samples. These digital modem samples are converted into analog modem signals, and transmitted in one-way acoustic transmissions down the low bit rate downlink. On the wetside, acoustic modem signals are received from the low bit rate downlink. The analog modem signals are filtered, sampled, demodulated and decoded into the digital data samples. The digital data samples are demultiplexed and distributed to wetside recipients as commands and configuration data.

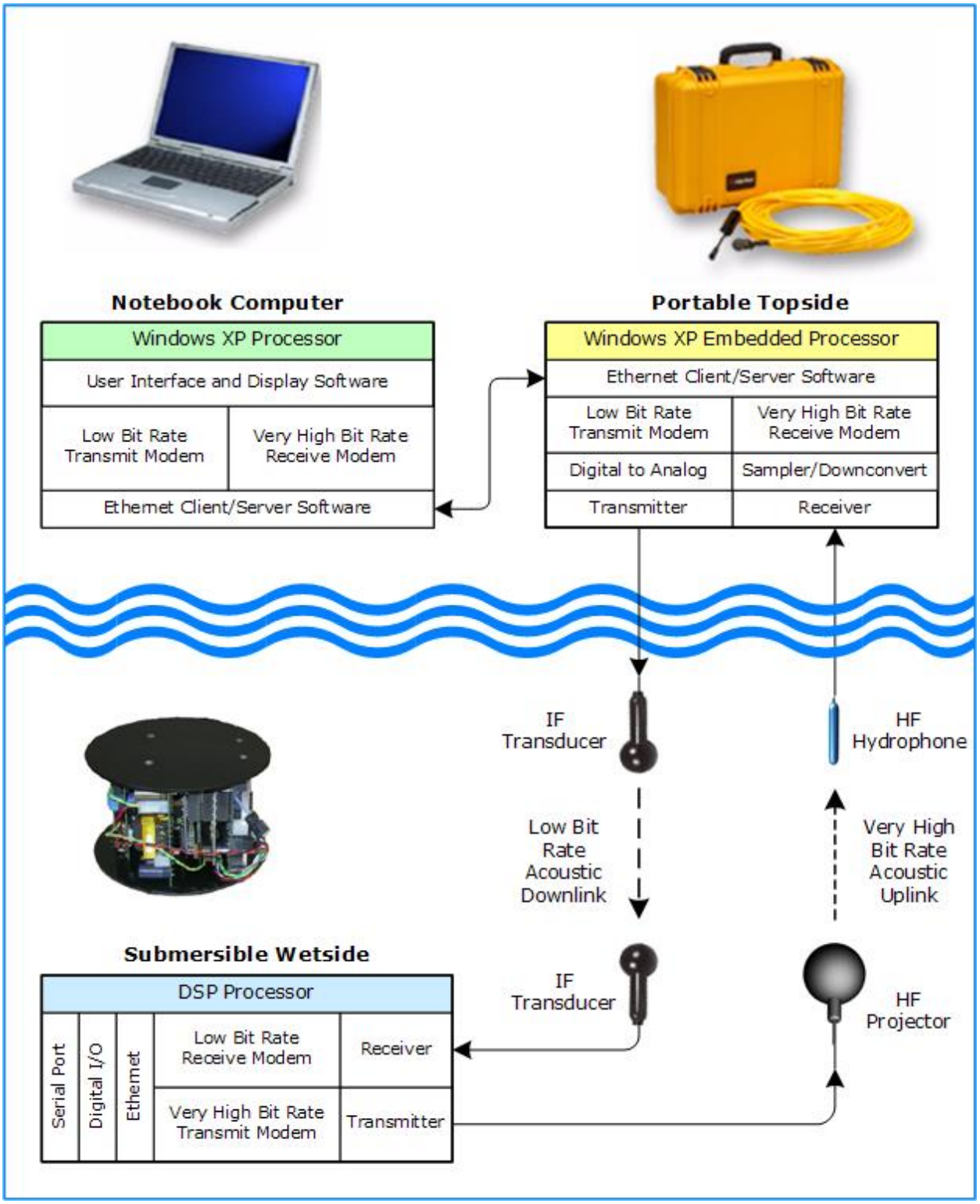

Figure 1: Acoustic communications system block diagram.

Figure 2: Acoustic communication system hardware (with the high-power source transducer Jetasonic H320).

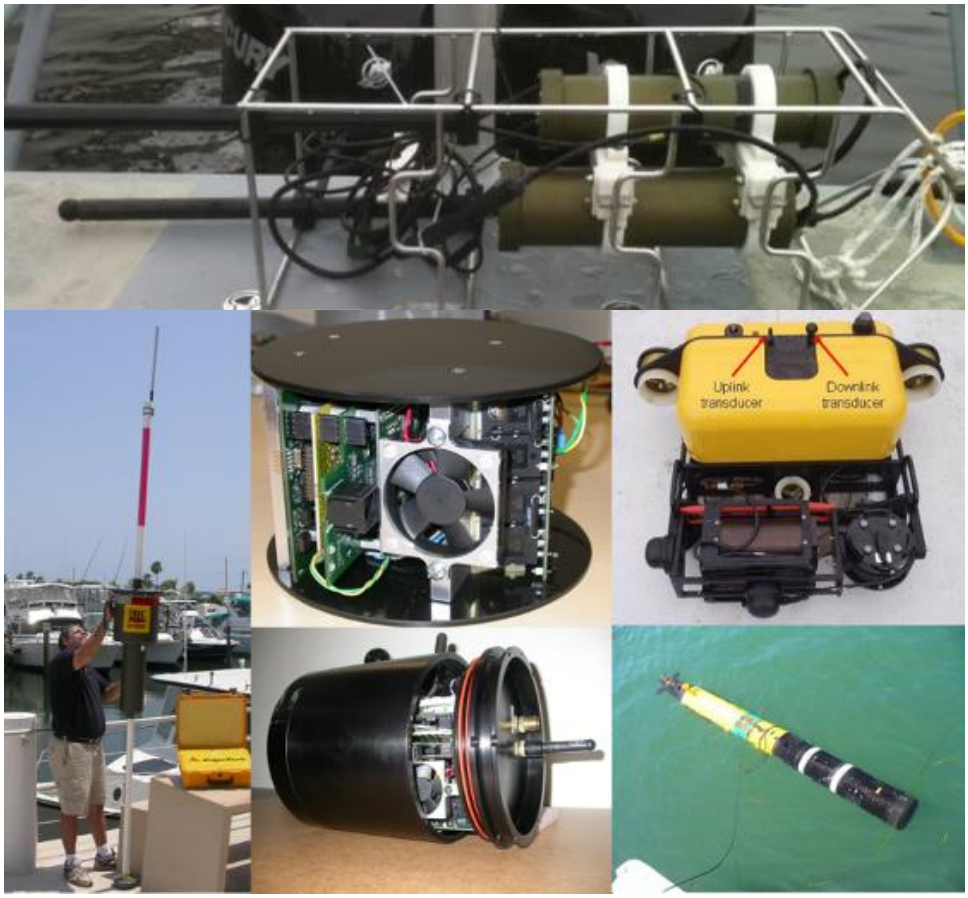

Figure 3: Topside receiver case and High-Frequency Acoustic Gateway (HAG) buoy (left); Hermes module for Bluefin Robotics HULS-3 (top center) and Remus-100 (bottom center); note that both modules are equipped with the small, low-power source transducer ITC 1089D; Bluefin Robotics HULS-3 (top right) and Remus-100 Gudgeon (bottom right), both equipped with Hermes.

1.3 Work Completed

The following is a review of the accomplishments over the period of performance (September 2009 until August 2013):

- Software and signal processing:
  - High bit-rate acoustic uplink:
    - A new, improved version of the Hermes acoustic uplink equalizer (Multi-scale DFE candidate selection process) was developed, which resulted in a significant reduction in the bit-error-rate during field experimentation and reduced processing requirements.
    - The MS-DFE equalizer was upgraded for parallel processing in real-time operations.
    - Various Doppler estimation software techniques (moving average and ARMA) were implemented, simulated and tested.
    - Hermes was upgraded to transmit and receive full-resolution sonar images containing ATR results, mosaic and vehicle status information simultaneously. The images originated from a Sound Metric Corporation (SMC) DIDSON unit installed on the Bluefin Robotics HULS-3 vehicle.

        - Hermes was upgraded to transmit and receive full-resolution Blueview sonar images and operate from a Remus-100 vehicle.
        - Hermes was upgraded to transmit and receive full-resolution sonar images containing ATR results, mosaic and vehicle status information simultaneously using the optimized status message format. The images originated from a Sound Metric Corporation (SMC) DIDSON unit installed on the Bluefin Robotics HULS-3 vehicle.
        - Hermes was upgraded to transmit and receive 3-D reconstruction images produced by the SeeByte software during Complex Area (CA) search operations.
    - Command-and-control acoustic downlink:
        - Hermes was upgraded to a closed loop communication system.
    - Single Input Multiple Output (SIMO) and Multiple Input Multiple Output (MIMO):
        - Single-Input Multiple-Output (SIMO) processing software was designed and implemented using the High-frequency Acoustic Gateway (HAG) buoys.
        - A Multiple-Input Multiple-Output (MIMO) algorithm was developed in collaboration with ISEN-Brest (France). This algorithm allowed the transmission of information from multiple Hermes uplink sources simultaneously. The process was tested with two sources and 3 receivers at the FAU SeaTech marina.
        - A time-varying channel response and Doppler spread estimation routine that used broadband PN sequences was developed and tested.
- AUV modules development:
    - Hermes was interfaced, tested and maintained on the Bluefin HULS-3 vehicle.
    - Hermes source package dedicated to the Woods Hole Oceanographic Institute (WHOI) Remus-100 unit was completed and tested at WHOI.
- Significant field tests:
    - High bit-rate acoustic uplink:
        - Hermes field-testing and demonstration in Norfolk, VA with Bluefin Robotics and SeeByte during October 2009. Real-time and simultaneous transmission of ATR images, mosaic images and vehicle status. Unfortunately, hurricane Ike limited the tests to an in-laboratory demonstration.
        - Hermes field-testing during hull inspection in Boston Harbor, MA with Bluefin Robotics and SeeByte during May 2010. Real-time and simultaneous transmission of ATR images, mosaic images and vehicle status. Transmission of control messages (to the vehicle and wetside modem unit).
        - Hermes field-testing during hull inspection (USNS Red Cloud) in Newport News, VA with Bluefin Robotics and SeeByte during June 2010. Real-time and simultaneous transmission of ATR images, mosaic images and vehicle status. Transmission of control messages (to the vehicle and wetside modem unit).
        - Hermes field-testing in Woods Hole, MA with WHOI during June 2010. Real-time transmission of Blueview sonar images from the Remus-100 Gudgeon.
        - Hermes field-testing at Battleship Cove, MA (Hiddensee) with the Complex Area (CA) team in December 2010. Real-time and simultaneous transmission of 2D ATR images and vehicle status in Non-Complex Area (NCA). Real-time and simultaneous transmission of 3D reconstruction images and vehicle status in CA area.
        - Hermes field-testing and demonstration in San Diego, CA (SS Curtiss) with the CA team in February 2011. Real-time and simultaneous transmission of 2D ATR images and vehicle status in NCA. Real-time and simultaneous transmission of 3D reconstruction images and vehicle status in CA.
        - Hermes field-testing at Battleship Cove, MA (Hiddensee) with the CA team in April 2011. Real-time and simultaneous transmission of 3D reconstruction images and vehicle status in CA.

- Hermes field-testing and demonstration at the Coast Guard Station in Boston, MA (Seneca) with CA team in April 2011. Real-time and simultaneous transmission of 2D ATR images and vehicle status in NCA. Real-time and simultaneous transmission of 3D reconstruction images and vehicle status in CA.
- Hermes field-testing and demonstration at NSWC in Panama City, FL (Bordelon) with the CA team in June 2011. Real-time and simultaneous transmission of 2D ATR images and vehicle status in NCA. Real-time and simultaneous transmission of 3D reconstruction images and vehicle status in CA.

- Periodical MIMO and SIMO experimentation in the FAU SeaTech marina and test tank.

2. Communication System

2.1 High Bit Rate Uplink

2.1.1 Source

The high data rate uplink operates between 262 kHz and 375 kHz in three sub-bands (Figure 4). The lower sub-band (262.5 kHz to 337.5 kHz) carries the binary information. The middle sub-band (347-373 kHz) is for detection purposes. The higher sub-band carries a narrow-band, 375 kHz tone designed to improve the Doppler-tracking capability of the high bit rate acoustic uplink. This acoustic uplink can operate at a maximum range of 180 m using an omni-directional source and a high-power omni-directional receiver Jetasonic H320. The source level required to achieve this range is 185.8 dB re 1µPa at 1 m, which corresponds to an acoustic power of 32 Watts. Using a small, low-power ITC-1089D and an input power of 16 Watts (Source Level of 180 dB re 1µPa at 1 m), the maximum range is 130 m. The downlink is designed for command-and-control and uses a lower frequency band (62-87 kHz) operated at the same source level but at a lower data rate.

The acoustic uplink uses either Binary Phase-Shift Keying (BPSK) or Quaternary Phase-Shift Keying (QPSK) modulation applied to symbols of adjustable bandwidth (25 kHz, 50 kHz or 75 kHz). The units presented in this document also use Bose-Chaudhuri-Hocquenghem (BCH) block error coding. The overall communication characteristics of the acoustic uplink are given in **Error! Reference source not found.**. The peak data rate is 87768 bits-per-second.

The acoustic uplink is designed to move multiplexed data from the wetside component to the topside component. The data typically originate from the various subsystems of the underwater platform (typically an AUV), such as high-resolution sonar, cameras, motion and pressure sensors. In addition, the wetside modem can relay its own status and performance metrics. The multiplexed information is encoded into modem symbols and then modulated into digital modem samples. These digital modem samples are converted into analog modem signals, and transmitted acoustically to the uplink receiver.

Wetside input data are received through serial ports, IP sockets (TCP, UDP) and digital input-output lines. A multiplexer is responsible for collecting data from all these input pipes and merging the data into individual packets suitable for transmission by the acoustic uplink. The multiplexer reads the input pipes using a weighted fair queue, taking data from each pipe's queue according to its priority. This allows the blocks from some pipes to be sent at a higher rate than others while ensuring that all pipes get to send.

Two input pipes are used here, one for Sound Metrics DIDSON sonar images and the other for vehicle status. The DIDSON pipe can include Wavelet Difference Reduction (WDR) compression and decompression if required. This third-party WDR compression technique is capable of 64-to-1 compression ratio.

The wetside unit is 150 mm in diameter and 76 mm tall. It fits inside the main pressure vessel of a Bluefin Robotics HAUV-1A or a Hydroid Remus-100 pressure vessel. The wetside unit can use a low-power, small source transducer (ITC-1089D) or a higher-power, larger transducer (Jetasonic H320). The receiver unit of the acoustic uplink use a single ITC-1089D. The input voltage of the unit is 18-36V and can be operated from the power bus of most AUVs. The unit accepts data via the Ethernet, serial port and digital lines. The wetside unit has been installed on the BlueFin Robotics HAUV-1. The active sensors installed on this underwater vehicle included one RDI DVL operating at 1.2 MHz and a Sound Metrics DIDSON operating at 1.8 MHz. With its carefully selected frequency range, the acoustic uplink is capable of operating without interfering with any of these sensors.

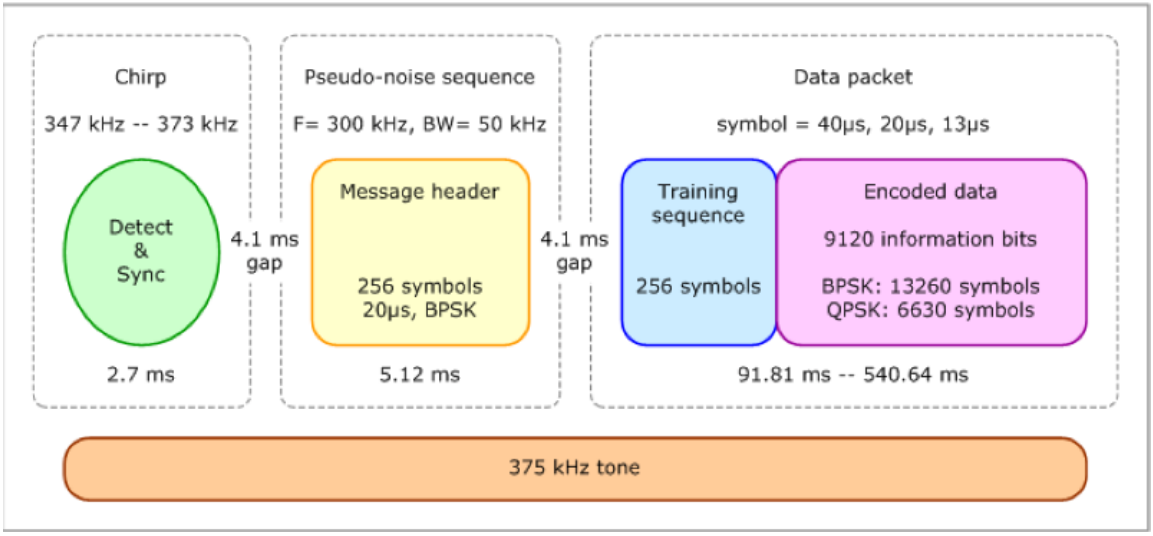

Figure 4: Individual message format for the high-rate acoustic uplink.

Table 1: Data packet specifications for the acoustic uplink.

Modulation Type	BPSK	BPSK	BPSK	QPSK	QPSK	QPSK
Symbol Duration	40 µs	20 µs	13 µs	40 µs	20 µs	13 µs
Symbol Bandwidth	25 kHz	50 kHz	75 kHz	25 kHz	50 kHz	75 kHz
Information bits/ frame	9120	9120	9120	9120	9120	9120
Packet duration (ms)	0.5491	0.2745	0.1830	0.2745	0.1373	0.0915
Message duration (s)	0.5615	0.2869	0.1954	0.2869	0.1497	0.1039
Information rate (bps)	16243	31784	46668	31784	60935	87768
Packet coded rate (bps)	25000	50000	75000	50000	100000	150000
Bits-per-Joule (bit/J)	2461.1	4815.8	7070.9	4815.8	9232.6	13298.2

2.2 Receiver

On the topside, the analog acoustic signals are filtered, sampled and down-converted into base-band (complex) digital modem samples. These samples are demodulated and decoded into digital data samples. The digital data samples are de-multiplexed and displayed to the operator or distributed to other topside destinations. The topside unit comes in the form of a single topside case equipped with a receiver hydrophone, equipped with analog-to-digital conversion electronics and a PC-type processor.

After topside reception and decoding, each packet is sent to a de-multiplexer, which is responsible for splitting the merged data and routing it to the correct output pipes. Data are handled in discrete, stand-alone blocks. Any packet that is received successfully contains all of the necessary information for each of the blocks it contains. A lost packet loses only those blocks it contains. The multiplexer treats each input block as a black-box and only knows the pipe identity, the path priority, the block type and the size of each individual data block (which may vary from block to block). The multiplexer packet header describes the path identity and offset of each block contained within the packet, allowing the topside de-multiplexer to extract each block and route it to the correct output pipe.

2.2.1 Receiver Signal Processing

A detailed description of the signal processing algorithm used to detect, authenticate, demodulate, equalize and error-check the incoming acoustic signals is available in the literature. Figure 5 shows a flowchart of the algorithm used to process an incoming acoustic message using a single receiver hydrophone, and to produce an output binary sequence.

The first issue to be addressed is the proper detection and authentication of an incoming message. A challenging aspect of the acoustic uplink is that each message can be transmitted immediately after the previous one. As a result, the transmission duty cycle can exceed 80%, which leaves very little time to estimate the background noise floor within the frequency band monitored by the receiver unit. In addition, the incoming message can use various types of modulation and frequency band, depending on the active configuration. Finally, the retrieval of the binary information contained in the packet is sensitive to time synchronization and frequency shifts.

Given these constraints, the uplink receiver process follows a series of initial steps, labeled (a) to (c) below, to accurately detect an incoming message and to identify the location and type of incoming data packet:

(a) The message trigger is a linear frequency-modulated chirp signal centered at 345 kHz with 26 kHz of bandwidth. A Blackman-Harris window is used to shape this chirp signal. The peak value of the cross-correlation between transmitted chirp and received signal is continuously monitored. The received signal contains only noise, unless a message is present. A trigger is deemed present if the signal-to-noise ratio (SNR) exceeds a detection threshold that can be dynamically adjusted based on the number of false alarms and slow changes of the noise power. The peak value of the cross-correlation corresponds to the beginning of the 2.7-ms message trigger, within the correlation's accuracy.

(b) The 5.12-ms preamble follows 4.1 ms later. This preamble contains the type of modulation (BPSK or QPSK) and symbol duration (40 μs, 20 μs or 13.3 μs) used in the data frame. The preamble uses direct-sequence spread spectrum (DSSS) to reduce the negative impact of fading. Three bits, used to code this information, are spread over 256 Gold-coded bits (Lin et al; 1983). As a result, the preamble can only contain one of eight pre-defined, 256 bit sequences. This pseudo-noise (PN) sequence is Gray-coded and BPSK-modulated at a carrier frequency of 300 kHz and using 50 kHz of bandwidth. Each symbol contains one bit (out of 256) and is shaped using a raised-cosine time window. As mentioned earlier, a 375 kHz tone is transmitted simultaneously, so that the average Doppler shift within the preamble can be estimated and compensated. The phase of each BPSK-modulated, Doppler-compensated symbol is estimated and the corresponding bit is retrieved. The identification process consists of matching the received binary PN-sequence with up to 1024 pre-defined binary sequences, with the understanding that only eight of these are valid. If the best match is one of these eight sequences, the detected signal is identified as a valid message, thus authenticated. The preamble correlation is also a mean to refine the estimated location of the packet following the preamble after a 4.1 ms dead time.

(c) Once the incoming message has been authenticated, the actual data packet is processed. A packet contains 9120 data bits plus 32 redundancy bits (CRC-32). The combined 9152 bits are block-coded, so that 4 parity bits are added to 11 data bits using a BCH(15,11,1) block code. A packet starts with a known 256-bit training sequence. The same modulation and symbol bandwidth is applied across the entire packet, which lasts between 103.9 ms and 561.5 ms depending on the modulation. Consequently, the data rate varies from 16243 bps to 87768 bps. In addition, a 375 kHz tone is transmitted simultaneously. The first processing step is the average Doppler shift compensation using the 375 kHz, tonal component. The second step consists of accurately estimating the starting location of the packet and demodulating the symbols. This is achieved using Minimum Mean-Square Error estimation (MMSE) of the incoming sequence. This operation relies on a Recursive Least-Square (RLS) algorithm.

At this stage of the process, an accurate estimate of the starting location of the packet has been found. The next step consists of demodulating the packet symbols. These symbols are distorted by noise, fading and inter-symbol interference (ISI), so that equalization is required to estimate the information content of the frame.

2.2.2 Decision Feedback Equalization

The high-rate uplink receiver uses a set of parallel Doppler-compensated Decision Feedback Equalizers combined with soft-decision BCH error correction routines. In a traditional approach, the DFE input is data vector $\mathbf{Z_{eq}}$, which comprises symbol vector $\mathbf{Z_{fr}}$ and decision vector $\mathbf{d_{fr}}$,

$$\mathbf{Z_{eq,n}} = \left[z_{fr,n}, \ldots, z_{fr,n+1-N_{eq,f}}, d_{fr,n-1}, \ldots, d_{fr,n-N_{eq,b}} \right]^T . \quad (1)$$

$N_{eq,f}$ represents the number of feed-forward taps, and $N_{eq,b}$ represents the number of feedback taps. The superscript ^{T} represents the vector transpose operator. Each filtered symbol at the output of the DFE is the product of $\mathbf{Z_{eq,n}}$ and the filter coefficient vector $\mathbf{C_{eq,n}}$ containing ($N_{eq,f}$ + $N_{eq,b}$) elements

$$r_{eq,n} = \mathbf{C}_{\mathbf{eq,n}}^H . \mathbf{Z_{eq,n}} . \quad (2)$$

H is the Hermitian operator. The elements $z_{fr,n}$ represent input complex symbols and $d_{fr,n}$ are the symbols obtained following a prior DFE decision made on earlier symbols. The subscript *fr* simply indicate that the symbol belongs to an information frame (or packet). $\mathbf{C_{eq,n}}$ minimizes the exponentially-weighted cumulative squared error between the equalized output $r_{eq,n}$ and the desired response

$$\varepsilon_{eq}^2 = \sum_{k=0}^{n} \lambda^{n-k} \left| r_{eq,k} - d_{fr,k} \right|^2 . \tag{3}$$

The parameter λ is known as the forgetting factor of the equalizer and controls the filter memory. This coefficient is positive and lower than 1. In the present case λ varies between 0.990 and 0.999. The solution $\mathbf{C_{eq,n}}$ that minimizes the cumulative squared error in is

$$\mathbf{C_{eq,n}} = \left(\sum_{k=0}^{n} \lambda^{n-k} \mathbf{Z_{eq,n}} . \mathbf{Z_{eq,n}^H} \right)^{-1} . \left(\sum_{k=0}^{n} \lambda^{n-k} \mathbf{Z_{eq,n}} . \mathbf{U_{fr}^H} \right). \tag{4}$$

This optimization problem is efficiently resolved using the least-squares lattice DFE algorithm covered in detail in the literature. The usual approach consists of using $N_{eq,f}$ feed-forward filter coefficients and a lower number $N_{eq,b}$ of feedback coefficients. A well-known limitation of the traditional DFE approach resides in the number of taps, due to processing burden and stability issues. A DFE is inherently an infinite impulse response filter with time-varying coefficients. The feedback filter coefficients are obtained following a non-linear decision process and can cause severe instabilities, especially if the number of feedback filter coefficients is large. This issue has been at the root of some extensive research and publications aimed at making the DFE process more stable while remaining computationally efficient. The work presented in this section falls in this category.

The channel impulse response is estimated by minimizing the mean-square error between a measured sequence of symbols and a reference. If the symbol duration is too long and the channel characteristics change too rapidly, the minimization process does not necessarily produce an optimal estimate of the channel response. Rather, different impulse response estimates may lead to very comparable mean-square errors. If sufficiently different, each estimate constitutes a candidate model for the acoustic channel. Therefore, the quality of the received information should improve as we find more and more of these channel estimates, given we know how to combine these appropriately. We can improve the system performance at the expense of processing power while keeping the source power, bandwidth and number of source and receivers the same.

At the frequency of operation of the acoustic uplink, the DFE process must compensate for closely packed echoes subject to significantly different Doppler shifts in the presence of fairly stationary noise. The uplink receiver of Hermes employs a phase-lock-looped DFE routine that leverages this complementary solution approach. The same equalizer routine is started at a different time interval of the received sequence, with a varying number of feed-forward taps and, optionally, a varying value for the forgetting factor λ. The governing equations of the DFE process become:

$$\mathbf{Z_{eq,n,m}} = \left[z_{fr,n-m}, \ldots, z_{fr,n+1-N_{eq,f}-m}, d_{fr,n-1}, \ldots, d_{fr,n-N_{eq,b}} \right]^T , \tag{5}$$

$$r_{eq,n,m} = \mathbf{C_{eq,n,m}^H} . \mathbf{Z_{eq,n,m}} , \tag{6}$$

$$\varepsilon_{eq,m}^2 = \sum_{k=0}^{n} \lambda^{n-k} \left| r_{eq,k,m} - d_{fr,k,m} \right|^2 , \tag{7}$$

$$\mathbf{C_{eq,n,m}} = \left(\sum_{k=0}^{n} \lambda^{n-k} \mathbf{Z_{eq,n,m}} . \mathbf{Z_{eq,n,m}^H} \right)^{-1} . \left(\sum_{k=0}^{n} \lambda^{n-k} \mathbf{Z_{eq,n,m}} . \mathbf{U_{fr}^H} \right). \tag{8}$$

The index *m* indicates a different configuration of the starting time interval and number of feed-forward taps. The minimum number of feed-forward coefficients is set to cover most of or the entire multipath. The number of feedback coefficients is kept as low as possible for stability purposes: a single feedback tap has proved sufficient between 262.5 kHz and 337.5 kHz.

The equalizers producing the lowest mean-squared error estimation of the training sequence are retained, and the corresponding starting time, number of feed-forward coefficients and forgetting factor are stored. The entire message is equalized using each combination of starting time, number of coefficients and forgetting factor (Figure 6 and Figure 7). For each candidate (also called path) *m*, the *k*-th equalized symbol $r_{eq,k,m}$ is calculated and a decision $d_{eq,k,m}$ is made. Each set of estimates ($r_{eq,k,m}$, $d_{eq,k,m}$) is the input to a soft-decision BCH or Turbo decoder. In the unlikely case where error coding is not used, the symbol estimates ($r_{eq,k,m}$, $d_{eq,k,m}$) are combined using maximal ratio combining.

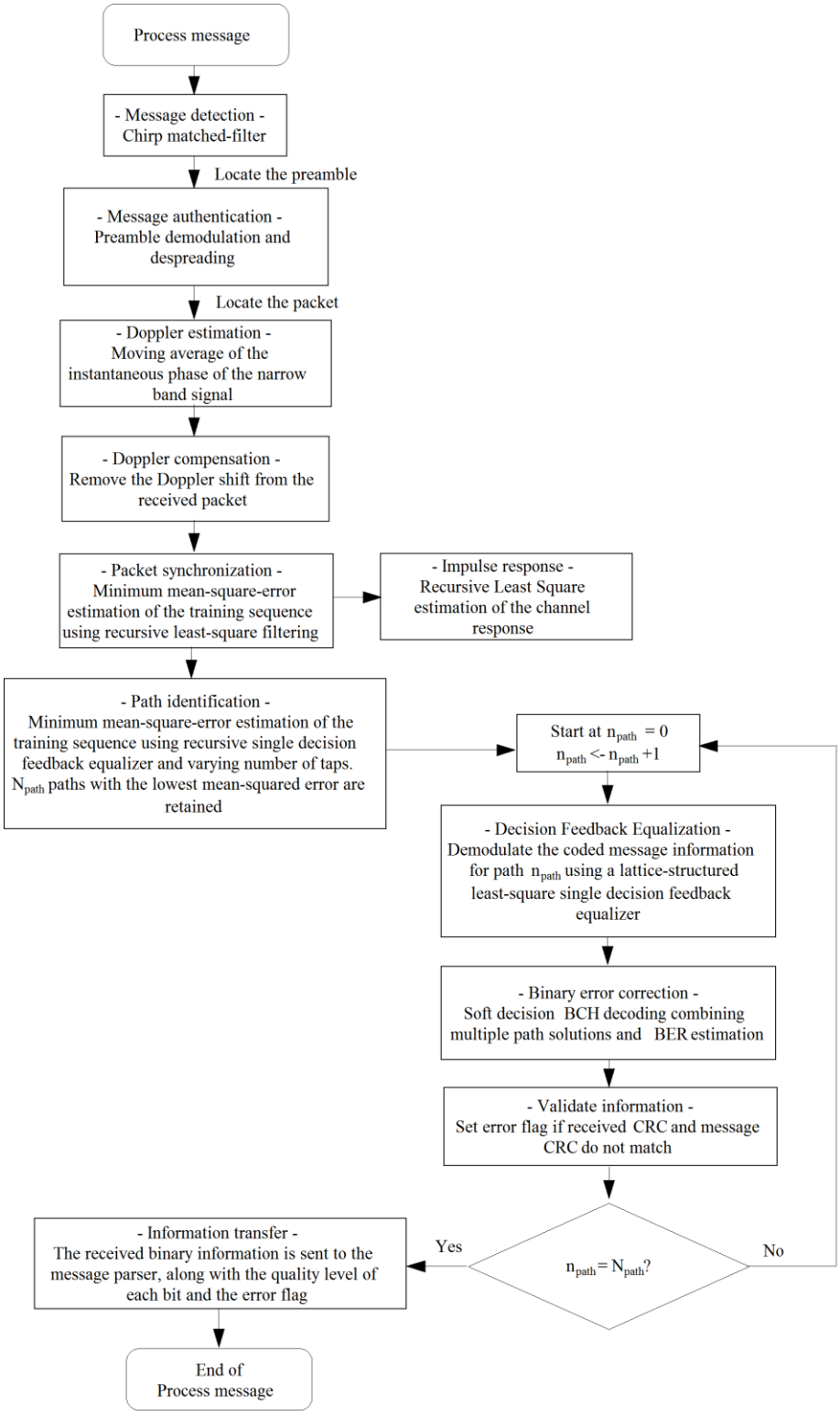

Figure 5: Signal processing flowchart of the HERMES high-rate uplink receiver (single unit).

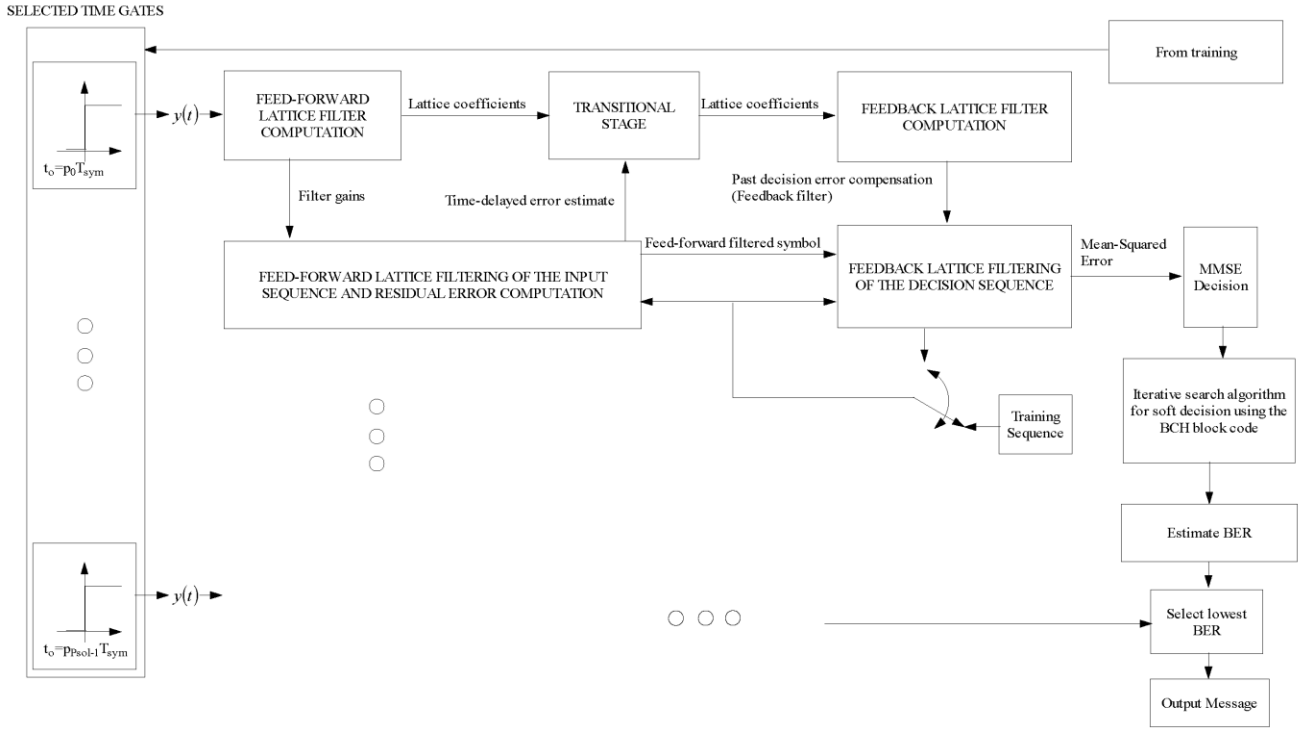

Figure 6: Decision feedback equalization of the data packet.

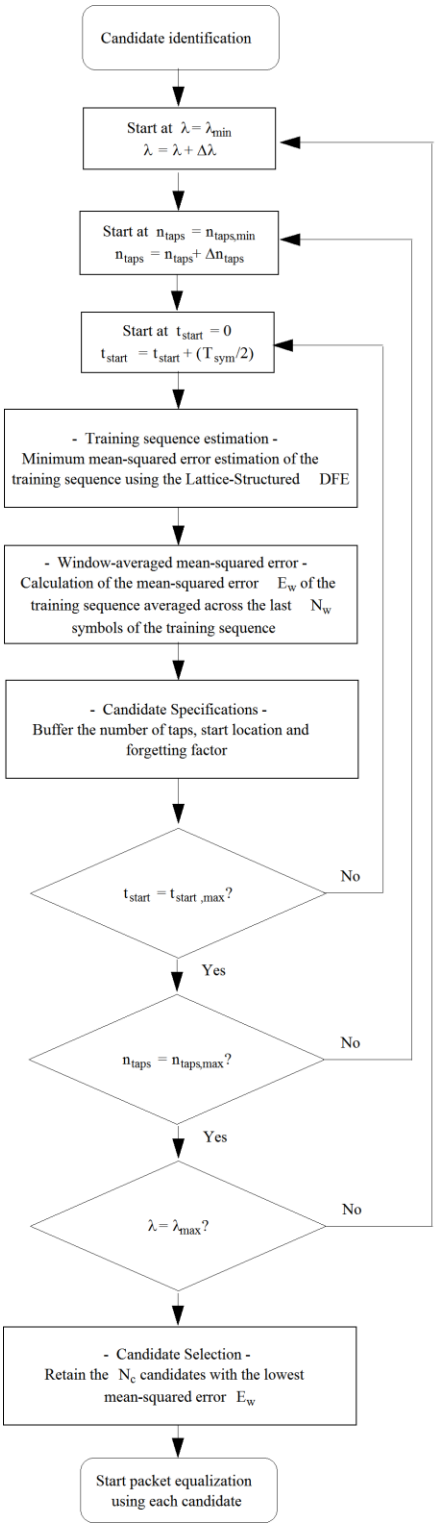

Figure 7: DFE candidate selection process.

2.3 Low Bit Rate Downlink

2.3.1 Source

The low bit rate command downlink operates in the frequency band from 62 kHz to 89 kHz, and achieves true data rates of up to 4,223 bps. It tolerates Doppler-based motion up to 2 m/s and is designed to exceed the range of operation of the high bit-rate acoustic uplink. The downlink moves low bit rate multiplexed data from the topside component to the wetside modem. The data originates from a topside user interface or other topside sources as command-and-control messages and configuration data for the AUV platform and its subsystems, including cameras, sonar and sensors, as well as the modem's own configuration data.

The acoustic downlink incorporates three possible different modes of operation using a Frequency Hopping (FH) scheme with 4 or 2 hops and 16 or 8 sub-bands per hop. Each sub-band accommodates a QPSK-modulated symbol. Mode 0 uses two hops and 16 sub-bands per hop. Modes 1 and 2 use four hops. Mode 1 uses 16 sub-bands per hop, while mode 2 uses 8 sub-bands per hop. Each sub-band for modes 1 and 2 has a bandwidth of 429 Hz, composed of the information bandwidth of 247 Hz and a fixed guard band of 182 Hz to minimize inter-carrier interference. The results presented in this report cover mode 1 only.

The input data sequence is formatted into frames such that one frame contains 86 bytes (688 bits) of information and a 2-byte CRC-16. These 88 bytes are encoded using a BCH(15,11,1) encoder. Two out-of-band detection symbols and a short synchronization impulse and reference sequence are transmitted prior to encoded data signals, as shown in Figure 8. Each detection symbol has a bandwidth of 429 Hz, while the synchronization impulse covers the highest (4^{th}) hop band (16 sub-bands for mode 1, 8 sub-bands for mode 2).

A reference sequence is obtained by generating symbols with zero reference phase through an entire hopping cycle. The reference symbols are generated periodically. The period depends on the Doppler-shift tolerance. The most Doppler-tolerant scheme uses a reference sequence before each data sequence, effectively halving the data rate. Although this approach is sub-optimal in terms of energy efficiency, this approach is very robust to compensate for Doppler shifts at very little computational expense. Computational efficiency is a strict requirement in the Hermes unit, as the wetside receiver unit must handle a suite of other tasks, such as encoding and modulation of uplink sequences, data compression, Ethernet and retransmission protocol. This approach does not preclude the addition of more energy efficient methods, once the robustness at these high-frequencies is demonstrated.

The spectrogram of the output signal is shown in Figure 9. The sampling rate is 220000 Hz, and each symbol (created in one hop) contains 2048 samples in modes 1 and 2, while each symbol is 4096 sample long in mode 0. Also, each symbol overlaps by 50% with the previous and by 50% with the following one. **Error! Reference source not found.** provides a summary of each mode of operation, assuming a single reference sequence following the synchronization pulse. **Error! Reference source not found.** and **Error! Reference source not found.** provide the message specifications using a single reference sequence or one reference per symbol, respectively.

Table 2: Summary of the modes of operation for the acoustic downlink.

Mode	#hops	# bands per hop	#symbols per hop	Sub-band	Symbol duration
0	2	16	32	214.9Hz	18.62ms
1	4	16	32	429Hz	9.31ms
2	4	8	16	429Hz	9.31ms

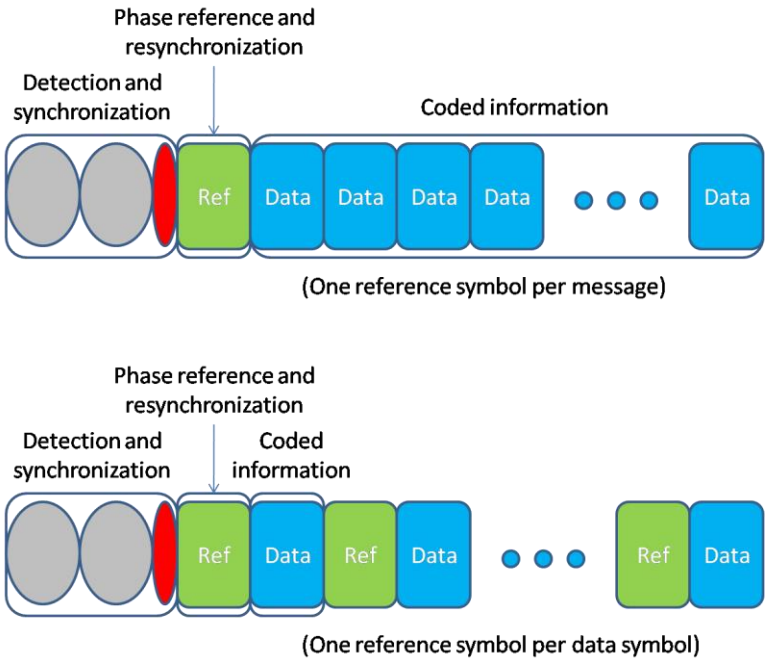

Figure 8: Message format for the acoustic downlink.

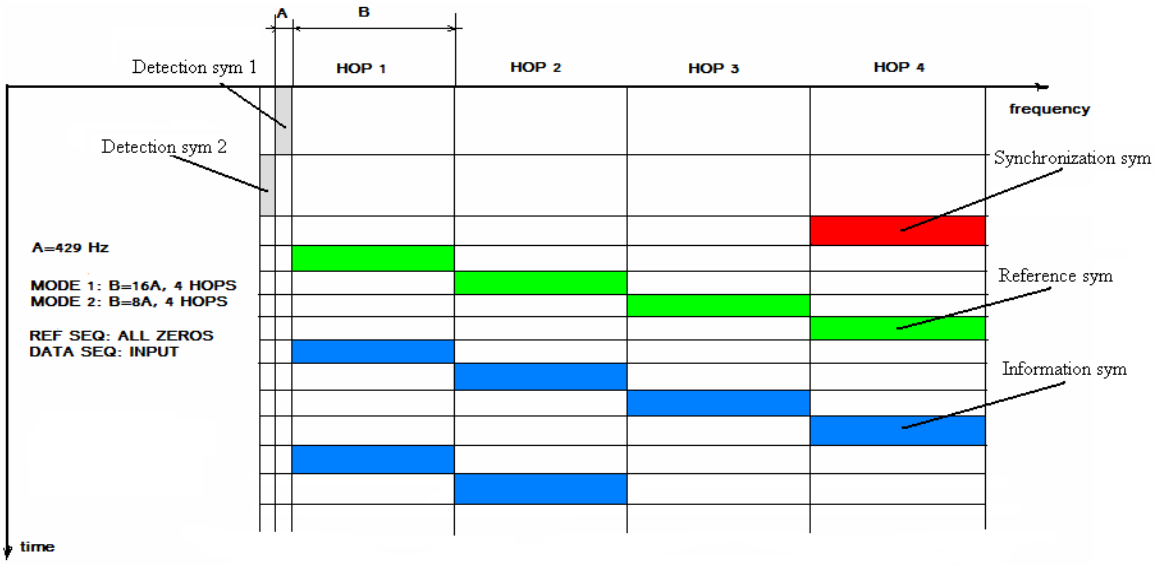

Figure 9: Spectrogram of a downlink message.

Table 3: Message specifications for the acoustic downlink, assuming a single reference sequence following the synchronization pulse.

Mode	0	1	2
Reference symbols	4	4	4
Symbols/frame	30	30	60
Frame duration (s)	0.3456 s (0.3258s *)	0.1821 s (0.1629 s *)	0.3223 s (0.3025 s *)
Raw bit rate (bits/s)	2778 (2946 *)	5272 (5893 *)	2978 (3173 *)
Coded bit rate (bits/s)	1990 (2111 *)	3778 (4223 *)	2134 (2274 *)

(*) Excluding the detection symbols and synchronization pulse.

Table 4: Message specifications for the acoustic downlink, assuming one reference sequence per data symbol.

Mode	0	1	2
Reference symbols	30	30	60
Data symbols/frame	30	30	60
Frame duration (s)	0.6062 s (0.5678 s*)	0.3031 s (0.2839 s*)	0.5829 s (0.5632 s*)
Raw bit rate (bits/s)	1583 (1690 *)	3167 (3381 *)	1647 (1704 *)
Coded bit rate (bits/s)	1135 (1212 *)	2270 (2423 *)	1180 (1221 *)

(*) Excluding the detection symbols and synchronization pulse.

In formal notation, the transmitted signal $s_T(t)$ is composed of the detection symbols $s_{d1}(t)$ and $s_{d2}(t)$, synchronization pulse $s_{syn}(t)$, reference symbols $s_{ref}(t)$ and the information frame signal $s_f(t)$. d_n $(n=1,...,D)$ is the coded bit sequence of length D. N_{SB} is the number of sub-bands per hop. Assuming 2 bits per sub-band (QPSK modulation), the number of symbols per frame N_{SF} is

$$N_{SF} = ceil\left(D/2N_{SB}\right). \tag{9}$$

If the input sequence does not contain enough bits to generate an integer number of symbols, the input sequence is zero-padded with K_z zero bits. The new sequence is denoted $\tilde{d}_n$ and the number of appended zeros is

$$K_z = 2N_{SB}N_{SF} - D. \tag{10}$$

The i^{th} data symbol falls into the hop $h(i)$,

$$h(i) = i\left[N_H\right]. \tag{11}$$

$\left[N_H\right]$ denotes "modulo N_H". A di-bit at hop $h(i)$ and m^{th} sub-band corresponds to the carrier frequency $f_{h(i),m}$ given by

$$f_{h(i),m} = f_{c,start} + [(h(i)-1)N_{SB} + (m-1)]\Delta f, \tag{12}$$

where $f_{c,start}$ is the lowest carrier frequency and Δf is a sub-carrier spacing. The i^{th} symbol is

$$s^{(i)}(t) = \sum_{m=0}^{N_{SB}-1} b(t) * \cos\left(2\pi f_{h(i),m} t + \theta_{i,m}\right), 0 \le t \le T_s. \tag{13}$$

'*' denotes the convolution operator. T_s is the data symbol duration. The phase $\theta_{i,m}$ is a function of the Gray-coded input binary sequence

$$\theta_{i,m} = \frac{\pi}{4}[1 + 4\tilde{d}_{l+1} - 2\tilde{d}_{l+1}\left(1-\tilde{d}_{l+2}\right) - 2\tilde{d}_{l+2}\left(1-\tilde{d}_{l+1}\right)]. \tag{14}$$

The index l represents the number of bits that have been processed, so that the next di-bit is formed from the $(l+1)$-th and $(l+2)$-th bits,

$$l = 2(i-1)N_{SB} + 2(m-1). \tag{15}$$

The pulse shaping function $b(t)$ is given by

$$b(t) = \frac{\operatorname{sinc}\left(\frac{\pi t}{T_s}\right)\cos\left(\frac{9\pi t}{10T_s}\right)}{1-4\left(\frac{9t}{10T_s}\right)^2}. \tag{16}$$

Finally, the information frame signal is

$$s_f(t) \approx \sum_{i=1}^{N_{SF}} \frac{10^{SL/20}}{N_{SB}} s^{(i)}\left(t - \frac{i-1}{2}T_s\right), \tag{17}$$

where SL denotes the transducer's source level. Each sequence of reference symbols is created following similar steps. The time dependence of the j^{th} reference symbol is

$$s_{ref}^{(j)}(t) = \sum_{m=0}^{N_{SB}-1} b(t) * \cos\left(2\pi f_{j,m} t\right), 0 \le t \le T_s,\ j = 1,\ldots,N_H. \tag{18}$$

The reference phase for each sub-band is zero radians. Finally, each sequence of the reference symbols is

$$s_{ref}(t)=\sum_{j=1}^{N_H}\frac{10^{SL/20}}{N_{SB}}s_{ref}^{(j)}\left(t-\frac{j-1}{2}T_s\right). \tag{19}$$

The synchronization impulse covers the last hop frequency band. Its bandwidth and frequency spectrum are

$$W=N_{SB}\Delta f, \tag{20}$$

$$S_{sync}(f)=B(f)\,rect\left(\frac{f-f_0}{W}\right). \tag{21}$$

$rect\left(\frac{f-f_0}{W}\right)$ is a rectangular pulse of width W centered at $f_0=\left(N_H-\frac{1}{2}\right)N_{SB}\Delta f$. $B(f)$ denotes the Fourier transform of the pulse shaping function $b(t)$. The time dependence of the synchronization pulse is

$$\begin{aligned}&s_{syn}(t)=10^{SL/20}b(t)*\left(W\frac{\sin(\pi Wt)}{\pi Wt}e^{j2\pi f_0 t}\right)\\&0\le t\le T_{syn}.\end{aligned} \tag{22}$$

The frequency spectrum and the time dependence of the N_D detection symbols are given by similar relationships. All detection symbols have a bandwidth Δf and are placed at $f_c^{(l)}=f_{start}-(2l-1)\frac{\Delta f}{2}$. The time domain dependence of the l-th detection symbol is

$$s_d^{(l)}(t)=10^{SL/20}b(t)*\left(\Delta f\frac{\sin(\pi\Delta f t)}{\pi\Delta f t}e^{j2\pi f_c^{(l)}t}\right),0\le t\le T_d. \tag{23}$$

Assuming that a single reference sequence is used for the entire message, the output signal formed from the input data sequence is

$$\begin{aligned}&s_T(t)=\sum_{l=1}^{N_D}s_d^{(l)}(t-(l-1)T_d)+s_{sync}(t-N_DT_d)+\\&+s_{ref}(t-N_DT_d-T_{syn})+s_f(t-N_DT_d-T_{sync}-T_{ref}),\end{aligned} \tag{24}$$

where T_d, T_{ref}, T_{syn} denote respectively the time durations of the detection symbol, reference sequence and the synchronization pulse.

2.3.2 Receiver

The downlink demodulation process starts with the search for N_D out-of-band detection symbols and the synchronization pulse. If all of them have been detected in the corresponding frequency bands, the detection process is complete. The downlink receiver acquires signal whose duration

is equal to the detection symbol duration (i.e. acquires the same number of samples) and looks for a spectral component that carries maximal energy. The search is performed over the entire downlink frequency band, excluding the sub-bands allocated for the other detection symbols. The k-th detection symbol ($k=1,2,...,N_D$) is detected if (a) the previous $(k-1)$ detection symbols have been detected and (b) the next acquired symbol $r(t)$ has a peak of energy located within the band centered on $f_c^{(k)}$,

$$f_c^{(k)} = f \,|\, \max_{f \in F_k} \left\{ \left| R(f) \right|^2 \right\}. \tag{25}$$

$R(f)$ is the Fourier transform of the received signal $r(t)$. The search for the spectral component carrying maximum energy is performed through the band F_k

$$F_k = \left[f_{start} - N_D \Delta f, f_{stop} \right] | \bigcup_{l \neq k} \left[f_c^{(l)} - \frac{\Delta f}{2}, f_c^{(l)} + \frac{\Delta f}{2} \right] \tag{26}$$
$$l = 1,2,...,N_D,$$

where $f_{start}, f_{stop}, \Delta f, f_c^{(l)}$ represent respectively the start and stop downlink frequencies, detection symbol bandwidth and detection symbol central frequency. The block diagram of the downlink message detection algorithm is shown in Figure 10.

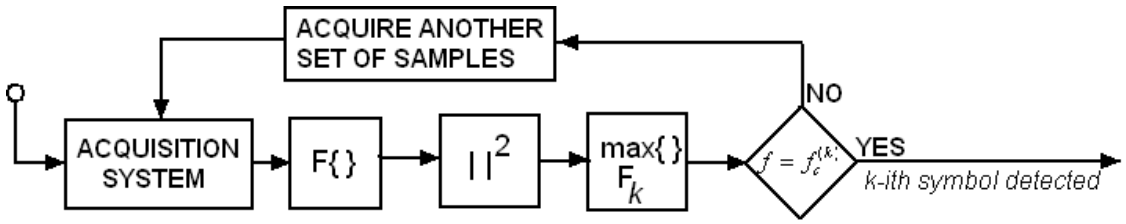

Figure 10: Message detection flowchart for the acoustic downlink.

The exact time instant at which the received synchronization pulse $r_{sync}(t)$ starts is obtained by examining the cross-correlation function between the transmitted symbol $s_{sync}(t)$ (known at the receiver side) and the complex conjugate of the received synchronization symbol $r_{sync}^*(t)$. Every operation takes place in base-band, so that complex algebra is used,

$$R_{s_{sync} r_{sync}^*}(\tau_l) = \int_0^{T_{sync}} s_{sync}(t) r_{sync}^*(t+\tau_l)\, dt, \tag{27}$$

The synchronization pulse starts at peak location τ_{sync} of the cross-correlation function $R_{s_{sync} r_{sync}}(\tau_l)$,

$$\tau_{sync} = \tau_l \,|\, \max_{\tau_l} \left\{ R_{s_{sync} r^*_{sync}} (\tau_l) \right\}. \tag{28}$$

Hence, the sequence of the received reference symbols starts at time instant τ_{ref},

$$\tau_{ref} = \tau_{sync} + T_{sync}, \tag{29}$$

where T_{sync} is the duration of the synchronization pulse. The estimation of the starting time instant of the synchronization pulse is schematically shown in Figure 11.

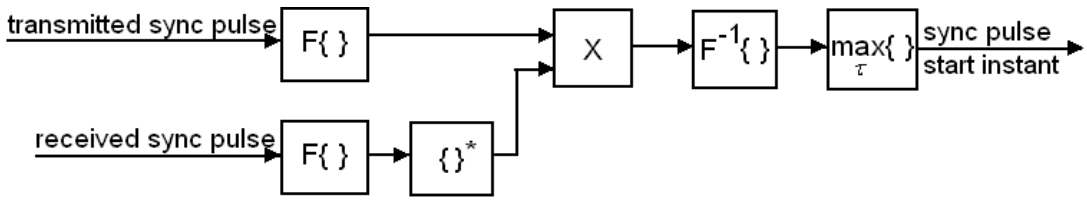

Figure 11: Message synchronization using the downlink synchronization pulse.

Once the starting instant of the reference symbols is determined, the receiver acquires reference and information symbols. The information symbols are demodulated based on the received reference symbols. To simplify the notations, we assume that a single reference sequence is transmitted for the entire message.

The spectrum of the i-th received information symbol $r_f^{(i)}(t)$ covers one of the allocated hops of index $h(i)$. The received reference symbol transmitted in hop $h(i) = 1, 2, ..., N_H$ is $r_{ref}^{(h(i))}(t)$. Each sub-band $m = 1, 2, ..., N_{SB}$ of the received information symbol $r_f^{(i)}(t)$ carries two bits of information (one QPSK symbol). They are recovered based on the phase difference between the constellation points demodulated from the sub-band m of the information symbol $r_f^{(i)}(t)$ and the reference symbol $r_{ref}^{(h(i))}(t)$.

The phase of the received QPSK symbol from the m-th sub-band of the i-th information symbol is denoted $\phi_{i,m}^{(f)}$. It is computed as a phase argument of the Fourier spectrum $R_f^{(i)}(f)$ of the i-th received information symbol at a central frequency $f_{h(i),m}$ of the m-th sub-band of the hop $h(i)$. Similarly, the phase of the received reference symbol $\phi_{h(i),m}^{(ref)}$ in the m-th sub-band of hop $h(i)$, is the phase argument of the Fourier spectrum $R_{ref}^{(h(i))}(f)$ associated with hop $h(i)$ at the carrier frequency $f_{h(i),m}$ in the m-th sub-band,

$$\phi_{i,m}^{(f)} = \arg_{f = f_{h(i),m}} \left\{ R_f^{(i)}(f) \right\}, \tag{30}$$

$$\phi_{h(i),m}^{(ref)} = \arg_{f=f_{h(i),m}} \left\{ R_{ref}^{(h(i))}(f) \right\}. \tag{31}$$

The information bits are mapped based on the estimated phase difference $\Delta\phi_{i,m}$,

$$\Delta\phi_{i,m} = \phi_{i,m}^{(f)} - \phi_{h(i),m}^{(ref)}. \tag{32}$$

The constellation diagrams of the transmitted and received symbols are shown in Figure 12.

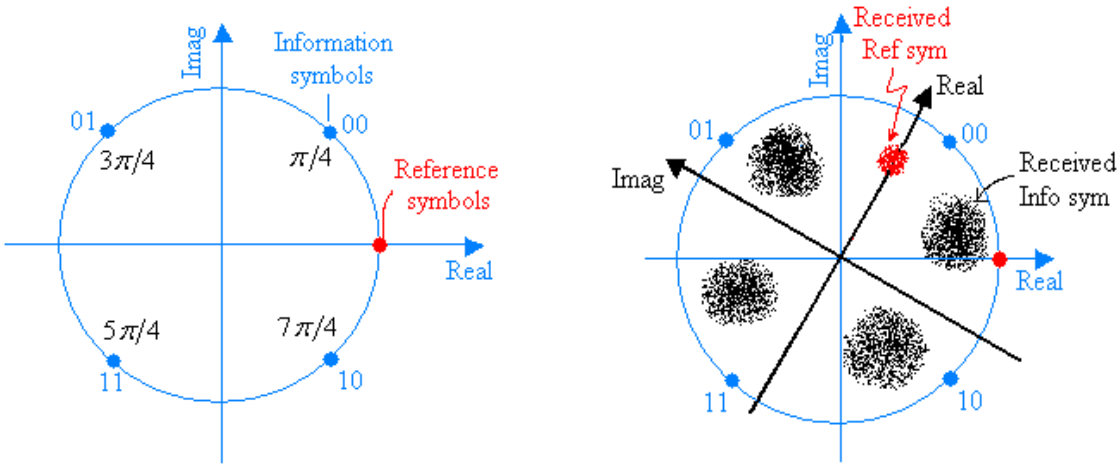

Figure 12: Constellation diagrams for the transmitted and received downlink messages.

3. Doppler tracking

The Hermes acoustic uplink receiver currently uses a robust moving average (MA) estimate for Doppler compensation. However, an in-depth study showed that the auto-regressive moving average (ARMA) approach (designed from 2nd order Volterra kernels) to Doppler estimation, shown in this section, often provides better estimates.

3.1 Moving Average Approach

At the receiver end, the Doppler shift is estimated by measuring the average rate of change in the signal argument of the 375 kHz tone received with every Hermes message $r(t) = e^{j\phi(t)}$ (converted to baseband). In the discrete domain, if *m* is the time index of a block of sample size $M = F_d T_{win}$ (F_d is the baseband sampling frequency, T_{win} is the width of a sliding time window),

$$\phi_m = \frac{1}{M} \sum_{n=0}^{M-1} \arg\left\{ r_b\left(\left(n + (m-1)M \right) T_d \right) \right\}. \tag{33}$$

From this information, estimation of the Doppler shift Δf_m and the Doppler velocity U_{mvg} are,

$$\Delta f_m = \left(\frac{F_d \Delta \phi_m}{2\pi M} \right), \tag{34}$$

$$U_{mvg}(m) = \left(\frac{c \Delta f_m}{f_{cw}} \right), \tag{35}$$

where *c* is the speed of sound in water.

3.2 Auto-regressive approach

An auto-regressive algorithm was developed which gives a continuous time estimate of the estimate $u(t)$ of the source velocity of $v(t)$ using the same tone $r(t) = e^{j\phi(t)}$ received with every Hermes message and converted to baseband. Here, $\phi(t) = \frac{2\pi}{\lambda}(ct - u(t)t)$. If we define $a(t) = \frac{\lambda}{2\pi}\dot{\phi}(t)$, it can be shown that,

$$u(t) = c - \frac{1}{t}\int_0^t a(\xi)\, d\xi, t > 0. \tag{36}$$

In the discrete time domain, $u(nT_s) \equiv u_n = c - \gamma_n, n \in \mathbb{N}^*$, so that

$$\gamma_n \equiv \gamma(nT_s) = \frac{1}{(nT_s)}\int_0^{nT_s} a(\xi)\, d\xi \approx \frac{1}{n}\sum_{k=0}^{n} a_k, \forall n > 0, a_k \equiv a(kT_s), k \in \mathbb{N}. \tag{37}$$

If trapezoidal integration is used, we can rewrite this equation in recursive form,

$$\gamma_n = \left(\frac{n-1}{n} \right)\gamma_{n-1} + \frac{1}{2n} a_n + \frac{1}{2n} a_{n-1}, n \in \mathbb{N}^*. \tag{38}$$

This formulation corresponds to a time-varying, autoregressive, moving-average (ARMA) filter.

The initial condition is $\gamma_0 = c - u(0)$. The discrete Doppler velocity obtain from this equation is,

$$U_{IIR}(n) = c - \gamma_n, n \in \mathbb{N}. \tag{39}$$

4. Single input multiple output uplink

The SIMO acoustic communication system proposed in this research uses multiple receivers and adaptive spatial diversity combining to improve the reliability of the underwater acoustic channel.

In each receiver, the received symbols are equalized using the MSDFE algorithm and results are used to perform diversity combining at two levels. The block diagrams of proposed diversity approach are shown in Figure 13 and Figure 14, and the nomenclature used in the block diagrams is given in Table 5.

The SIMO operation comes in two configurations. In the first configuration (noted level-1 and shown in Figure 13), the symbols collected at each receiver are equalized using a DFE and combined using MRC. More specifically, the symbols used (noted $d_l(m)$) are obtained at the output of the equalizer prior to the decision process. This combined message $c_l(m)$ is used to form a sequence $p_i(m)$ which is a feedback parameter to diversity combining performed at higher level.

In the second configuration (noted level-2 and shown in Figure 4), the MRC outputs are used as decision symbols in the DFE. This second configuration is a form of turbo equalization: the process can be repeated over and over, leading to a better estimate of the received message as the number of iterations increases.

Table 5: Nomenclature used in the block diagrams for multilevel diversity.

Name	Description
r	Signal at the receiver
l	Receiver index
L	Number of receivers
k	Candidate index in MSDFE
K	Number of DFE candidates
n	Decoded bit index
m	Coded bit index (after de-convolution)
i	Iteration index
O_l	Optimal set of DFE parameters
$b_l(n)$	Number of bits n of receiver l after MSDFE process
$q_l(n)$	Quality index of $b_l(n)$ (BER and SNIR of the binary sequence)
$c_i(m)$	Coded bit m of iteration i
$d_l(m)$	De-convolved complex symbol m of branch l for the best DFE candidate
$p_i(m)$	Quality reference parameter for level-2 diversity combining
$g_l(m)$	Received sequence using optimal DFE parameters
DFE	Decision Feedback Equalizer
ECC	Error Cyclic Check
MSE	Mean Squared Error

The received sequence at the receiver is $r_l(t)$. The equalizers in each DFE set of every receiver start the equalization process at different time interval of the received sequence using variable DFE parameters, generating estimates of the received sequence with the lowest mean squared error. Further, an error cyclic check (ECC) using 32 redundancy bits (CRC-32) is performed on the output of each DFE. The minimum MSE decision process implemented at the output of ECC gives the binary sequence $b_l(n)$ and its SNIR represented as a quality index $q_l(n)$. The optimal parameters O_l of the DFE that generate the best estimate and symbols $d_l(m)$ prior to the MSE decision are retained in each receiver. The results at the output of any one of the receivers are identical with results in the case SISO system.

The next step in the adaptive diversity process is to use the parameters obtained during the MSDFE process. Symbols $d_l(m)$ are used to perform level-1diversity combining. They are combined using MRC in a sense that the decision on each symbol is made based on the maximum

SNIR value of the symbol. The combined message $c_i(m)$ is used to form a quality reference sequence $p_i(m)$ which is a feedback parameter to diversity combining performed at higher level. In addition, the combined message $c_i(m)$ is used to evaluate the binary sequence estimate and its quality index (noted $b_{MRC}^{1}(n)$ and $q_{MRC}^{1}(n)$ in Figure 14) after first iteration of level-1 diversity.

The optimal DFE parameters O_l in each receiver and quality reference sequence $p_i(m)$ are used in level-2 diversity combining. This diversity combining is performed at DFE level. The estimates of the received sequence $g_l(m)$ obtained using the set of optimal parameters are evaluated using the reference sequence $p_i(m)$ symbols in the decision process. The outputs of level-2 diversity combining are corrected symbols $d_{l,i}^{2}(m)$. The symbols obtained at level-2 diversity are used for next iteration of level-1 diversity. Additionally, the binary sequence estimate and the quality index of the new improved sequences (noted $b_i^2(n)$ and $q_i^2(n)$ in Figure 14) are calculated. The diversity combining performed at DFE level is a form of turbo equalization repeated until the best possible result is achieved or a predefined error criterion is met. BER and SNIR are estimated using binary sequence and quality index at each level and iteration and used to evaluate the improvement of the acoustic channel performance.

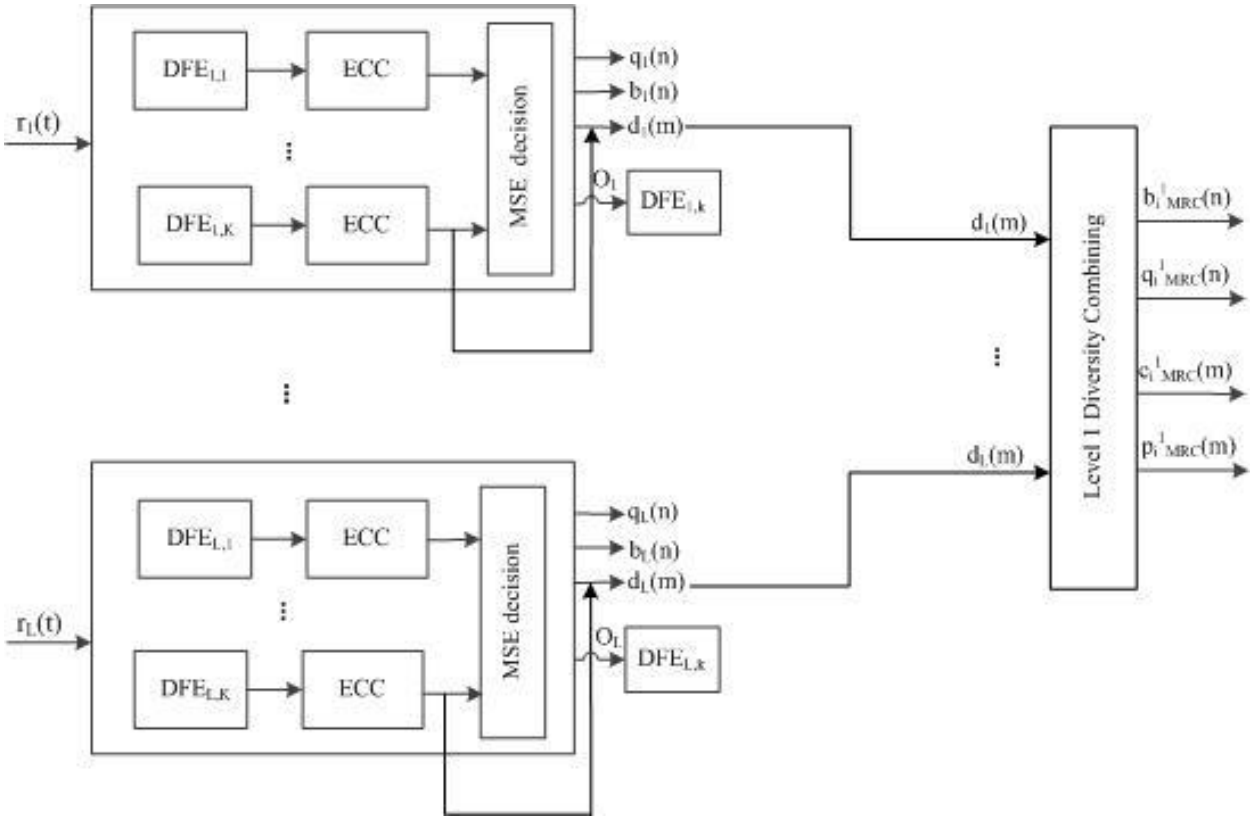

Figure 13: SIMO level-1 configuration.

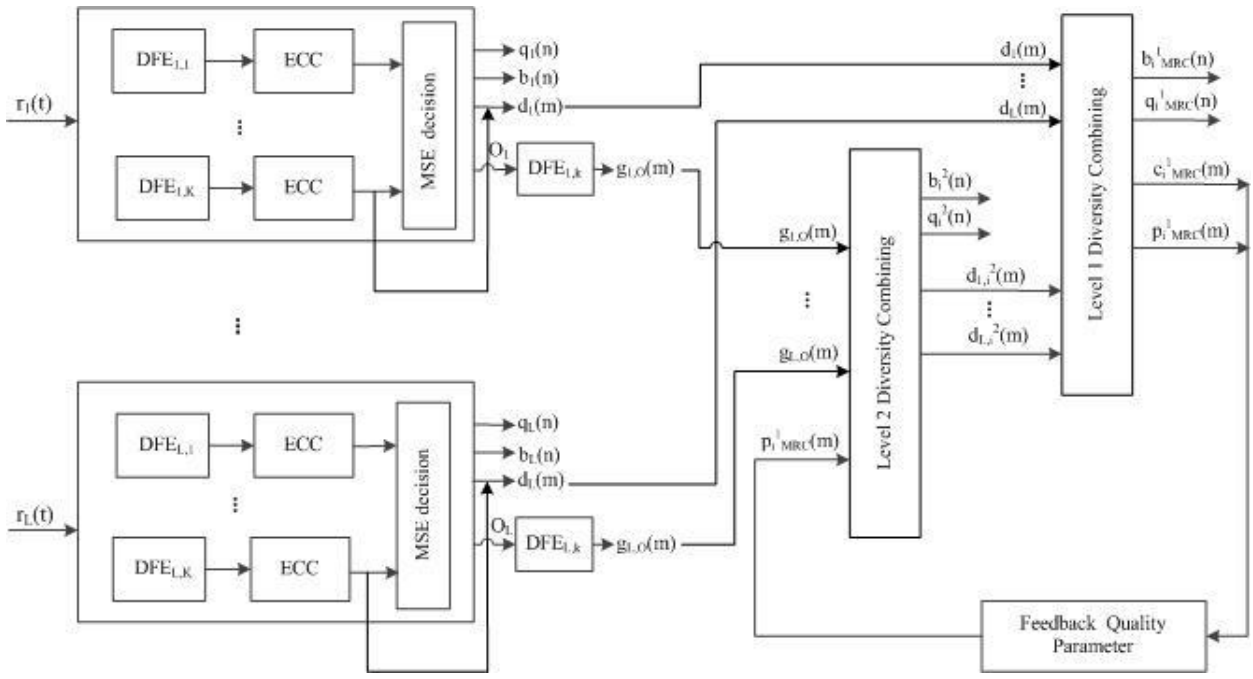

Figure 14: SIMO level-2 configuration.

5. Multiple input multiple output uplink

The applicability of Multiple-Input-Multiple-Output (MIMO) technology to Hermes was evaluated, so that multiple sources and receivers distributed over an area can be used simultaneously. The contributions brought by this work to the field of underwater acoustic communications lie in the development of a channel model and estimation algorithm and the development of a MIMO deconvolution system. MIMO underwater acoustic communication is achieved by modifying the signaling of the FAU Hermes uplink message. The limited bandwidth, reliability and flexibility presented by underwater acoustic communication systems can be partly resolved by the use of MIMO techniques. Indeed, the capability to send different messages via each source represents a considerable enhancement of the overall data rate of the system. Furthermore, being able to increase the coverage area of the communication by setting up a spatially-distributed network constitutes an important benefit. However, MIMO communication systems cannot guarantee perfect communications, as signal fading, Doppler spread and ambient noise impair the overall performance of any underwater acoustic modem. The proper retrieval of MIMO messages requires both an accurate estimation of the acoustic channels and a least-square (LS) channel estimation algorithm. Channel deconvolution (MIMO equalization) is critical to properly separate the messages coming from multiple sources and intersymbol interference. The deconvolution is implemented as a Minimum Mean Square Error (MMSE) equalizer. The theoretical limit of the deconvolution process is computed with an Interference Cancellation Linear Equalizer (ICLE), which removes the interference due to the use of MIMO using a priori information on the transmitted sequence.

5.1 System Model

5.1.1 Source Signals

The messages sent through the acoustic channels are obtained by modifying the signaling of Hermes. Here, i represents the source index. The proposed message is composed of the source-dependent MIMO sequence $s_{i,h}(t)$ followed after a predefined time delay τ_{msg} with the traditional Hermes message $s_{i,msg}(t)$, such that:

$$s_i(t) = s_{i,h}(t) + s_{i,msg}(t - \tau_{msg}). \tag{40}$$

$s_{i,h}(t)$ consists of a perfectly known pseudo noise (PN) sequences of length $\tau_H = 218.5\ \text{ms}$, up-sampled from the symbol frequency F_{sym} to the sampling frequency and pulse-shaped using a raised-cosine filter. Figure 15 shows an example of source signal. Given a carrier frequency f_0 and a signal level *SL*, the transmitted signal is

$$s_{i,h}(t) = 10^{SL/20} \cdot \left(s_{i,PN}(t) * b_{RC}(t)\right) \cdot \cos\left(2\pi f_0 t\right) \mu Pa, \tag{41}$$

where

$$b_{RC}(t) = \frac{\sin\left(\pi t / T_{sym}\right) + \sin\left(\beta \pi t / T_{sym}\right)}{\left(\pi t / T_{sym}\right)\left(1 - 4\left(\beta t / T_{sym}\right)^2\right)}. \tag{42}$$

Here, β is the roll-off coefficient and T_{sym} is the symbol period.

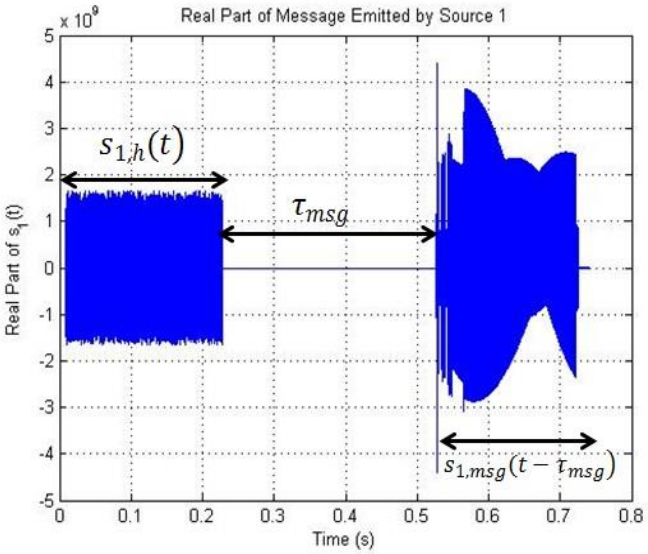

Figure 15: Real Part of Source Message 1.

The message following the MIMO sequence does not change with the source. The MIMO sequences (one per source) have a very low cross-correlation to their auto-correlation peak ratio. We observed that the peak ratio is approximately 40 (which is equivalent to 16 dB).

5.1.2 Channel Estimation

In this section, we present the operations carried out at the receiver end. We first focus on the channel estimation algorithm, followed with the equalization. The derivations are provided in the discrete time domain, where k stands for the time index and l the delay index. This process is performed over the duration of N_{win} time windows, of time index ι_{win} and length L_{win}. The received samples at receiver j can be written under matrix form

$$\tilde{\mathbf{r}}_j = \mathbf{S}_j \tilde{\mathbf{h}}_j + \tilde{\mathbf{n}}_j, \tag{43}$$

where $\mathbf{S}_j \in \mathbb{R}^{(L_{win}-L_j)\times T_j}$ represents the augmented source signal array at the $j-th$ receiver. $\mathbf{h}_j \in \mathbb{C}^{(T_j)\times 1}$ represents the augmented channel impulse response array. $\tilde{\mathbf{n}}_j \in \mathbb{C}^{(L_{win}-L_j+1)\times 1}$ represents the noise array.

As depicted in Figure 16, $k_0(\iota_{win})$ denotes the beginning of the time window. L_{ij} is the length of the channel impulse response between transmitter *i* and receiver *j*, and $L_j = \max_{i\in[1;N_t]}\{L_{ij}\}$. Finally, T_j is the sum of the channel lengths over the total number of transmitters N_t, so that $T_j = \sum_{i=1}^{N_t} L_{ij}$.

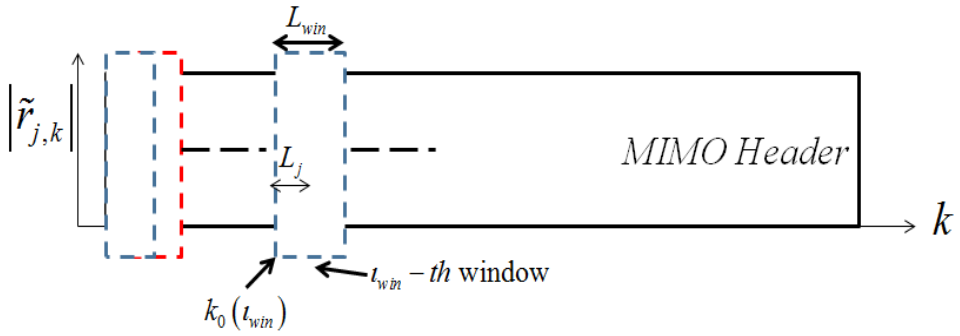

Figure 16: Definition of the parameters of the time-window used to perform the channel estimation at receiver j.

In the continuous time domain, and in the results section, the quantity T_j is noted T_L. The index j can here be dropped because the parameter T_L is a tunable parameter. Indeed, we will study the influence of this parameter on channel estimation and deconvolution process in the results section. The channel estimation is performed through minimization of the following quantity

$$\tilde{\mathbf{h}}_j^{est} = \arg\min_{\tilde{\mathbf{h}}_j} \left\| \tilde{\mathbf{r}}_j - \mathbf{S}_j \tilde{\mathbf{h}}_j \right\|^2 . \tag{44}$$

This leads to the LS estimation of $\tilde{\mathbf{h}}_j$ for every time window index t_{win},

$$\tilde{\mathbf{h}}_j^{est} = \left(\mathbf{S}_j^H \mathbf{S}_j \right)^{-1} \mathbf{S}_j^H \tilde{\mathbf{r}}_j, \tag{45}$$

where $(\,)^H$ represents the Hermitian operator. This operation requires a $T_j \times T_j$ matrix inversion.

5.1.3 EMD-Trended Estimation of the Time-Varying Channel

In exploring the possible conversion of Hermes into a MIMO device, single-carrier phase-modulated spread-spectrum sequences were used for channel estimation and deconvolution purposes. It clearly appeared that the channel estimation and deconvolution routines were quite sensitive to rapid time changes in the acoustic channel impulse response, which usually reflects the presence of Doppler spread produced for the most part by moving boundaries and oscillating sensors. A trend estimation technique, based on the empirical modal decomposition (EMD) method, was applied to the least-square estimate of the channel impulse response. Simulated data produced with a Rayleigh channel model and experimental data collected in a marina were used. The channel estimation method was estimated the time varying impulse response of the acoustic channel with a high-resolution of both time and delay (down to 7 μs) at the expense of high computational requirements.

The trend estimation constitutes a potential improvement to the least-square channel estimation aforementioned. At the core of this technique is the decomposition of the underwater acoustic channel estimate into a random component that characterizes the channel random behavior, and a second component that behaves essentially as in a deterministic medium. In our case, the decomposition of the channel impulse response estimate $h_{est}(k,l)$ can be expressed as a sum of zero-mean amplitude-modulated and frequency-modulated components plus a residue, using the EMD method. In discrete form, the estimated channel response is represented in the empirical model space as:

$$h^{est}(k,l) = \sum_{q=1}^{Q} m_q(k) + O(Q,k). \tag{46}$$

Here k is the same window time index described in the previous section, Q is the total number of modes in the EMD, m_q is the q^{th} mode resulting from the EMD and $O(Q;k)$ is the residue obtained from the Q-modes empirical modal decomposition of $h_{est}(k;l)$. The discrimination between the trend part and the fluctuation component using the EMD algorithm depends on a threshold criterion S_{TH}. The trend is the component with the slower rate of fluctuation. The signal is decomposed by taking the fastest fluctuating components away successively until we reach a threshold S_{TH}. Those components have smaller periods, and thus higher frequencies, than the period of the pseudo-deterministic component with the smallest period, and are included in the fluctuating component of the signal. The remaining part, including the residual, constitutes the trend component of the signal. Using this threshold, the EMD decomposition becomes,

$$h^{est}(k,l) = \sum_{q=1}^{S_{TH}} m_q(k) + \sum_{q=S_{TH}+1}^{Q} m_q(k) + O(Q,k). \tag{47}$$

The first right-hand term represents the channel impulse response fluctuation and the sum of the second and third right-hand terms is the channel impulse response trend. Different techniques have been proposed to estimate this threshold value; however there is no deciding rule for how to choose it. It has been shown that STH remains typically a small number that depends partly on the signal length and that is at most $log_2(K)$, where K is the length of $h^{est}(k,l)$. For our application, considering the signal length and total duration, we choose a threshold criterion for the main paths to be $S_{TH} = 6$.

5.1.4 Minimum Mean Squared Error Linear Equalization

The MIMO deconvolution process presented in this report compensates for the co-antenna and inter-symbol interferences by using the time-varying MIMO channel estimates provided by the above mentioned algorithm. The critical parameters indentified in this performance study are: (1) the length of the channel estimate T_L; (2) the length T_κ of the pre-cursor and post-cursor of the linear equalization filter. We consider two equalization structures: conventional Linear Equalization (LE) and interference cancellation linear Equalization (ICLE) that provides theoretical lower bound of the equalization process. The process presented in this section consists of a feed-forward multi-channel linear filter optimized under MMSE criterion. Let L represent the maximum value of the sub-channel length L_{ij},

$$L = \max_{i\in[1;N_t],\, j\in[1;N_r]} \left\{ L_{ij} \right\}. \tag{48}$$

We define the matrices $\breve{\mathbf{r}}_k \in \mathbb{C}^{N_r}$ and $\breve{\mathbf{n}}_k \in \mathbb{C}^{N_r}$ as the received signal and noise over the total number of hydrophones:

$$\breve{\mathbf{r}}_k = \left[\tilde{r}_{1,k}, \cdots, \tilde{r}_{N_r,k} \right]^T, \tag{49}$$

and

$$\breve{\mathbf{n}}_k = \left[\tilde{n}_{1,k}, \cdots, \tilde{n}_{N_r,k} \right]^T. \tag{50}$$

Similarly, we define the transmitted signals $\mathbf{s}_k \in \mathbb{R}^{N_t}$ and channel impulse responses $\mathbf{H}_l \in \mathbb{C}^{N_r \times N_t}$ as:

$$\mathbf{s}_k = \left[s_{1,k}, \cdots, s_{N_t,k} \right]^T, \tag{51}$$

$$\mathbf{H}_l = \begin{bmatrix} \tilde{h}_{11,l} & \tilde{h}_{21,l} & \cdots & \tilde{h}_{N_t 1,l} \\ \vdots & & & \vdots \\ \tilde{h}_{1N_r,l} & \tilde{h}_{2N_r,l} & \cdots & \tilde{h}_{N_t N_r,l} \end{bmatrix}. \tag{52}$$

Therefore, the received signal becomes

$$\breve{\mathbf{r}}_k = \sum_{l=0}^{L-1} \mathbf{H}_l \mathbf{s}_{k-l} + \breve{\mathbf{n}}_k. \tag{53}$$

We now define κ_1 and κ_2 as the pre-cursor and post-cursors of the linear equalization filter. In this case, $\mathbf{x}_k \in \mathbb{R}^{(L+\kappa_1+\kappa_2)N_t}$, $\mathbf{y}_k \in \mathbb{C}^{(1+\kappa_1+\kappa_2)N_r}$ and $\mathbf{w}_k \in \mathbb{C}^{(1+\kappa_1+\kappa_2)N_r}$ are defined as

$$\mathbf{x}_k = \left[\mathbf{s}^T_{k-\kappa_2-L+1}, \cdots, \mathbf{s}^T_{k+\kappa_1}\right]^T, \tag{54}$$

$$\mathbf{y}_k = \left[\breve{\mathbf{r}}^T_{k-\kappa_2}, \quad \cdots, \quad \breve{\mathbf{r}}^T_{k+\kappa_1}\right]^T, \tag{55}$$

and

$$\mathbf{w}_k = \left[\breve{\mathbf{n}}^T_{k-\kappa_2}, \quad \cdots, \quad \breve{\mathbf{n}}^T_{k+\kappa_1}\right]^T. \tag{56}$$

In the results section, the influence of the pre-cursor and post-cursor is studied in the continuous time domain. In this report, the length of these cursors is assumed to be the same and is represented by T_κ. Next, we define the augmented matrix containing the matrices of channel impulse responses, denoted $\mathbf{H} \in \mathbb{C}^{\left((1+\kappa_1+\kappa_2)N_r\right)\times\left((L+\kappa_1+\kappa_2)N_t\right)}$,

$$\mathbf{H} = \begin{bmatrix} \mathbf{H}_{L-1} & \cdots & \mathbf{H}_0 & 0 \\ & \ddots & \ddots & \\ 0 & \mathbf{H}_{L-1} & \cdots & \mathbf{H}_0 \end{bmatrix}. \tag{57}$$

Therefore, this equation can be rewritten as

$$\mathbf{y}_k = \mathbf{H}\mathbf{x}_k + \mathbf{w}_k. \tag{58}$$

The output of LE process can be expressed as:

$$u^{est}_{i,k} = \mathbf{c}_i{}^T \mathbf{y}_k. \tag{59}$$

By using the MMSE criterion, the optimum equalization filter is,

$$\mathbf{c}_i = \left(\hat{\mathbf{H}}\hat{\mathbf{H}}^H + \frac{\sigma_n^2}{\sigma_s^2}\mathbf{I}\right)^{-1} \left\{\hat{\mathbf{H}}\right\}_i, \tag{60}$$

where $\mathbf{I}$ is the identity matrix of size $\left(1+\kappa_1+\kappa_2\right)N_t$, σ_n^2 is the variance of the noise and σ_s^2 is the variance of the original sequence $s_{i,k}$. $\left\{\hat{\mathbf{H}}\right\}_i$ denotes the $\left[\left(\kappa_2 - 1 + L\right)N_t + i\right] - th$ column of $\hat{\mathbf{H}}$, where $\hat{\mathbf{H}} \in \mathbb{C}^{(1+\kappa_1+\kappa_2)N_r \times (L+\kappa_1+\kappa_2)N_t}$ is the estimates of augmented channel matrix $\mathbf{H}$ for time window index ι_{win}.

Here, the estimated signal $s^{est}_{i,k}$ depends on length of the time window, which in turns depends on the measured channel response. If $N_{win} = 1$, the channel is stationary over a message duration and

$$s_{i,k}^{est} = u_{i,k}^{est}. \tag{61}$$

However, if $N_{win} \geq 1$, $u_{i,k}^{est}$ becomes a function of ι_{win}. In this case, the equalized signal for each sliding window is cropped and forms a section of the equalized output $s_{i,k}^{est}$,

$$\begin{aligned} &s_{i,k'}^{est} = u_{i,k}^{est}, \text{ where } \frac{L_{win}}{4} \leq k \leq \frac{3L_{win}}{4} - 1, \\ &k' = k + (\iota_{win} - 1) L_{win} O_R \text{ and } 1 \leq \iota_{win} \leq N_{win} - 2. \end{aligned} \tag{62}$$

The variables ι_{win}, L_{win} and O_R represent the time window index, length and overlapping rate, respectively.

5.1.5 MMSE Interference Cancellation Linear Equalizer

The ICLE has been developed to evaluate the best possible performance of the deconvolution process by assuming that the source signal is perfectly known. The output of the ICLE may be expressed as follows,

$$u_{i,k}^{ICLE} = \mathbf{p}_{i,k}^H \mathbf{y}_k - \mathbf{q}_{i,k}^H \overline{\mathbf{v}}_{i,k}, \tag{63}$$

$\mathbf{p}_{i,k}$ and $\mathbf{q}_{i,k}$ respectively stand for the feed-forward and feed-back filters, and $\overline{\mathbf{v}}_{i,k}$ is defined as,

$$\overline{\mathbf{v}}_{i,k} = \left[s_{k-N_{ICLE}-L+2}^T, \cdots, s_{k-K_{ICLE}-1}^T, \mathbf{v}_{i,k-K_{ICLE}}^T, s_{k-K_{ICLE}+1}^T, \cdots, s_k^T \right]^T, \tag{64}$$

$$\mathbf{v}_{i,k}^T = \left[s_{1,k}, \cdots, s_{i-1,k}, 0, s_{i+1,k}, \cdots, s_{N_t,k} \right]^T. \tag{65}$$

K_{ICLE} is the discrete delay index induced by the equalizer, such that $0 \leq K_{ICLE} \leq N_{ICLE} + L - 2$, where N_{ICLE} represents the discrete ICLE length. Under MMSE optimization, the feed-forward and feed-back equalization vectors become equal to:

$$\begin{cases} \mathbf{p}_{i,k} = \lambda_k \overline{\mathbf{p}}_k \\ \mathbf{q}_{i,k} = \hat{\mathbf{H}}^H \mathbf{p}_k \end{cases}, \tag{66}$$

where

$$\lambda_k = \frac{1}{1 + \mathbf{e}_{i,N_{ICLE}+L-1-K_{ICLE}}^T \hat{\mathbf{H}}^H \overline{\mathbf{p}}_k}, \tag{67}$$

and

$$\overline{\mathbf{p}}_k = \frac{\sigma_s^2}{\sigma_n^2} \hat{\mathbf{H}} \mathbf{e}_{i,N_{ICLE}+L-1-K_{ICLE}}. \tag{68}$$

$\mathbf{e}_{i,k}$ is a null column vector, with the exception of element $N_t\left(k-1\right)+i$ equal to 1. σ_n^2 represents the noise variance. The ICLE estimate $s_{i,k}^{ICLE}$ depend on the number of time windows used to perform the channel estimation, thus the last three equations also apply to $s_{i,k}^{ICLE}$.

5.1.6 Performance Metrics

The channel estimation performance is measured using the RMSE comparing the received header and the ability of the system to rebuild this received header using the estimated channels. First, we compare the received header and the emitted sequence, convolved with the estimated channel. The result is averaged across the total number of messages and receivers. This RMSE is given by:

$$\mathrm{RMSE}_{CE} = 20\log_{10}\left(\sqrt{\frac{\sum_{j=1}^{N_r}\sum_{m=1}^{N_{msg}}\left\|\tilde{\mathbf{r}}_j - \mathbf{S}_j\tilde{\mathbf{h}}_j^{est}\right\|^2}{N_r L N_{msg}} \Big/ \frac{\sum_{j=1}^{N_r}\sum_{m=1}^{N_{msg}}\left|\tilde{r}_j\left(t_m\right)\right|^2}{N_r N_{msg}}}\right) \tag{69}$$

The MIMO LE performance is measured using the relative RMSE between the deconvolved MIMO header and the original sequence. This metric indicates the accuracy of the co-antenna and inter-symbol interference removal process. In this case, the RMSE is given by:

$$\mathrm{RMSE}_{MIMO\_LE} = 20\log_{10}\left(\sqrt{\frac{\sum_{i=1}^{N_t}\sum_{m=1}^{N_{msg}}\sum_{k_m=\kappa_1+L}^{L_h-\kappa_2}\left|s_i^{est}\left(k_m\right)-s_i\left(k_m\right)\right|^2}{N_t N_{msg}\left(L_h-\left(\kappa_2+\kappa_1+L\right)\right)} \Big/ \frac{\sum_{i=1}^{N_t}\sum_{m=1}^{N_{msg}}\sum_{k_m=\kappa_1+L}^{L_h-\kappa_2}\left|s_i\left(k_m\right)\right|^2}{N_t N_{msg}\left(L_h-\left(\kappa_2+\kappa_1+L\right)\right)}}\right) \tag{70}$$

In order to evaluate the impact of the linear equalization on the received signals, RMSE_{MIMO_LE} is compared to another relative RMSE between emitted and raw received signals. This second metric is calculated by comparing the received MIMO header signal (prior to any interference removal) and the corresponding source signal,

$$\mathrm{RMSE}_{MIMO\_Raw} = 20\log_{10}\left(\sqrt{\frac{\sum_{i=1}^{N_t}\sum_{m=1}^{N_{msg}}\sum_{k_m=\kappa_1+L}^{L_h-\kappa_2}\left|\tilde{r}_i(k_m)-s_i(k_m)\right|^2}{N_t N_{msg}\left(L_h-(\kappa_2+\kappa_1+L)\right)}}{\frac{\sum_{i=1}^{N_t}\sum_{m=1}^{N_{msg}}\sum_{k_m=\kappa_1+L}^{L_h-\kappa_2}\left|s_i(k_m)\right|^2}{N_t N_{msg}\left(L_h-(\kappa_2+\kappa_1+L)\right)}}\right). \quad (71)$$

The performance estimated with the ICLE represents the theoretical performance limit of the MIMO LE. The relative RMSE between emitted MIMO sequences and the output of the ICLE is:

$$\mathrm{RMSE}_{MIMO\_ICLE} = 20\log_{10}\left(\sqrt{\frac{\sum_{i=1}^{N_t}\sum_{m=1}^{N_{msg}}\sum_{k_m=N_{ICLE}+K_{ICLE}}^{L_h-K_{ICLE}}\left|s_i^{ICLE}(k_m)-s_i(k_m)\right|^2}{N_t N_{msg}\left(L_h-(N_{ICLE}+2K_{ICLE})\right)}}{\frac{\sum_{i=1}^{N_t}\sum_{m=1}^{N_{msg}}\sum_{k_m=N_{ICLE}+K_{ICLE}}^{L_h-K_{ICLE}}\left|s_i(k_m)\right|^2}{N_t N_{msg}\left(L_h-(N_{ICLE}+2K_{ICLE})\right)}}\right). \quad (72)$$

In the case of perfect channel estimation, the RMSE at the output of the channel estimator is directly related to the SNR:

$$SNR = 10\log_{10}\left(RMSE_{CE}^2\right). \quad (73)$$

In the case of imperfect channel estimation, this equation can be rewritten by taking the noise induced by the channel estimator into consideration. In this case, we obtain:

$$\tilde{\mathbf{r}}_j = \mathbf{S}_j\tilde{\mathbf{h}}_j + \tilde{\mathbf{n}}_j + \tilde{\boldsymbol{\xi}}_j, \quad (74)$$

where $\tilde{\boldsymbol{\xi}}_j$ represents the noise samples induced by the channel estimation on receiver j. In our case, the SNR was obtained by taking the ratio of σ_s^2 over σ_n^2. Therefore, the relationship between the SNR and the RMSE given in the last equation should be rewritten as follows:

$$SNR = 10\log_{10}\left(RMSE_{CE}^2\right) + 10\log_{10}\left(\sigma_\xi^2\right), \quad (75)$$

where σ_ξ^2 is the variance of the noise induced by the channel estimator.

6. Experimental Summary

6.1 Hermes field demonstrations

6.1.1 Boston Harbor Experiment Using HULS-3

A series of rehearsal experiments were performed on May 13th and 14th 2010 in Boston Harbor, Massachusetts. The objective of this experiment was the testing of the Bluefin Robotics HULS-3 AUV equipped with the FAU Hermes acoustic modem. The vehicle was equipped with a high-resolution SMC DIDSON scan-sonar and on-board ATR and mosaicing capability, developed by SeeByte. The vehicle was operated off a small boat and scanned the sea floor. The Hermes acoustic modem transmitted high-resolution ATR images, mosaic images and vehicle status information. These data were transmitted individually or simultaneously via the pipe architecture. In addition, the acoustic downlink transmitted simple mission and modem commands. The data presented for May 13th, 2010 were collected at the dock of Research Vessel (RV) Resolution in Boston Harbor. Figure 17 shows an aerial view of the experiment. The GPS coordinate mark indicates the aft port position of the RV Resolution. A picture of the experimental setup is shown in Figure 18. Figure 19 shows the HULS-3 vehicle trajectory: In this case, the vehicle dove to a depth of 4.7m, moved to a target location and remained stationary. The water depth was 5m. A total of 334 uplink messages (3,046,080 data bits) were transmitted in mode 4 (46,668bps on a per-message basis) during this short mission. Four downlink command messages were also transmitted. The messages were processed in real-time and post-processed using the same multi-scale DFE technique, but with a wider, finer and slower search capability. The configuration parameters are shown in Table 6. The post-processing required up to 2 seconds per message.

Table 6: Real-Time and Post-Processed Multi-Scale DFE Parameter Settings, Boston Harbor Experiment.

Parameter	**First pass**	**Second pass**	**Second pass**
$N_p = 2$	**$n_p = 1$** (real-time and 2 sec/message max)	**$n_p = 2$** (real-time)	**$n_p = 2$** (2 sec/message max)
N_c	20	1	1
$f_{D,min}$ (Hz)	$f_{D,mean}$	$f_{D,mean} - 0.5$	$f_{D,mean} - 1.0$
$f_{D,max}$ (Hz)	$f_{D,mean}$	$f_{D,mean} + 0.5$	$f_{D,mean} + 0.5$
Δf_D (Hz)	0	0.5	0.25
λ_{min}	0.996	$\lambda(n_c)$-0.001	$\lambda(n_c)$-0.001
λ_{max}	0.998	$\lambda(n_c)$+0.001	$\lambda(n_c)$+0.001
$\Delta\lambda$	0.002	0.001	0.001
$n_{taps,min}$	-5	$n_{taps}(n_c)$-1	$n_{taps}(n_c)$-1
$n_{taps,max}$	40	$n_{taps}(n_c)$+1	$n_{taps}(n_c)$+1
Δn_{taps}	1	1	1
$t_{start,min}$	$10T_s$	$t_{start}(n_c)-T_s$	$t_{start}(n_c)-3T_s$
$t_{start,max}$	$30T_s$	$t_{start}(n_c)+T_s$	$t_{start}(n_c)+3T_s$
Δt_{start} (T_s = symbol duration)	$5T_s$	T_s	T_s

Figure 17: Bluefin dock and RV Resolution GPS location.

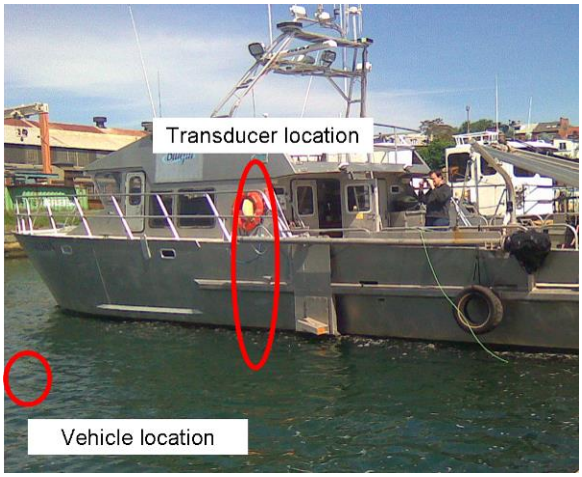

Figure 18: RV Resolution target ship for 05/13/2010 Hermes Modem test.

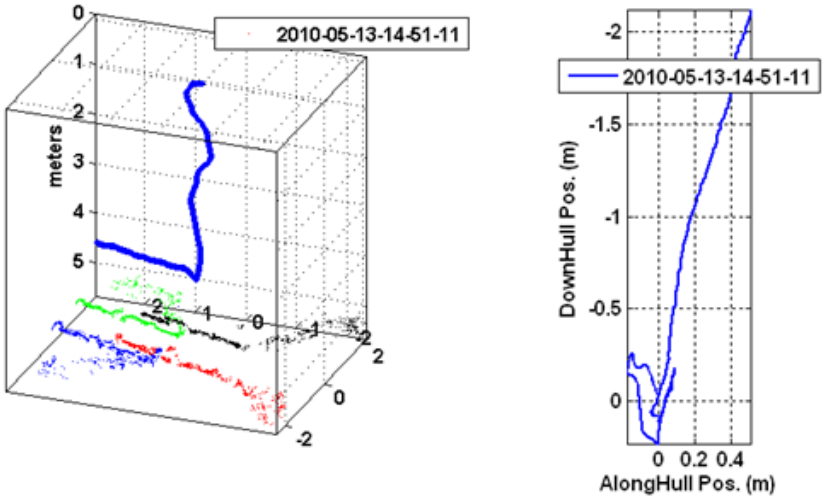

Figure 19: Boston Harbor vehicle trajectory, 05/13/2010.

Using the real-time uplink processing mode, the average BER was 1.0946%. 82.53% of the messages were received with a BER of 2% or less, at an average BER of 0.05873%. In the post-processed mode, the average BER dropped to 0.74555% (Figure 20). 88.45% of the messages were received with a BER of 2% or less, at an average BER of 0.00478%. During this mission, ATR, mosaic and status data were transmitted simultaneously. Figure 21 shows an example of SeeByte mosaic and ATR images transmitted during the mission.

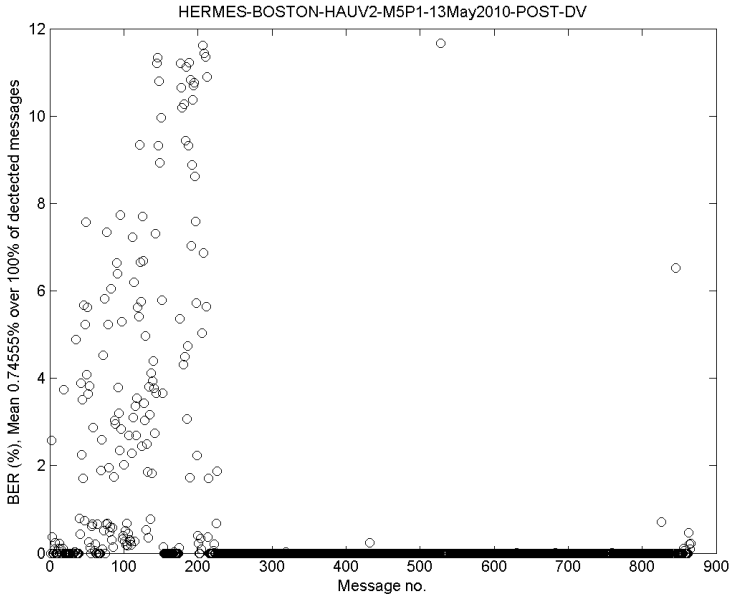

Figure 20: Measured BER, Boston harbor, 05/13/2010.

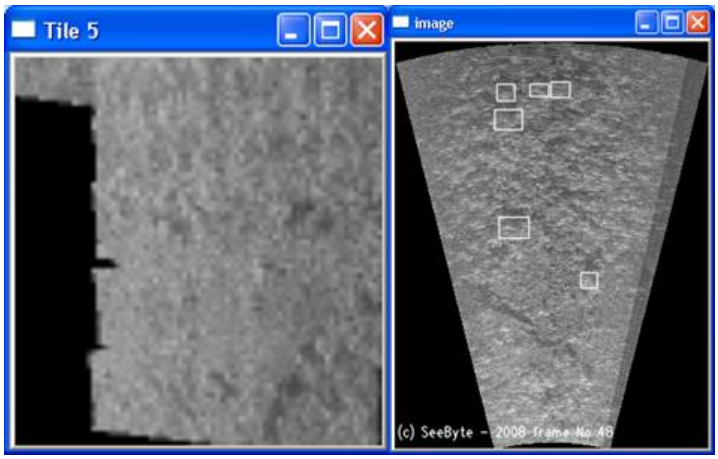

Figure 21: Example of mosaic (left) and ATR image (right) transmitted during the Boston harbor mission, 05/13/2010.

The data presented for May 14th, 2010 were collected at the Mystic pier in Boston Harbor. Figure 22 shows an aerial view of the experiment. Figure 23 shows the HULS-3 vehicle trajectory. In this case, the vehicle dove to a depth of 8 m (1 m off the bottom) and followed a farming pattern. The vehicle speed fluctuated between 0 and 0.4 m/s. A total of 401 uplink messages (3,657,120 data bits) were transmitted in mode 4 (46,668 bps on a per-message basis) during this mission. Five downlink command messages were also transmitted. As in the May 13th mission, the messages were processed in real-time and post-processed using the multi-scale DFE technique, using the same configuration parameters shown in Table 6. Using the real-time uplink processing mode, the average BER was 1.6253%. 63.59% of the messages were received with a BER of 2% or less, at an average BER of 0.4095%. In post-processing mode, the average BER dropped to 1.2128% (Figure 24). 72.82% of the messages were received with a BER of 2% or less, at an average BER of 0.4059%. During this mission, only ATR data were transmitted. Figure 25 shows an example of SeeByte ATR image transmitted during the mission.

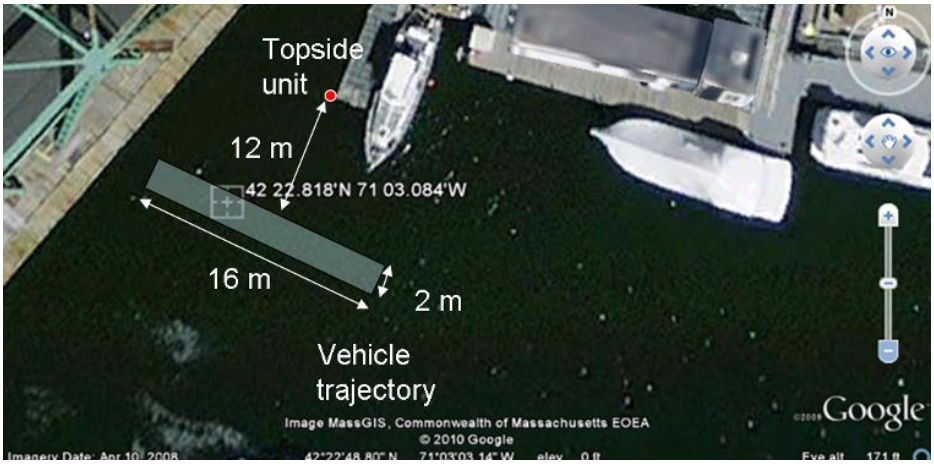

Figure 22: Aerial view of Mystic pier operations, 05/14/2010.

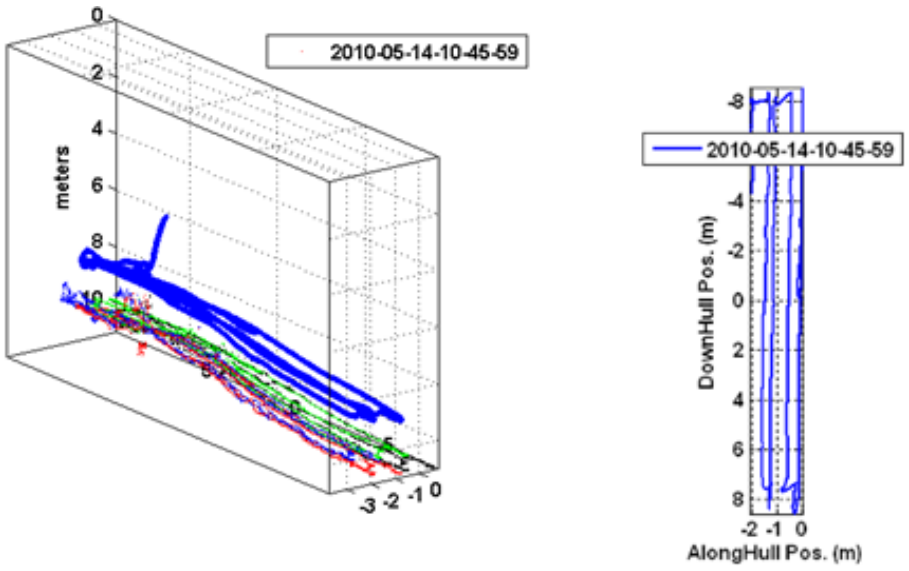

Figure 23: Vehicle trajectory, Mystic pier, 05/14/2010.

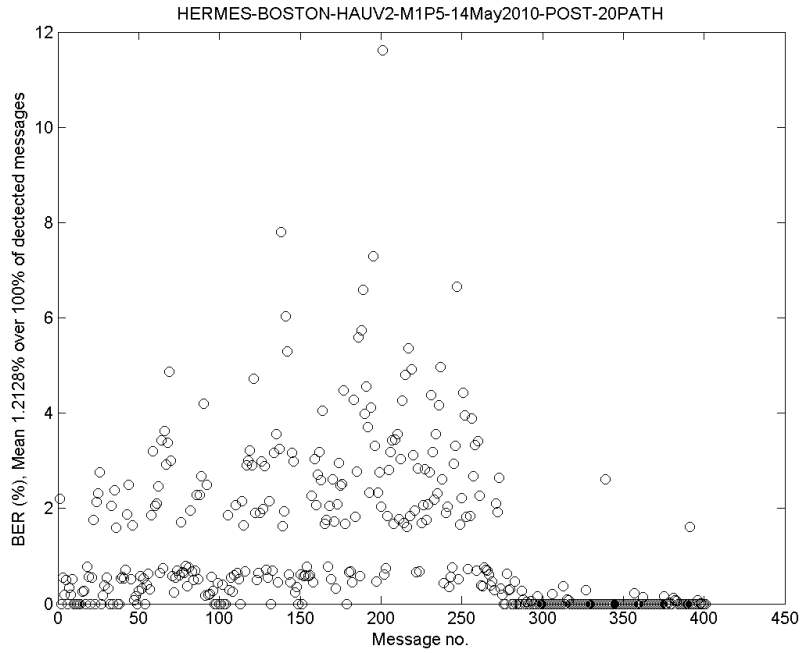

Figure 24: BER, post-processed mode, Mystic pier, 05/14/2010.

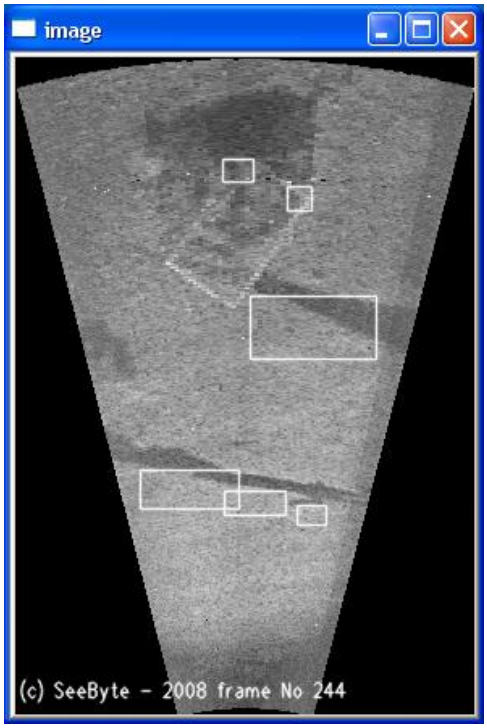

Figure 25: An example of nearly pristine ATR image received during the 05/14/10 mission, Mystic pier.

6.1.2 Newport News Experiment Using HULS-3

A series of experiments were performed from June 14th until June 18th 2010 in Newport News, Virginia. One of the objectives of this ONR-sponsored event was the testing of the Bluefin Robotics HULS-3 AUV, equipped with the FAU Hermes acoustic modem. The vehicle was equipped with a high-resolution SMC DIDSON scan-sonar and on-board ATR and mosaicing capability, developed by SeeByte. The vehicle was operated off a small boat and scanned the hull of a very large ship, the USNS Red Cloud. Specifically, the Hermes acoustic modem transmitted high-resolution ATR images, mosaic images and vehicle status information. These data were transmitted simultaneously via the pipe architecture. In addition, the acoustic downlink transmitted simple mission and modem commands. The data presented here were collected on June 14th and 18th, 2010.

As in the Boston Harbor case, the messages were processed in real-time and post-processed using the same multi-scale DFE technique, but with a wider and finer (and slower) search capability. The configuration parameters shown in Table 7 were used. The post-processing required up to 2 seconds per message. The results for June 14th focus on a specific mission where the data were transmitted at the highest possible data rate (mode 5, or 87,768bps measured across a 104ms message). At the beginning of this mission, the transmission mode (mode 4 to mode 5) was changed during operations using an acoustic downlink command. In mode 5, 10,041,120 data bits (1,101 messages) were transmitted at a distance of up to 52m, the maximum distance to the vehicle during the mission (52m is not the maximum range of the acoustic uplink in mode 5). Twelve command messages were also sent to the vehicle using the acoustic downlink. Using the real-time mode, 36.07% of the messages were received with a BER

of 2% or less (at an average BER of 0.45673%). At a range of 40m to 52m, 43.46% of the messages were received with a BER of 2% or less (at an average BER of 0.2137%).

Table 7: Real-Time and Post-Processed Multi-Scale DFE Parameter Settings, Newport News Experiment.

Parameter	**First pass**	**Second pass**	**Second pass**
$N_p = 2$	**$n_p = 1$** (real-time and 2 sec/message max)	**$n_p = 2$** (real-time)	**$n_p = 2$** (2 sec/message max)
N_c	10	1	1
$f_{D,min}$ (Hz)	$f_{D,mean}$	$f_{D,mean} - 0.5$	$f_{D,mean} - 1.0$
$f_{D,max}$ (Hz)	$f_{D,mean}$	$f_{D,mean} + 0.5$	$f_{D,mean} + 0.5$
Δf_D (Hz)	0	0.5	0.25
λ_{min}	0.996	$\lambda(n_c)-0.001$	$\lambda(n_c)-0.001$
λ_{max}	0.998	$\lambda(n_c)+0.001$	$\lambda(n_c)+0.001$
$\Delta\lambda$	0.002	0.001	0.001
$n_{taps,min}$	-5	$n_{taps}(n_c)-1$	$n_{taps}(n_c)-1$
$n_{taps,max}$	40	$n_{taps}(n_c)+1$	$n_{taps}(n_c)+1$
Δn_{taps}	1	1	1
$t_{start,min}$	$15T_s$	$t_{start}(n_c)-T_s$	$t_{start}(n_c)-3T_s$
$t_{start,max}$	$30T_s$	$t_{start}(n_c)+T_s$	$t_{start}(n_c)+3T_s$
Δt_{start}	$5T_s$	T_s	T_s
(T_s = symbol duration)			

The results for June 18th focus on a specific mission where the data were transmitted at the longest possible range in mode 4 (46,668bps on a per-message basis). In this mission, the HULS-3 vehicle moved toward the stern of USNS Red Cloud. It began the mission at a distance of 50m and traveled to a range of 130m (the limit of the fiber optic tether). An aerial view of the experiment is shown in Figure 26.

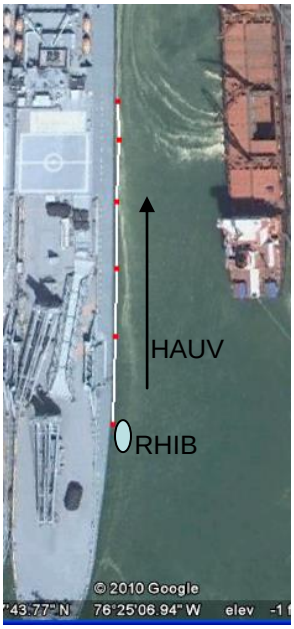

Figure 26: Aerial view, Newport News, 06/18/10.

The recorded vehicle trajectory is shown in Figure 27. 11,956,320 data bits (1311 messages) were transmitted in mode 4. Fourteen command messages were also sent to the vehicle.

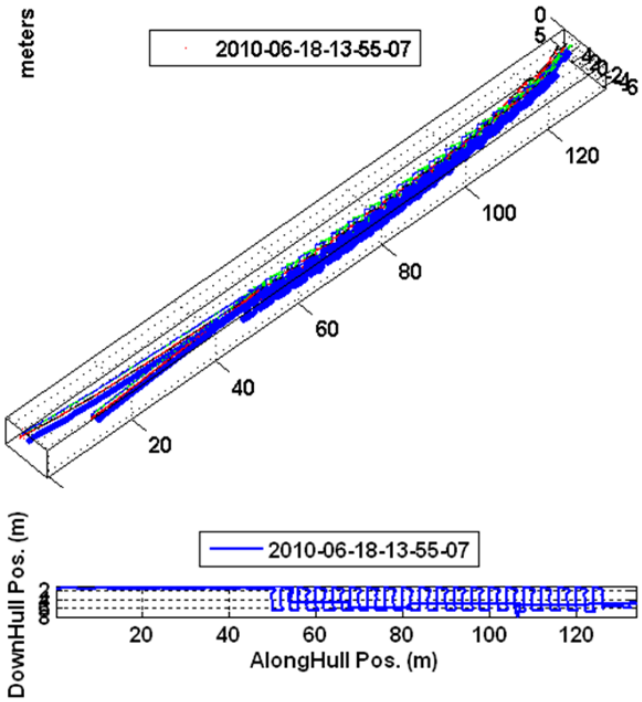

Figure 27: Vehicle trajectory, Newport News, 06/18/10.

Using the real-time mode, 81.42% of the messages were received with a BER of 2% or less (at an average BER of 0.23957%). The estimated BER for each message, using the post-processing mode, is shown in Figure 28. 81.24% of the messages were received with a BER of 2% or less (at an average BER of 0.23812%). The first 100 messages were measured while the vehicle was still at the surface with the source transducer barely submerged. Past the first 100 messages, 86.06% of the messages were received with a BER of 2% or less (at an average BER of 0.2038%). In this case, the communication was of such quality that little benefit came of using the slower post-processed mode.

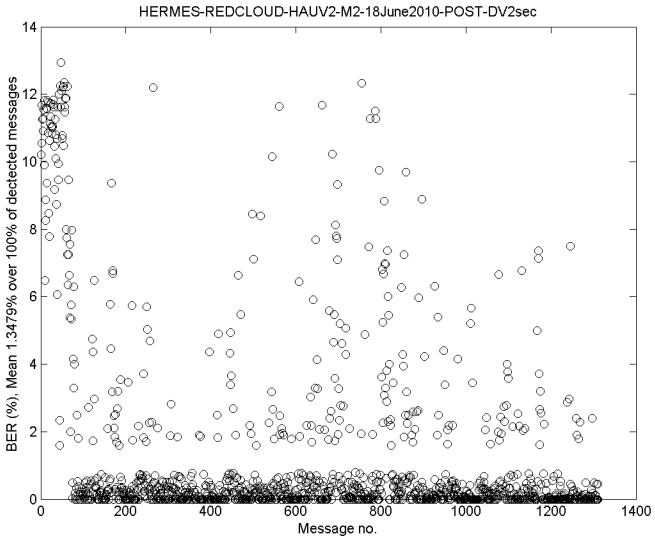

Figure 28: BER, Newport News, 06/18/10.

6.1.3 WHOI Experiment Using Remus-100 Gudgeon

The objective of this experiment was twofold: (1) the functional test of the newly developed Hermes module for the REMUS-100 and (2) the real-time transfer of Blueview sonar images during vehicle operation. The AUV platform was the WHOI Gudgeon (Figure 3), a REMUS-100 specially equipped with bow thrusters and capable of hovering. The experiment took place on Jun 25th 2010 along the WHOI dock (Figures 29 and 30). The preliminary results presented here were collected at a distance of 30m. Five separate data collections were performed during separate 10min missions. A single-image Blueview *.son* file was transmitted periodically, interleaved with test sequences. Because of the large sonar file size and the limited duration of the experiment, only a limited number of images were transmitted.

Although the operational conditions were ideal and the range was limited, a very dense school of bait fish posed a new challenge to the Hermes acoustic communications system. In short, both source and receiver were surrounded with tens of thousands of bait fish, which produced a large amount of volume scattering. Attempts to photograph the biological activity were unsuccessful. As a result of the interference, the communication performance dropped as compared with the earlier experiments in Norfolk. However, this experiment was also an excellent opportunity to show the benefits of the multi-scale candidate search approach. Figure 31 shows the measured

BER during the last mission using the low-resolution results obtained in real-time. Figure 32 shows the BER measured during the same mission with a much refined resolution. The multi-scale parameters are shown in Table 8.

On average, the BER obtained in the first case is 4.54%, vs. 2.72% in the second case. In the first case, only 15.85% of the messages are received with a BER of 2% or less, and at an average of 0.86%. Using the higher-resolution mode, 33.83% of the messages are received with a BER of 2% or less, and at an average of 0.75%. This dramatic increase in performance comes at the cost of processing time: the processing of an individual message can take up to 120 seconds using the high-resolution mode (using a single 2.4GHz Intel processor). The authors are working to reduce the processing time through improved parallel computation.

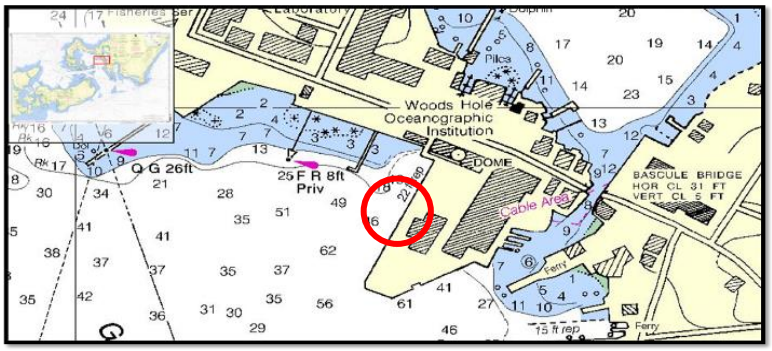

Figure 29: Aerial view of the WHOI experiment, 06/25/10.

Figure 30: Boat view of the WHOI experiment, 06/25/10.

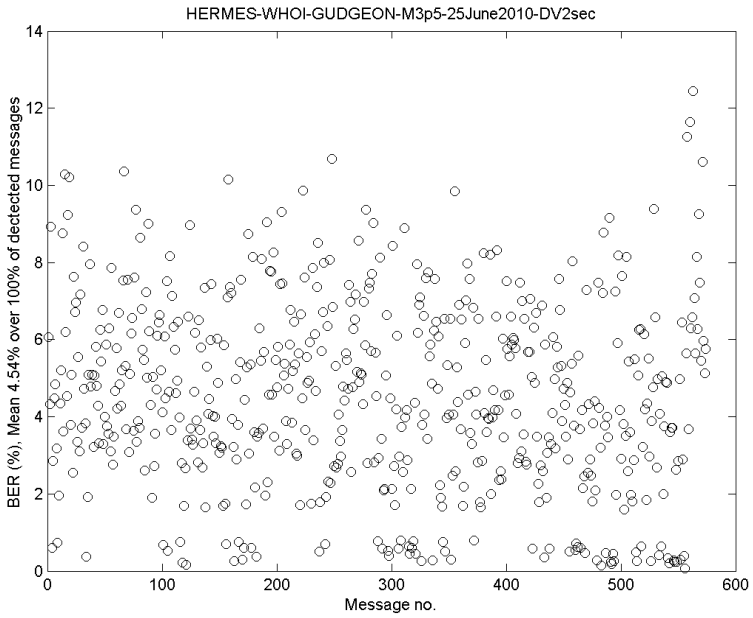

Figure 31: BER measured using fast post-processing (up to 2 second/message), WHOI mission, 06/25/10.

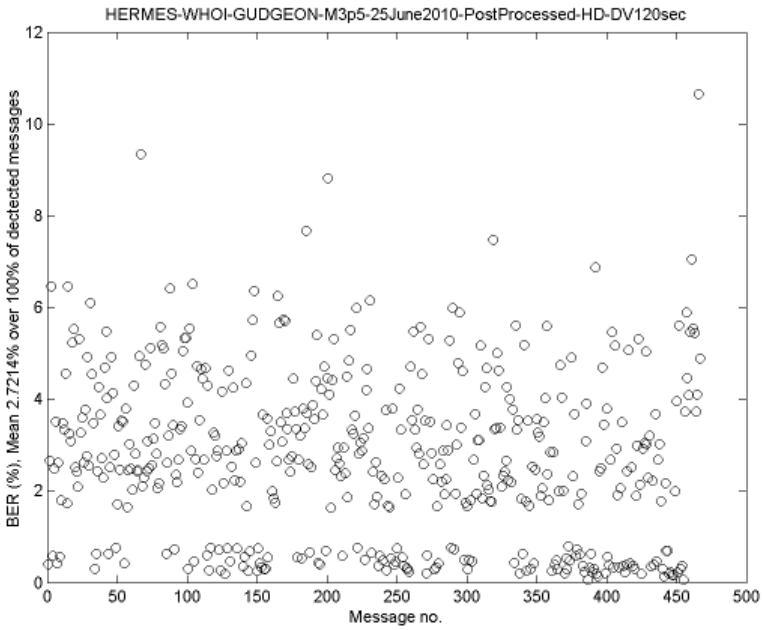

Figure 32: BER measured using slow post-processing (up to 120 second/message), WHOI mission, 06/25/10.

Table 8: Real-Time and Post-Processed Multi-Scale DFE Parameter Settings, WHOI Experiments.

Parameter	**First pass**	**Second pass**	**Second pass**
N_p = 2	**n_p = 1** (2s and 120s/message)	**n_p = 2** (2s/message max)	**n_p = 2** (120s/message max)
N_c	10	1	1
$f_{D,min}$ (Hz)	$f_{D,mean}$	$f_{D,mean}$ – 1.0	$f_{D,mean}$ – 0.5
$f_{D,max}$ (Hz)	$f_{D,mean}$	$f_{D,mean}$ + 0.5	$f_{D,mean}$
Δf_D (Hz)	0	0.25	0.25
λ_{min}	0.996	$\lambda(n_c)$-0.001	0.995
λ_{max}	0.998	$\lambda(n_c)$+0.001	0.999
$\Delta\lambda$	0.002	0.001	0.001
$n_{taps,min}$	-5	$n_{taps}(n_c)$-1	$n_{taps}(n_c)$-10
$n_{taps,max}$	40	$n_{taps}(n_c)$+1	$n_{taps}(n_c)$+10
Δn_{taps}	1	1	1
$t_{start,min}$	$15T_s$	t_{start} (n_c)-$3T_s$	t_{start} (n_c)-$5T_s$
$t_{start,max}$	$35T_s$	t_{start} (n_c)+$3T_s$	t_{start} (n_c)+$5T_s$
Δt_{start} (T_s=symbol duration)	$5T_s$	T_s	$2T_s$

6.1.4 Battleship Cove, MA, December 2010 (Hiddensee)

This field experiment consisted in a series of functional tests. HULS-3 mostly operated under the propellers and rudder of the target ship (Hiddensee) and transmitted status and SeeByte 3D reconstruction of the hull using Hermes. The experiment took place from 12/01/2010 until 12/03/2010. The water depth was 7 m, the vehicle top speed was 0.2 m/s and the vehicle range to Hermes topside unit varied from 1 m to 40 m. Uplink messages were transmitted in mode 4 at a rate of 1 message per 1.5 second. 1 downlink message was transmitted per 100 uplink messages. Figure 33 shows the ship and some of the salient results obtained during the experiment.

The following is a day-by-day operations summary:

- Day 1: 8 missions
  - *Missions 1 to 6: short hardware configuration missions.*
  - *Missions 7 and 8: CA using 3D reconstruction.*
- Day 2: 8 missions (CA with narrow legs at 0.2 m/s)
  - *Missions 1 and 2: status only.*
  - *Missions 3 to 8: 3D reconstruction and status.*
- Day 3: 6 missions (CA only).

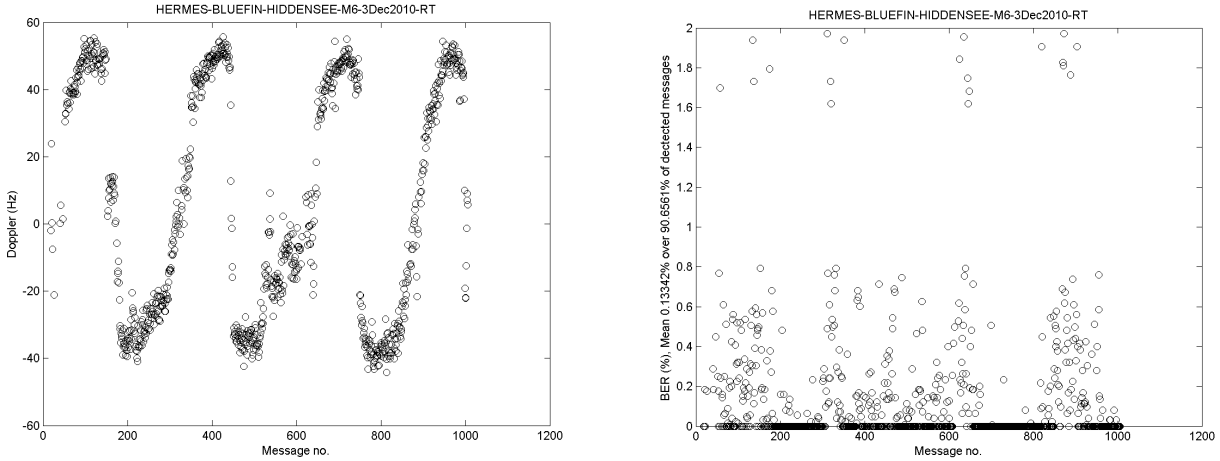

Figure 33: Top: aerial view of Hiddensee at the Battleship Cove (left), HULS-3 trajectories during a stern (center) and hull survey (right); bottom: Hermes uplink performance during this mission.

6.1.5 San Diego, CA, February 2011 (SS Curtiss)

This field experiment was a series of preparation tests followed with a live demo to distinguished visitors. During CA missions, HULS-3 operated either under the propellers and rudder of the target ship (SS Curtiss) and transmitted status and SeeByte 3D reconstruction of the hull using Hermes. During hull search NCA missions, HULS-3 operated either under the hull of the target ship (away from the propeller and rudder) and transmitted status and SeeByte 2D ATR images using Hermes. The experiment took place from 02/04/2011 until 02/11/2011. The water depth was 17 m, the vehicle top speed was 0.2 m/s and the vehicle range to Hermes topside unit varied from 1 m to 80 m. Uplink messages were transmitted in mode 4 at a rate of either 1 message per 1.5 second or 3 messages per 2 seconds. 1 downlink message was transmitted per 200 uplink messages. Figures 34 to 38 show the ship and some of the salient results obtained during the experiment.

The following is a day-by-day operations summary:

- Day 1 (02/04/11):
  - *Mission 1: CA stern search with transmission of 3D reconstruction data and vehicle status.*
  - *Mission 2: NCA hull search with transmission of 2D ATR images and vehicle status.*
- Day 2 (02/05/11):
  - *Mission 1: NCA hull search with transmission of 2D ATR images and vehicle status.*
  - *Mission 2: CA stern search with transmission of 3D reconstruction data and vehicle status.*
- *Day 3 (02/08/11): one NCA hull search mission with transmission of 2D ATR images and vehicle status. At the end of the last mission, the acoustic uplink source transducer was accidentally damaged. No further data were collected past 02/08/2011.*

Figure 34: Top: aerial view of the SS Curtiss.

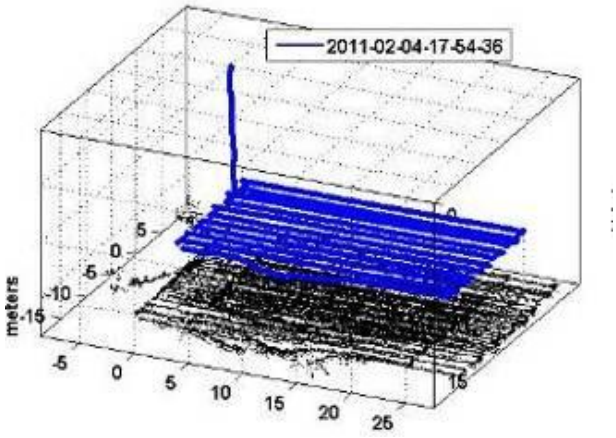

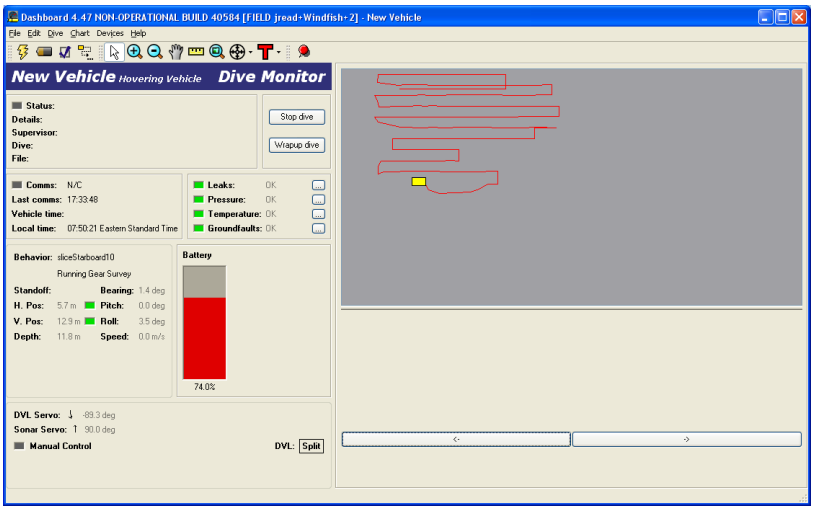

Figure 35: HULS-3 trajectory during a CA stern inspection (top); Bluefin Dashboard displaying the information received with Hermes during a CA stern inspection (bottom). The stern inspection was mission 1 on 02/04/2011.

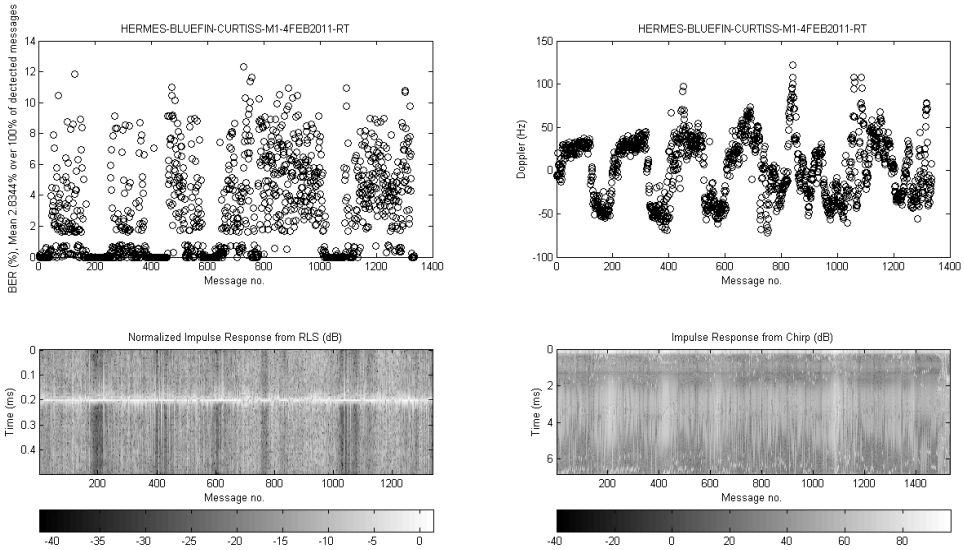

Figure 36: Hermes uplink performance during the CA stern inspection.

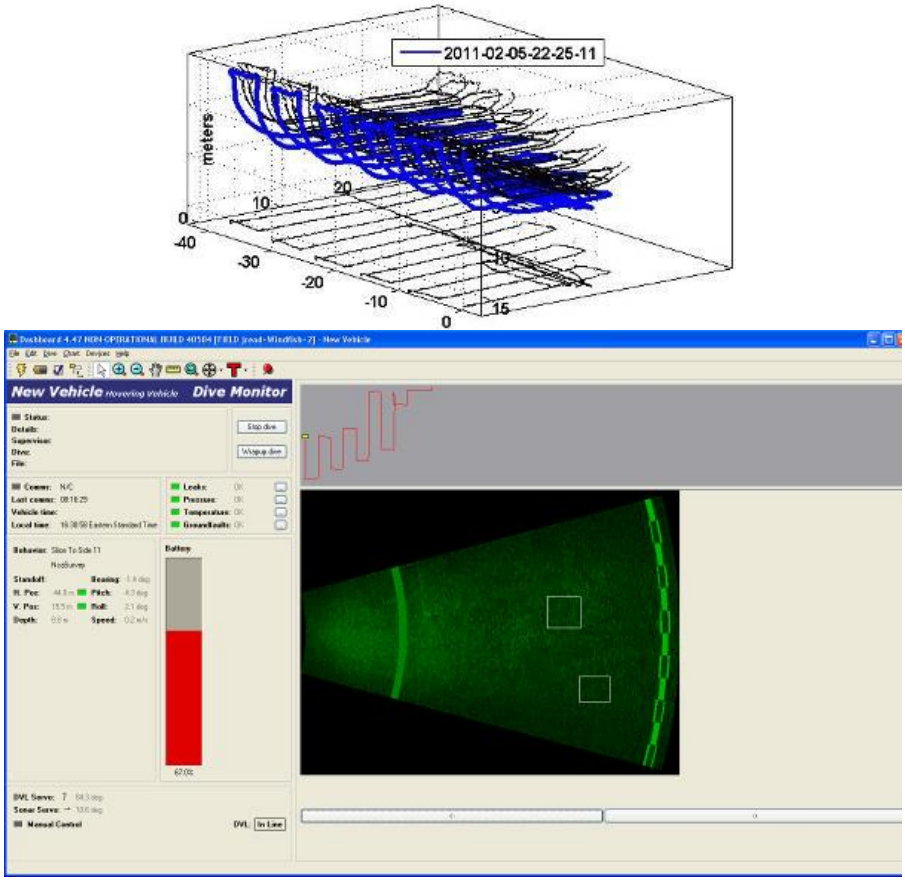

Figure 37: HULS-3 trajectory during a a hull inspection (top); center and bottom left; Bluefin Dashboard displaying the information received with Hermes during the same hull inspection (bottom). The hull inspection was mission 2 on 02/04/2011.

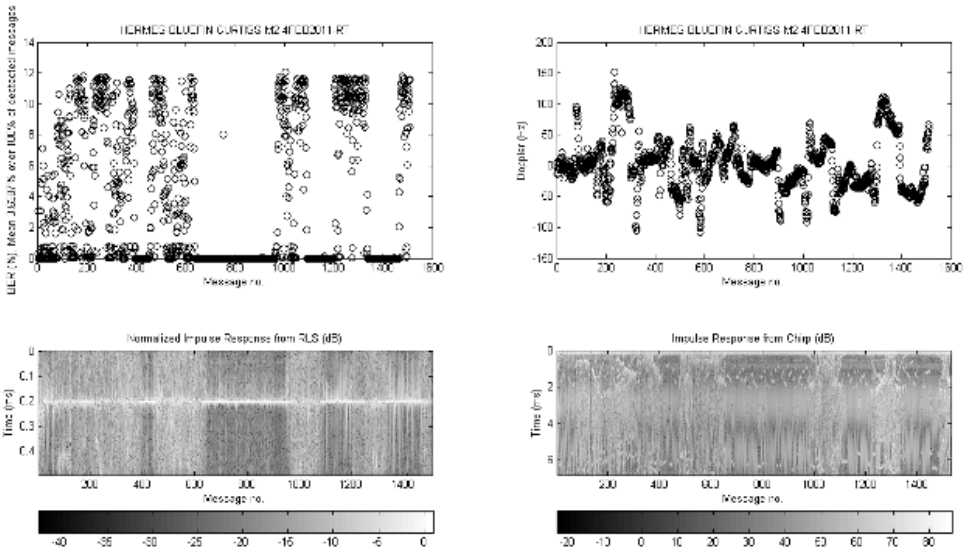

Figure 38: Hermes uplink performance during the hull inspection.

6.1.6 Battleship Cove, MA, April 2011 (Hiddensee)

This one-afternoon field experiment (04/22/2011) was in preparation of the US Coast Guard Station demo in Boston. HULS-3 completed 2 missions under the propellers and rudder of the target ship (Hiddensee) and transmitted status and SeeByte 3D reconstruction of the hull using Hermes. The water depth was 7 m, the vehicle top speed was 0.2 m/s and the vehicle range to Hermes topside unit varied from 1 m to 20 m. Uplink messages were transmitted in mode 4 at a rate of 1 message per 1.5 second. 1 downlink message was transmitted per 200 uplink messages. Figures 39 to 41 show the ship and some of the salient results obtained during mission 2 on the experiment 04/22/2011.

Figure 39: Aerial view of Hiddensee at the Battleship Cove (MA).

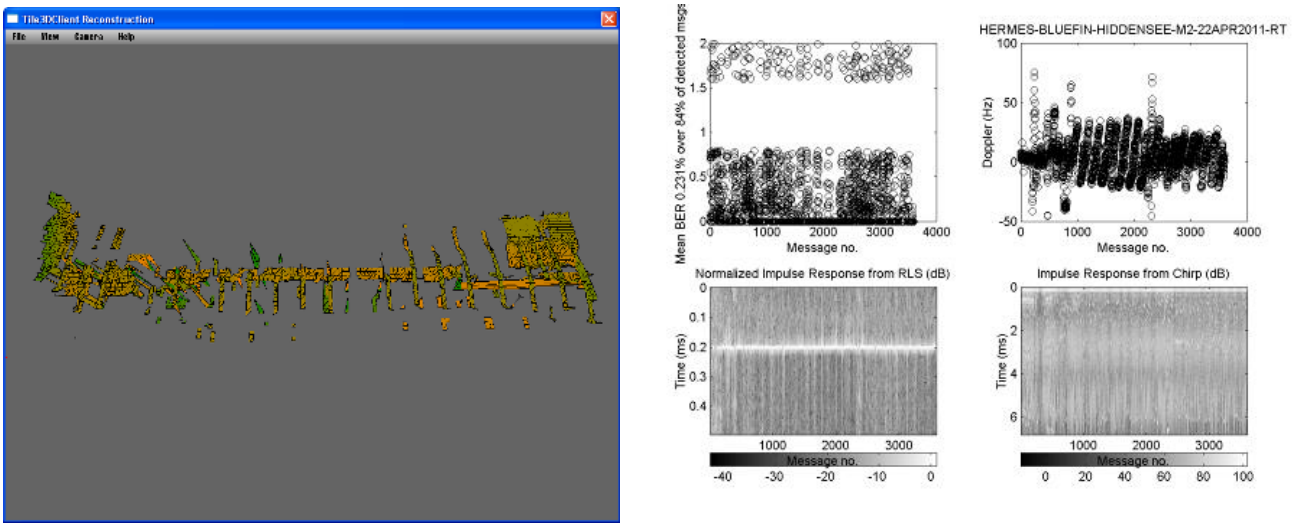

Figure 40: Left: SeeByte 3D reconstruction transmitted with Hermes during the hull and stern inspections; Right: Hermes uplink performance during this mission..

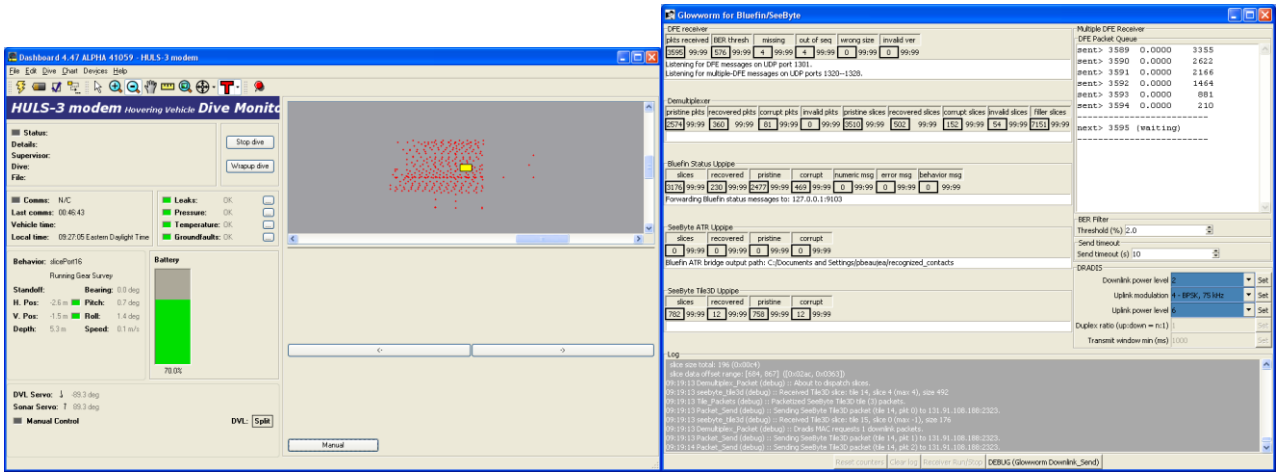

Figure 41: Left: Bluefin Dashboard displaying the information received with Hermes during the mission; Right: a snapshot of Hermes message traffic GUI.

6.1.7 US Coast Guard Station, Boston, MA, April 2011 (USCGC Seneca)

This field experiment was a series of preparation tests followed with a live demo to distinguished visitors. During CA search missions, HULS-3 operated either under the propellers and rudder of the target ship (USCGC Seneca) and transmitted status and SeeByte 3D reconstruction of the hull using Hermes. During NCA hull search missions, HULS-3 operated either under the hull of the target ship (away from the propeller and rudder) and transmitted status and SeeByte 2D ATR images using Hermes. During all these missions, the vehicle was occasionally controlled with the MIT backseat driver. The experiment took place from 04/25/2011 until 04/28/2011. The water depth was 13 m, the vehicle top speed was 0.2 m/s and the vehicle range to Hermes topside unit

varied from 1 m to 95 m. Uplink messages were transmitted in mode 4 at a rate of either 1 message per 1.5 second or 3 messages per 2 seconds. 1 downlink message was transmitted per 200 uplink messages. Figure 42 shows the ship and some of the salient results obtained during the experiment.

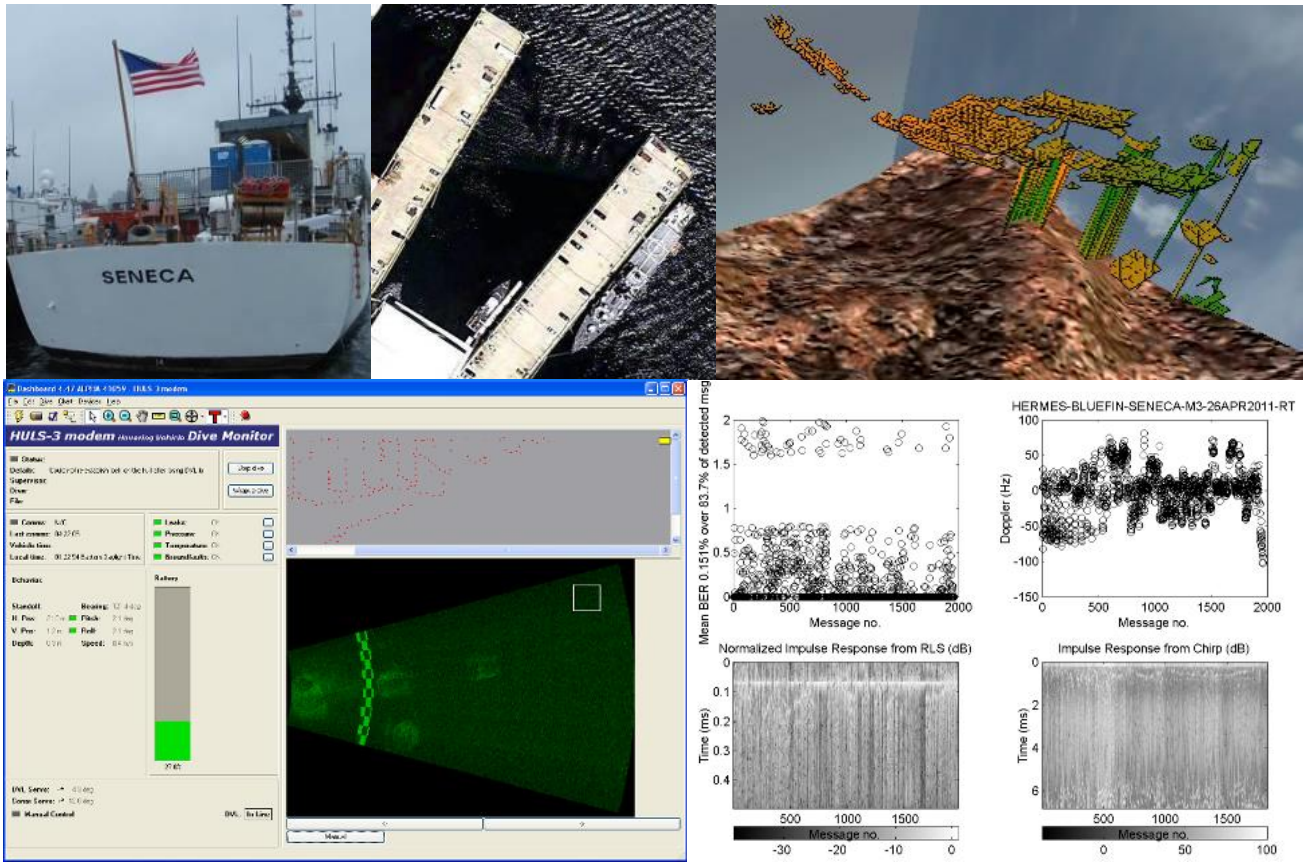

Figure 42: Top left and center: stern of the USCGC Seneca and aerial view of the test location; top right: SeeByte 3D reconstruction transmitted with Hermes during the stern inspections; bottom left: Bluefin Dashboard displaying the information received with Hermes during the mission; bottom right: Hermes uplink performance during the hull inspection. The hull inspection was mission 3 on 04/26/2011. The stern inspection was mission 4 on 04/26/2011.

The following is a day-by-day operations summary:

- Day 1:
  - *Mission 1: CA stern search with transmission of 3D reconstruction data and vehicle status.*
  - *Missions 2-5: NCA hull search with transmission of 2D ATR images and vehicle status.*
- Day 2:
  - *Missions 1-3: NCA hull search with transmission of 2D ATR images and vehicle status.*
  - *Missions 4-9: CA stern search with transmission of 3D reconstruction data and vehicle status.*
- Day 3:
  - *Missions 1-2: NCA hull search with transmission of 2D ATR images and vehicle status.*
  - *Missions 3-5: CA stern search with transmission of 3D reconstruction data and vehicle status.*
- *Day 4: visitor demo.*
  - *Missions 1-2: NCA hull search with transmission of 2D ATR images and vehicle status.*

- *Missions 3-4: CA stern search with transmission of 3D reconstruction data and vehicle status.*

6.1.8 NSWC, Panama City, FL, June 2011 (Bordelon)

This field experiment was a series of preparation tests followed with a live demo to distinguished visitors. During CA search missions, HULS-3 operated either under the propellers and rudder of the target ship (SS Curtiss) and transmitted status and SeeByte 3D reconstruction of the hull using Hermes. During NCA hull search missions, HULS-3 operated either under the hull of the target ship (away from the propeller and rudder) and transmitted status and SeeByte 2D ATR images using Hermes. During all these missions, the vehicle was occasionally controlled with the MIT backseat driver. The experiment took place from 04/25/2011 until 04/28/2011. The water depth was 17 m, the vehicle top speed was 0.2 m/s and the vehicle range to Hermes topside unit varied from 1 m to 30 m. Uplink messages were transmitted in mode 4 at a rate of either 1 message per 1.5 second or 3 messages per 2 seconds. 1 downlink message was transmitted per 200 uplink messages. Figure 43 shows the ship and some of the salient results obtained during the experiment.

The following is a day-by-day operations summary:

- Day 1 (06/17/2011):
  - *Mission 1-3: CA stern search with transmission of 3D reconstruction data and vehicle status.*
  - *Missions 4: NCA hull search with transmission of 2D ATR images and vehicle status.*
- Day 2 (06/18/2011):
  - *Missions 1-4: NCA hull search with transmission of 2D ATR images and vehicle status.*
  - *Missions 5-7: CA stern search with transmission of 3D reconstruction data and vehicle status.*
- Day 3 (06/20/2011):
  - *Missions 1: NCA hull search with transmission of 2D ATR images and vehicle status.*
  - *Missions 2-3: CA stern search with transmission of 3D reconstruction data and vehicle status.*
- *Day 4 (06/21/2011): visitor demo.*
  - *Missions 1: NCA hull search with transmission of 2D ATR images and vehicle status.*
  - *Missions 2: CA stern search with transmission of 3D reconstruction data and vehicle status.*
  - *Missions 3: NCA hull search with transmission of 2D ATR images and vehicle status.*
  - *Missions 4: CA stern search with transmission of 3D reconstruction data and vehicle status.*
- *Day 5 (06/22/2011):*
  - *Missions 1-3: CA stern search with transmission of 3D reconstruction data and vehicle status.*
- *Day 6 (06/23/2011): visitor demo.*
  - *Missions 1-5: CA stern search with transmission of 3D reconstruction data and vehicle status.*

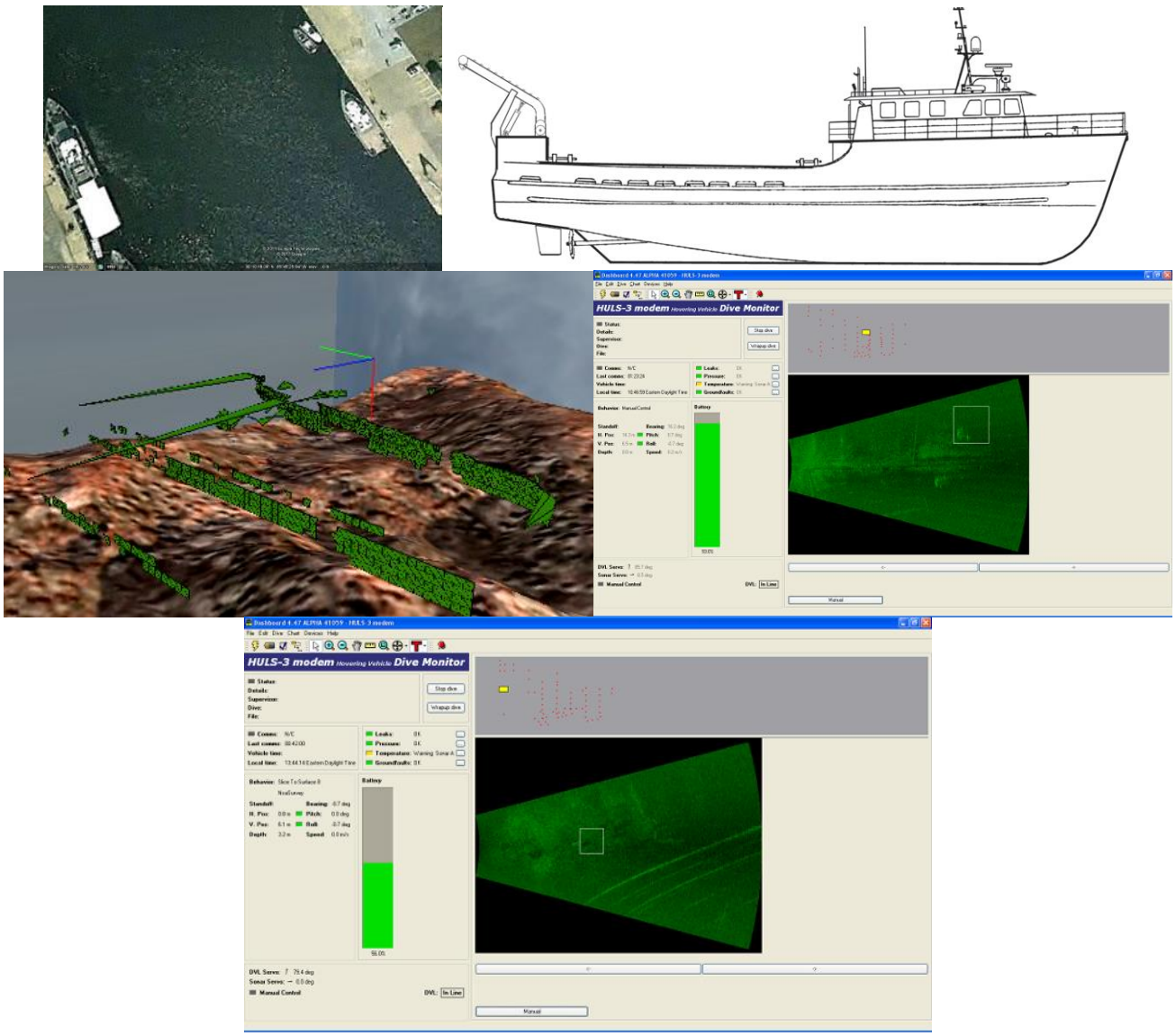

Figure 43: Top left and center: aerial view of the test location and M/V Will Bordelon; top right: SeeByte 3D reconstruction transmitted with Hermes during the stern inspections; bottom: Bluefin Dashboard displaying the information received with Hermes during the mission. The hull inspection was mission 3 on 06/21/2011. The stern inspection was mission 4 (curtain mission) on 06/22/2011.

6.2 Doppler tracking

The experimental setup consisted of a towing carriage that moves at a user defined velocity on the Tow Tank. The tank setup in the Hydrodynamics laboratory of FAU SeaTech was used for indoor experiments (Figure 44 and 45). It measured about 18 m x 1.2 m x 1.2 m. The tank had a tow carriage attached on the top surface of the tank and moved smoothly over the rim of the tank. The movement of the tow carriage was controlled by a stepper motor.

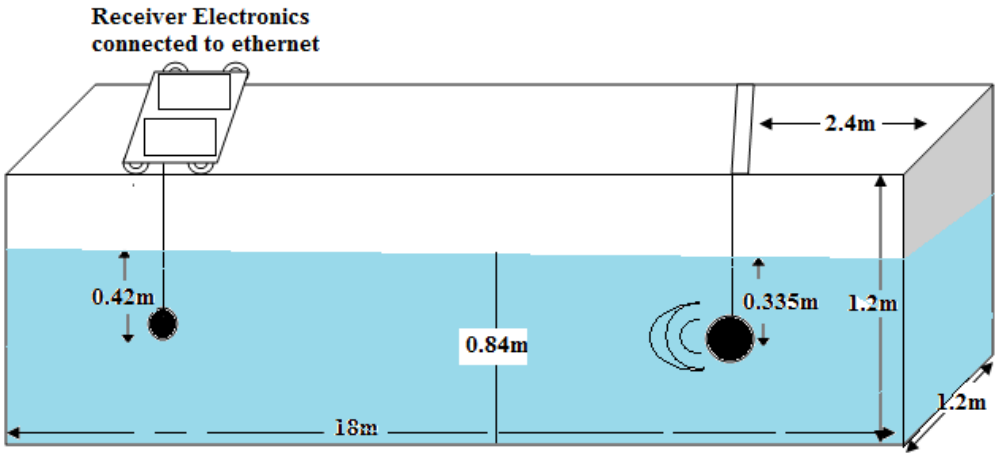

Figure 44: Tow Tank Setup.

The receiver hydrophone was attached to the tow carriage. The tow carriage produced a back and forth movement with respect to a stationary acoustic source that was suspended at about 0.335 m below the water surface. The distance between the source and the receiver was varied between 1.3 m to 8.4 m. The receiver was immersed at a depth of 0.42 m. The water level in the tank was 0.84 m.

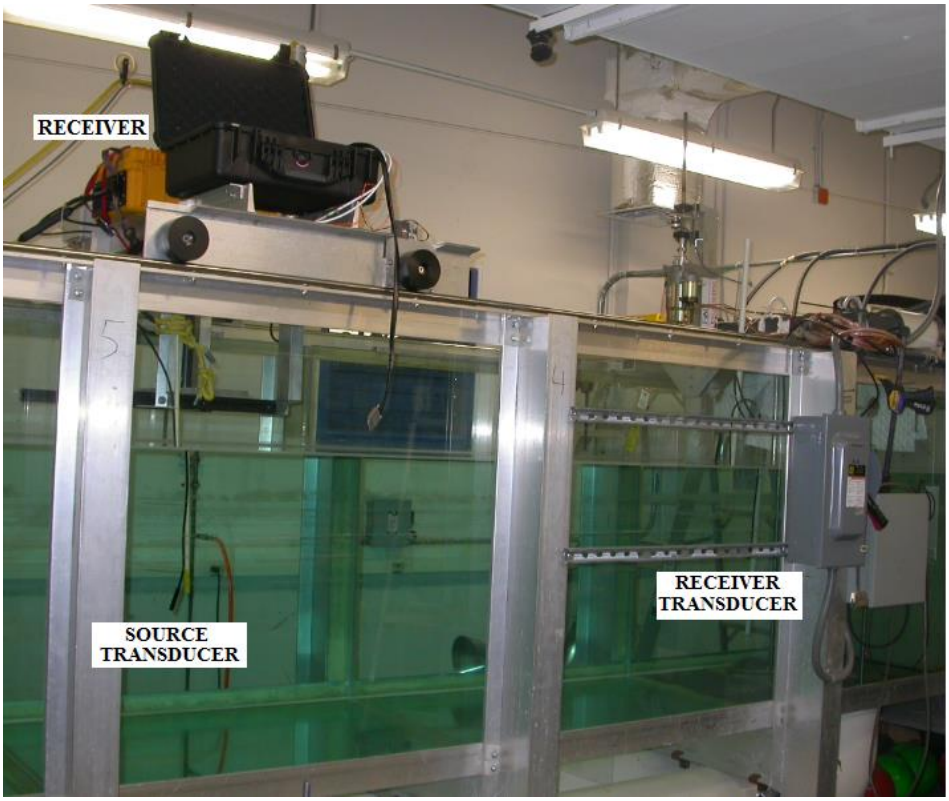

Figure 45: Test Setup in the Tow Tank.

The experiment was carried out in January 2011. The source was at first stationary at a distance of 2.4 m from one end of the tank. The source transducer was immersed at a depth of 0.36 m. The receiver hydrophone was attached to the towing carriage and immersed at a depth of 0.42 m. The towing carriage moved to and from the source at a peak velocity ranging between 0.2 knots to 1 knot. The laptop connected to the Hermes receiver unit stored the received signals. The laptop connected to the tow carriage recorded its velocity. Figure 46 shows the velocity profile generated from the movement of the tow carriage above the tank. The tow carriage started from rest and came to rest before a change in direction.

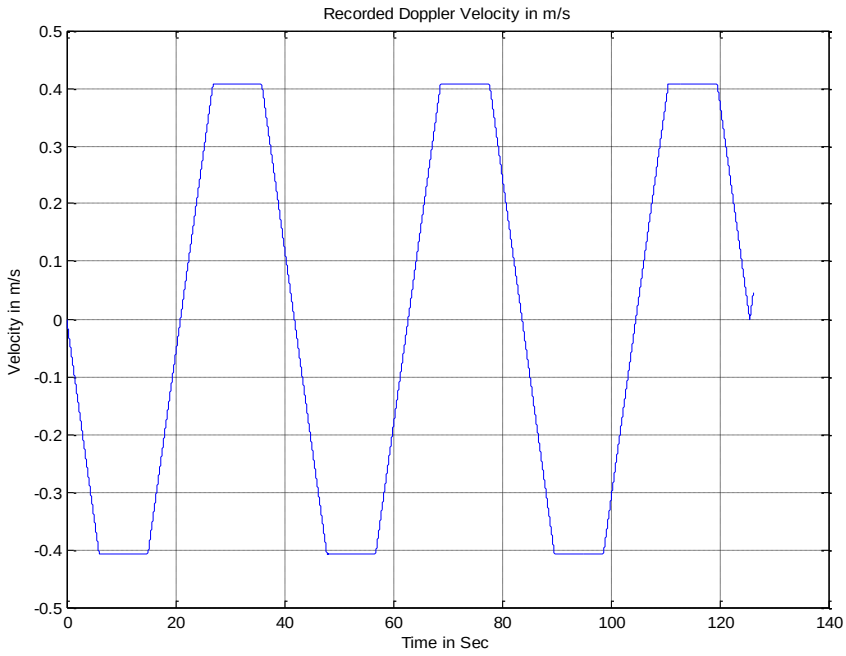

Figure 46: Recorded Velocity of the Tow Carriage.

The estimation results for the Doppler velocity were generated after the post processing of the received tone files. The real time velocity recordings and the data collection by the acoustic modem source was not time synchronized. Figure 47 shows the average velocity estimated across every individual tone file (once every 0.6 s).

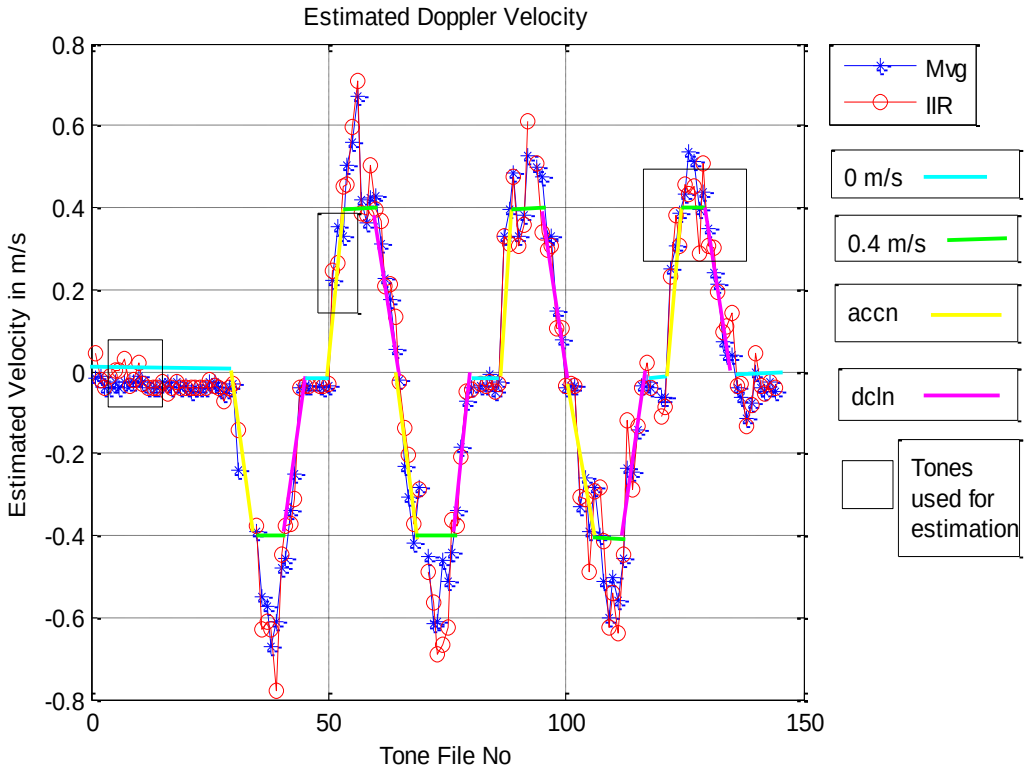

Figure 47: Estimated Doppler Velocity values from the Received Signal Tone.

The estimates closely followed the actual trend from Figure 46. The exact RMSE for the estimation methods could only be provided in parts of the test due to limited synchronization accuracy between the recorded and estimated Doppler values. The points of rest of the tow carriage could also be observed. The discontinuities observed in the graphs are due to the loss of tone files during transmission. Due to internal clock offset, the frequency of the pilot tone at 375 kHz has a small offset of 10 Hz equivalent to 0.04 m/s.

6.3 Single input multiple output uplink

The experimental results presented in this report are obtained using the proposed SIMO techniques. The data were recorded at the FAU Sea Tech marina in Port Everglades, Florida. Due to the equipment constraints the experiment was conducted using one source and one receiver. The source transmitted multiple messages at distance between 25 m and 160 m from the receiver. The post processing of the data is performed in a manner that different distances between the source and receiver are considered as one source and multiple receivers positioned at these distances receiving messages with different time delays. The positions of the source and receiver during the experiment and the bathymetry at low tide are given in Figure 48.

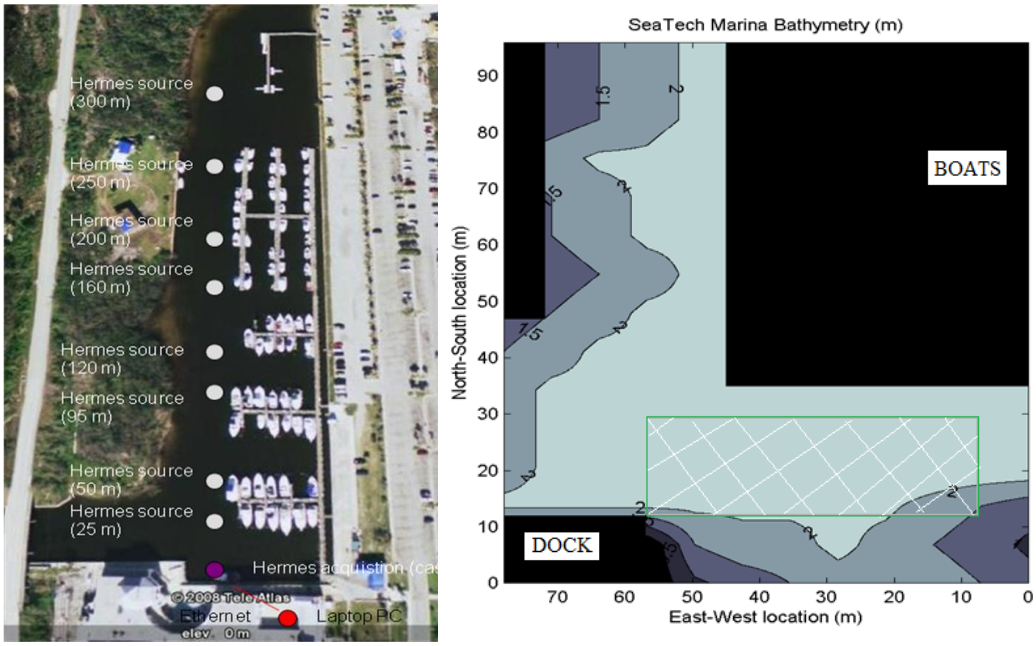

Figure 48: Left: Source and receiver positions. Right: Bathymetry at low tide, Port Everglades, Florida.

The sea bottom was a combination of mud and sand and the water depth was about 2 m. The source and receiver transducers were placed about 1m below the surface with the distance between them of 25 m, 50 m, 80 m, 95 m, 120 m and 160 m. The experiment was performed in a non-controlled environment in terms of biological life and boat traffic. The MSDFE was configured to use three candidates, the value of the forgetting factor was set to be 0.999, and the number of feed forward taps ranged between 15 and 40, with step size of 5. The source transmitted BPSK modulated messages at 25 kHz, 50 kHz and 75 kHz bandwidth at a carrier frequency of 300 kHz.

The results in this report are obtained using only BPSK-modulated messages with 25 kHz of bandwidth. Multiple messages were recorded from each distance. The proposed multilevel adaptive diversity is performed only on messages with non-zero BER. SNIR and BER of each received message are estimated using a known message with zero BER. Since the number of all possible combinations from different distances using three, four or five receivers is very high and the adaptive diversity for one set of receivers takes long time to process, the messages with highest BER at each distance are processed. BER and SNIR of individual messages used in the combining are given in Table 9.

Table 9: BER and SNIR of individual messages used in the experimental results.

Distance	BER [%]	SNIR [dB]
25	0.0830	12.4284
50	6.7270	10.6280
80	0.1056	16.5451
95	3.1599	11.4762
120	0.1659	17.5701
160	0.0377	15.3332

BER and SNIR for all possible combinations of the received messages using adaptive diversity with three, four and five receivers are given in Figure 49 and Figure 50. The experimental results

for BER and SNIR follow the theoretical results, where increased number of receivers leads to decreased BER and increased SNIR, respectively.

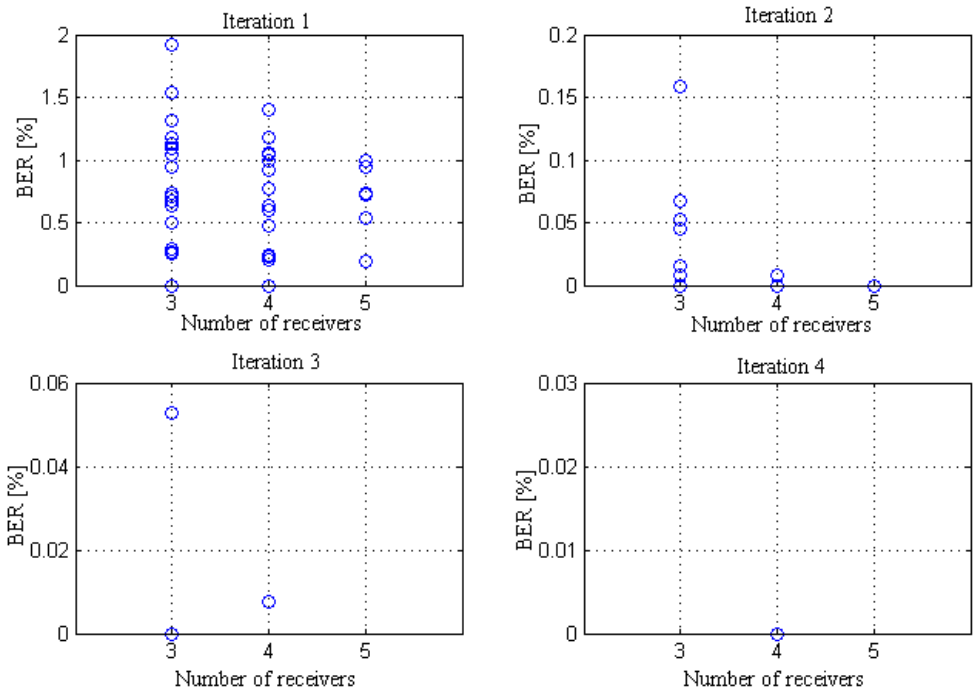

Figure 49: BER achieved with multilevel adaptive diversity for different number of receivers.

The BER of the combined messages (Figure 49) decreases when more iterations of the adaptive process are performed. The system with five receivers achieves zero BER in the second iteration. In case of three and four receivers few combinations need three and four iterations for the best result. The biggest impact of this approach can be seen in the second iteration where the maximum BER decreases with more than one tenth of the maximum value in the first iteration. Individual messages recorded at 50 m and 95 m distance have overly high BER which can lead to a non-retrievable message at the receiver. Using the diversity approach, the impact of the high individual BER on the receiving process is minimized and in all combinations with the exception of one, the BER of the combined message is zero. In addition, adaptive diversity significantly lowers the BER of a heavily corrupted individual message. The BER of an individual message received at 50 m decreases from 6.727% to about 1% using this approach.

The SNIR of the combined messages increases with each iteration, as shown in Figure 50. The result is expected because the MRC criterion was used in the decision process. The SNIR of the combined message has the biggest increase (about 2 dB on average) at first iteration, compared to the highest SNIR of the individual messages. SNIR increases further with each additional iteration with about 0.5 dB per iteration.

The average values for BER and SNIR for all iterations and for all combinations are given in Figure 51. In case of BER, the number of receivers used in the SIMO system does not decrease dramatically the value of BER with each additional receiver, but has an impact on the number of iterations needed to achieve optimal results. The biggest decrease of BER values are seen as a result of the adaptive diversity process. On the other hand, the SNIR values increase when both number of receivers increased and the adaptive diversity is used. There is an exception from the

expected SNIR results in the third and fourth iteration of the process. The SNIR values are expected to increase, but the deviation from the expected result is due to the small number of combinations used to calculate the average values.

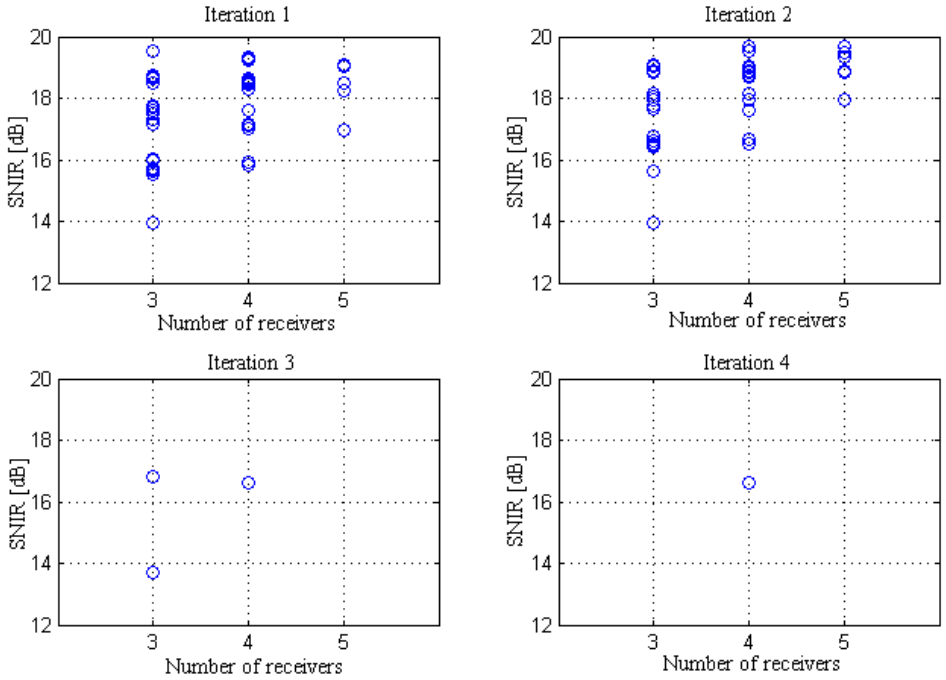

Figure 50: SNIR achieved with multilevel adaptive diversity for different number of receivers.

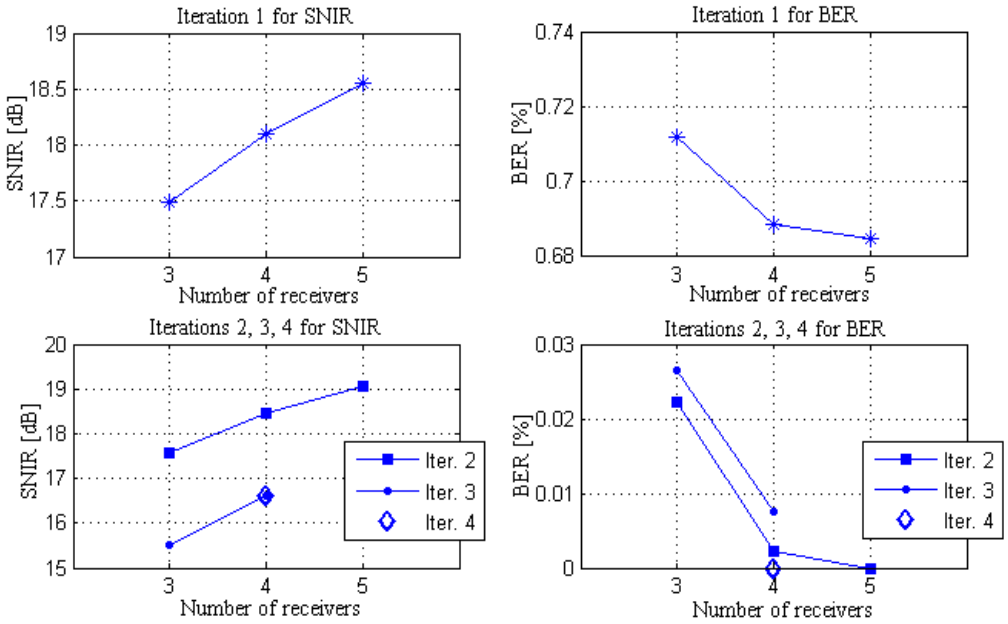

Figure 51: Average values of BER and SNIR for all combinations.

Adaptive diversity process implemented on two levels improves the BER and SNIR of the combined message compared to the individually received messages. Using different number of receivers and multilevel adaptive diversity combining on messages with non-zero BER we were able to achieve BER of 0% and increase in SNIR up to 3 dB depending on the SNIR values of individual messages. Furthermore, we were able to retrieve to a certain point a heavily corrupted message and improve its BER from 6.7270% to as low as 1%. The improved channel characteristics are achieved at the expense of processing time and the cost of additional equipment, without need to increase the transmission power or the channel bandwidth. Adaptive diversity combined with parallel MSDFE achieves better performance of the acoustic channel and increases the reliability and coverage area of the underwater acoustic communications system in the challenging environment. Future work includes the implementation of the proposed multilevel diversity approach on simulated data, which will overcome the limitation of the small sample size of experimental data and provide statistical validation of the proposed approach.

6.4 Multiple input multiple output uplink

The results in terms of MIMO deconvolution are presented in this section. The simulation parameters and the metrics are first presented, followed with a description of the experimental setup. The simulated results are analyzed: in this case, the channel is stationary over the duration of the message. Finally, a set of field data is analyzed, where time variations of the channel are observed.

6.4.1 Experimental Setup

The series of experiments for this project were carried out in the Florida Atlantic University Seatech marina (Figure 52). While the experimental setup presented here uses two sources and three receivers, this report presents only the results obtained with two receivers. Table 10 provides a summary of the data collection. A first set of data was acquired on 07/27/2011. A second series of experiments took place on 08/31/2011. The two sources were alternatively placed at the two locations labeled 'Pos1" and "Pos7" in Figure 52. Two splash proof boxes were built to prevent any damage to the modem sources and were installed on kayaks. Each box contained the Hermes source electronics and a battery pack. The messages were transmitted using Hermes units equipped with ITC-1089 transducers. The source level was 179 dB ref. 1µPa at 1m. The receivers used to carry out these missions were deployed of a small research vessel. The experimental ranges are given in Table 11. The signals presented in this report were acquired at a maximum range of 27 m. At this point, it is important to account for absorption loss, which is a major limiting physical parameter for underwater acoustic propagation: at the frequency range used here (262 kHz – 375 kHz), the absorption in sea water at 20°C is 100 dB/km.

Since the equipment did not have the ability to perform real-time MIMO communication, each source was used individually and the MIMO messages were constructed off-line. The SNR was calculated on each receiver. The average value of SNR_j, where j corresponds to the receiver index, across the total number of messages retained per mission is displayed in Table 12. The results in SNR are consistent for every mission: we observe fluctuations around a mean value of 32 dB. These variations result of the time varying characteristics of the channel, especially since the missions were not all carried out at the same time. Note also that these values of the SNR were obtained after averaging over an important number of messages. We can also explain these differences by the fact that the electronics used in every receiver was not exactly the same.

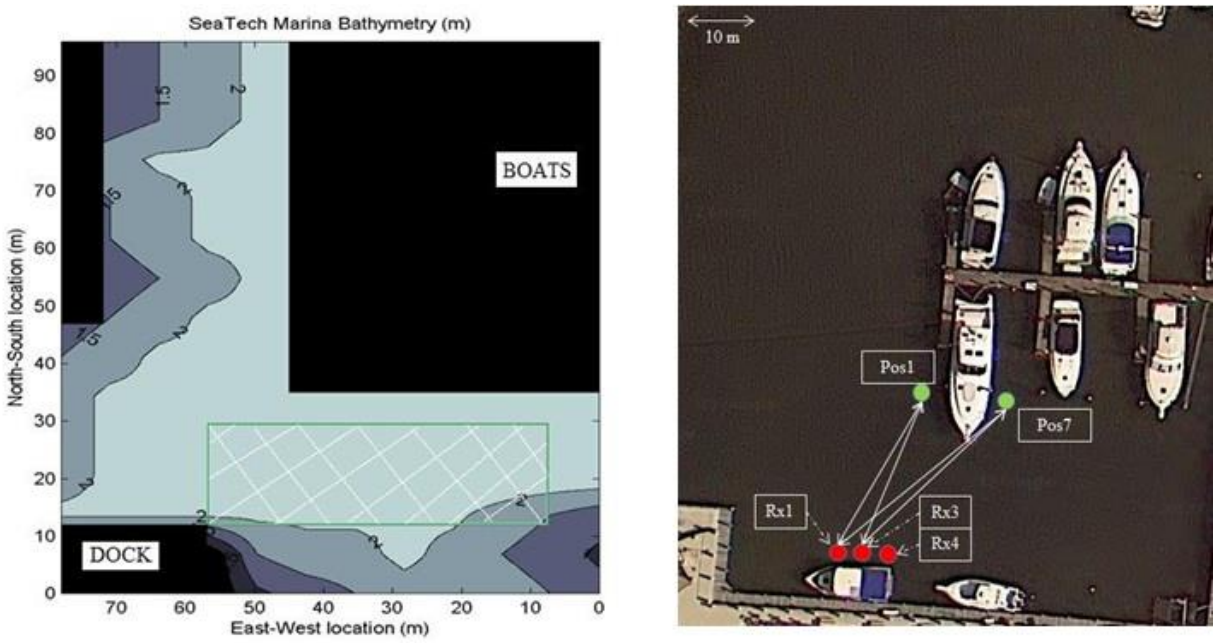

Figure 52: Experimental Setup.

Table 10: Summary of Data Collected.

Mission number and Date	Source 1 Position	Source 2 Position	Receiver 1 Position	Receiver 2 Position	Number of Messages Retained
1-07/27/2011	Pos1	Pos7	Rx1	Rx3	50
2-07/27/2011	Pos7	Pos1	Rx1	Rx3	50
3-08/29/2011	Pos7	Pos1	Rx1	Rx3	100
4-08/29/2011	Pos1	Pos7	Rx1	Rx3	100

Table 11: Experimental Ranges.

Distance	Distance (m)
Rx1-Pos1	24
Rx1-Pos7	27
Rx3-Pos1	23.3
Rx3-Pos7	25.8
Pos1-Pos7	6.15
Rx1-Rx3	2.68

Table 12: Signal-to-Noise Ratio per Mission and per Receiver.

Mission number and Date	$\mathrm{SNR}_1(dB)$	$\mathrm{SNR}_2(dB)$
1-07/27/2011	27.1	27.3
2-07/27/2011	28.8	27.8
3-08/29/2011	30.9	34.3
4-08/29/2011	29.2	33.2

6.4.2 Simulation Parameters

The channel model combines a deterministic model (average echo intensities) and stochastic Rician model. Sources and receivers separation and depth matches the experimental setup. The simulation parameters (Table 13) are tuned to match the experimental data sets as closely as possible. Doppler shift and Doppler spread have been derived from the field data. The time window used to perform the channel estimation covers the duration of the MIMO sequence and the dead-time interval. Hence, the channel is assumed to be time-invariant over the transmission of a message. For every transmitted message, we also adjust the time delay τ_0 between the signals measured at every receiver. In this report, we only consider full overlap between received messages. The channel model considered here includes both the specular reflection from the sea bottom and scattering from the sea surface and bottom.

Table 13: Simulation Parameters.

Name	Symbol	Value (units)	Name	Symbol	Value (units)
Sources Depth	D_{S_i}	1 m	Source Level	SL	179 dB re 1μPa @ 1m
Receivers Depth	D_{R_j}	1.5 m	Noise Level	NL	83.7 dB re 1μPa
Water Depth	D_W	3m	Sampling Frequency	F_s	150 kHz in Base Band - 750 kHz in Pass Band
Water Sound Speed	c	1500 m/s	Symbol Rate	F_{sym}	75 kHz
Water Density	ρ	1023 kg/m^3	Carrier Frequency	F_0	0 kHz in Base Band 300 kHz in Pass Band
Sandy Sediment Sound Speed	c_b	1800 m/s	MIMO Sequence Duration	τ_H	218.5 ms
Sandy Sediment Density	ρ_b	1800 kg/m^3	Dead-Time Duration	τ_{msg}	300 ms
Spreading factor	k_{spread}	15	Number of Transmitted Messages	N_{msg}	100
Sea Bottom Loss	L_{SB}	5 dB	Correlation Threshold Parameter	K_{thr}	20
Beginning of Time Window	k_0	0	Time Window Length	τ_{win}	518.5 ms
Number of Transmitters	N_t	2	Number of Receivers	N_r	2
Distance Source 1 Receiver 1	R_{11}	23.3 m	Distance Source 1 Receiver 2	R_{12}	24 m
Distance Source 2 Receiver 1	R_{21}	25.8 m	Distance Source 2 Receiver 2	R_{22}	27 m

6.4.3 MIMO Channel Estimation Results

Table 14 shows the values of RMSE_{CE} with variations of T_L for both experimental and simulated data. The maximum value of T_L taken into consideration was 5.33 ms. Performing the channel estimation with higher values of T_L leads to singularities and does not allow to obtain accurate results. Therefore, this is the maximum value that can be considered. As a reminder, RMSE_{CE} measures the error between the received signals and the emitted sequences convolved with the estimated channels. Since an averaging over the total number of receivers is performed, the results presented in Table 14 translate the accuracy of the channel estimation for all the estimated sub-channels.

Table 14: RMSE_{CE} as a Function of T_L.

$T_L\,(ms)$	Simulated $\mathrm{RMSE}_{CE}\,(dB)$	Experimental $\mathrm{RMSE}_{CE}\,(dB)$
0.667	-9.5	-0.4
1.333	-12.5	-0.9
2.0	-18.8	-4.1
2.667	-34.7	-4.9
3.333	-34.7	-6.2
4.0	-34.7	-9.1
4.667	-34.8	-11.4
5.33	-34.8	-25.7

In both experimental and simulation cases, as T_L increases, the accuracy of the channel estimation improves. However, while RMSE_{CE} reaches a sweet-spot at $T_L = 2.667$ ms using simulated data ($\mathrm{RMSE}_{CE} \simeq -34.7dB$), the experimental results on RMSE_{CE} differ. Indeed, the minimum RMSE_{CE} is obtained for $T_L = 5.33$ ms ($\mathrm{RMSE}_{CE} = -25.7dB$) as shown in Table 14 and Figure 53. If, as explained earlier on, values higher than $T_L = 5.33$ ms cannot be considered, the minimum value of RMSE_{CE} using experimental data is of the same order of magnitude as RMSE_{CE} in the simulation framework. The channel estimation can therefore be considered as very accurate. Figure 53 displays the influence of T_L on the channel estimation accuracy in the specific case of mission 4. The figure also shows that RMSE_{CE} drops and the confidence interval $[-\sigma_{CE};\sigma_{CE}]$ become narrower as T_L increases.

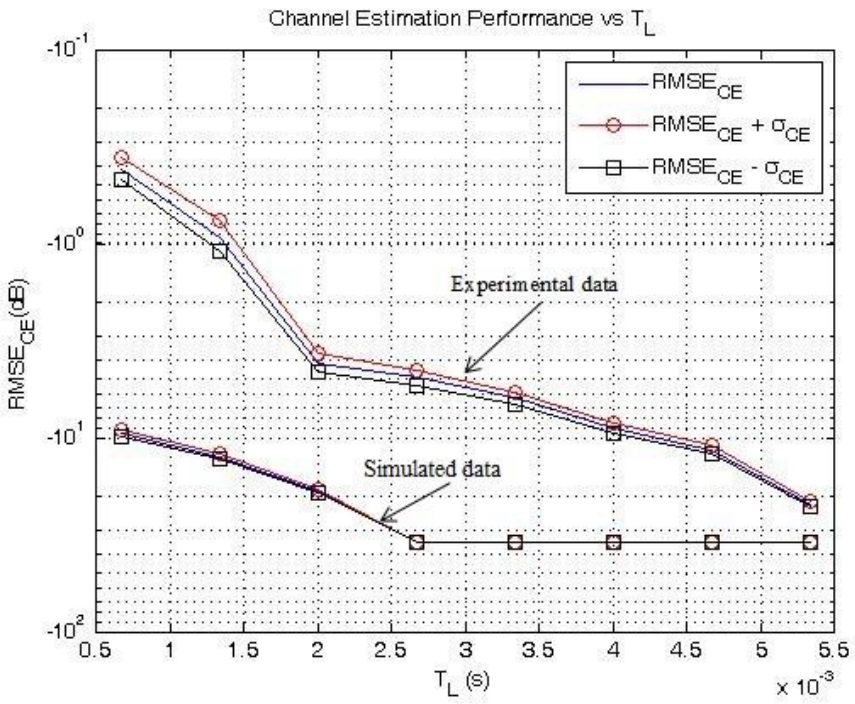

Figure 53: RMSE_{CE} **and** $\mathrm{RMSE}_{CE} \pm \sigma_{CE}$ **as a function of** T_L**.**

Figure 54 shows the values of the RMSE obtained for each of the four missions carried out, for each receiver, and the values of the SNR corresponding to the mission and receiver of interest.

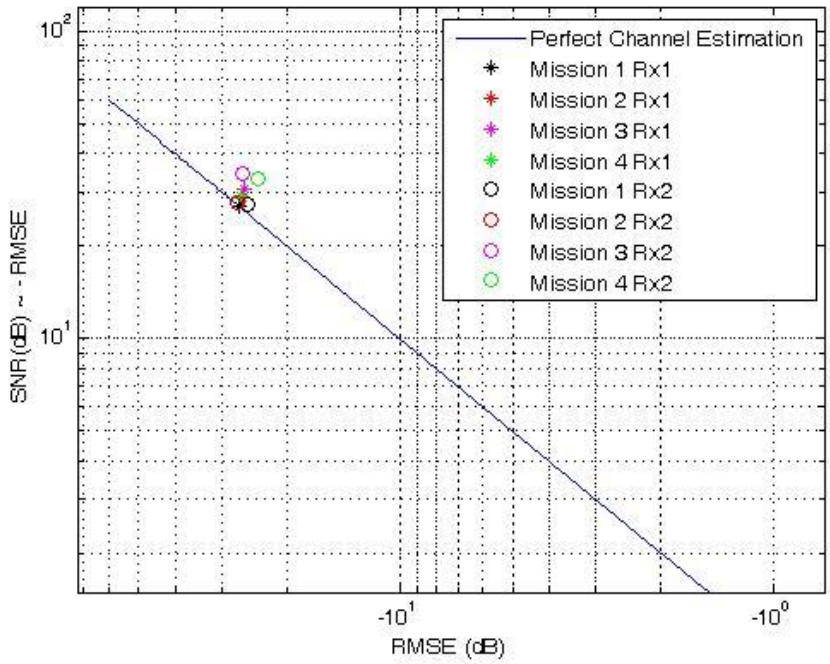

Figure 54: SNR vs RMSE at the output of the channel estimator corresponding to the same mission and receiver.

In Figure 54, we observe an acceptable correspondence between experimental data and perfect channel estimation curve, even though some difference is noticed. As an example, the case of Mission 3, receiver 2 shows a RMSE of -26.4 dB and a corresponding SNR of 34.28 dB. As demonstrated in (39), this phenomenon is explained by the fact that the channel estimator induces some additional noise to the signal, causing the RMSE to be higher than expected.

6.4.4 MIMO Deconvolution Results

A comparison of the MIMO deconvolution capability between experimental data and simulation results has been completed, using the RMSE defined in (34), (35) and (36). The results are shown in Table 15 and 16. The effects of variations of the parameter T_L is observed. The results are shown for $T_\kappa = T_{\kappa_{\max}} = 6\ \text{ms}$, which lead to the lowest RMSE value. Both simulations and experimental results (averaged over the total number of missions carried out) are presented in Table 16. Clearly, RMSE_{MIMO_LE} and RMSE_{MIMO_ICLE} decrease as T_L increases using either simulated or field data. Note that the equalizer length is limited to $T_L = 5.33\ \text{ms}$, as higher values of T_L led to singularities.

Table 15: RMSE between Emitted and (Raw) Received Signals, RMSE_{MIMO_Raw}, as a Function of T_L.

$T_L\,(ms)$	$\text{RMSE}_{MIMO\_Raw}\,(dB)$	
	Simulations	Experiments
0.667 ms, 1.333 ms, 2 ms, 2.667 ms, 3.333 ms, 4 ms, 4.667 ms, 5.33 ms	0.04	3

Table 16: RMSE between Emitted and Received Signals after LE Processing, RMSE_{MIMO_LE} and after ICLE Processing, RMSE_{MIMO_ICLE} as Functions of T_L.

		$\text{RMSE}_{MIMO\_LE}\,(dB)$		$\text{RMSE}_{MIMO\_ICLE}\,(dB)$	
		Simulations	Experiments	Simulations	Experiments
$T_L\,(ms)$	0.667	**0.4**	**19.7**	**-4.5**	**15.8**
	1.333	**-3.4**	**14.4**	**-6.7**	**12.1**
	2.0	**-10.3**	**8.3**	**-13**	**6.4**
	2.667	**-20.5**	**5.5**	**-33.4**	**3.1**
	3.333	**-20.5**	**2.2**	**-33.4**	**0.7**
	4.0	**-20.5**	**-1.9**	**-33.3**	**-3**
	4.667	**-20.5**	**-3.9**	**-33.3**	**-8.8**
	5.33	**-20.5**	**-3.3**	**-33.2**	**-26.9**

RMSE_{MIMO_LE}, computed with both simulated and experimental data, is shown in Figure 55. This figure shows the influence of the pre-cursor and post-cursor length: if T_L is sufficiently large

to provide accurate channel estimation, RMSE_{MIMO_LE} drops as T_κ increasing. Therefore, showing the influence of T_L on RMSE_{MIMO_LE} is not of great interest: this is why we chose to represent RMSE_{MIMO_LE} as a function of T_κ only ($T_L = 5.33\ \mathrm{ms}$). For example, for an equalizer length $T_L = 5.33\ \mathrm{ms}$, $\mathrm{RMSE}_{MIMO\_LE} = -6.2\ \mathrm{dB}$ with $T_\kappa = 0.7\ \mathrm{ms}$ and drops to $\mathrm{RMSE}_{MIMO\_LE} = -20.5\ \mathrm{dB}$ with $T_\kappa = 6.0\ \mathrm{ms}$. As it has been shown in the channel estimation process results, the confidence interval also narrows as the process gets more and more reliable.

In the case of experimental data, severe distortions in the received signals impact the accuracy of the MIMO deconvolution process. Indeed, RMSE_{MIMO_LE} varies dramatically when computed with simulation and experimental data. In the best case scenario, we use $T_L = 5.33\ \mathrm{ms}$ and $T_\kappa = 6\ \mathrm{ms}$. Figure 56 shows the variation of $\mathrm{RMSE}_{MIMO\_ICLE}$ as a function of T_L: if the MIMO sequence is known, the accuracy of the process improves as T_L increases. On average, $\mathrm{RMSE}_{MIMO\_ICLE} = -26.9dB$ when $T_L = 5.33\ \mathrm{ms}$ using experimental data vs. -33.2dB using simulated data. As expected, the comparisons between $\mathrm{RMSE}_{MIMO\_ICLE}$ and RMSE_{MIMO_LE} calculated using simulated and experimental data reveals that LE process does not reach the lower bound provided by ICLE structure. Using simulation data, we find that $\mathrm{RMSE}_{MIMO\_ICLE} = -33.2\ \mathrm{dB}$ while $\mathrm{RMSE}_{MIMO\_LE} = -20.5\ \mathrm{dB}$. This phenomenon is especially pronounced in the case of experimental data, where $\mathrm{RMSE}_{MIMO\_ICLE} = -26.9\ \mathrm{dB}$ and $\mathrm{RMSE}_{MIMO\_LE} = -3.3\ \mathrm{dB}$ for $T_L = 5.33\ \mathrm{ms}$. One can conclude that LE alone is not totally sufficient to remove the whole interference terms provided by frequency selective channel and multi-antenna architecture. Non-linear approaches like iterative processing strategy or decision feedback equalization appear thus necessary.

The capability of Hermes to support MIMO technology was presented in this report. The system performance was evaluated using both simulated and experimental data, using two sources and two receivers. The ability to retrieve, using a Linear Equalizer (LE), emitted messages in presence of inter-symbol interferences, co-antenna interferences and noise was estimated.

The channel impulse response estimation performance was related to the value of the channel estimate length T_L. Computer simulations showed that for $T_L \geq 2.667\ \mathrm{ms}$, the relative root mean-square error used to measure the accuracy of the estimation reached a plateau. In this configuration, an RMSE comparing the received header and the ability of the system to rebuild this received header using the estimated channels of -34.8dB was measured across the total number of transmitted messages. This performance was compared to experimental data: we observed in this case a value for the same metric of -25.7dB for $T_L = 5.33\ \mathrm{ms}$, meaning that the proposed technique evaluates fairly accurately the acoustic channel between every source and receiver.

To measure the benefits of this linear equalizer, the RMSE between emitted and received messages was first computed for each individual source and receiver. An Interference Cancelation Linear Equalizer (ICLE) was also developed to measure the limit of the deconvolution process, using estimated channel impulse responses. Optimized under the MMSE criterion, the ICLE took advantage of the known source signal. Using simulated data, $T_L = 5.33\ \mathrm{ms}$ and $T_\kappa = 6\ \mathrm{ms}$, the

RMSE was estimated at 0.03 dB before equalization, -20.5 dB after LE and -33.3 dB after ICLE. For experimental data (with the same values for T_L and T_κ), the RMSE was estimated at -3 dB before equalization, -3.3 dB after LE and to -26.9 dB after ICLE.

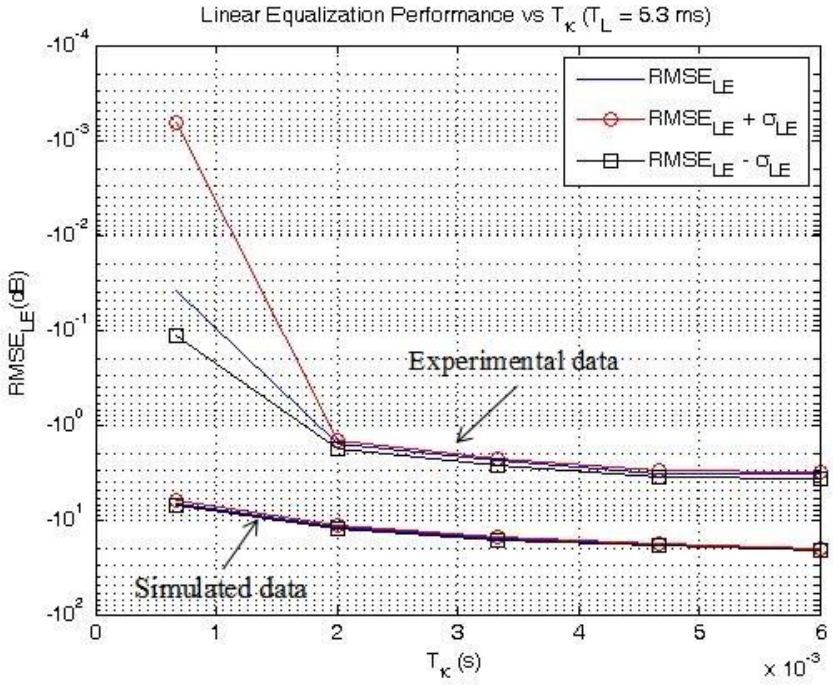

Figure 55: RMSE_{MIMO_LE} **as a Function of** T_L **and.** T_κ **using Simulated Data.**

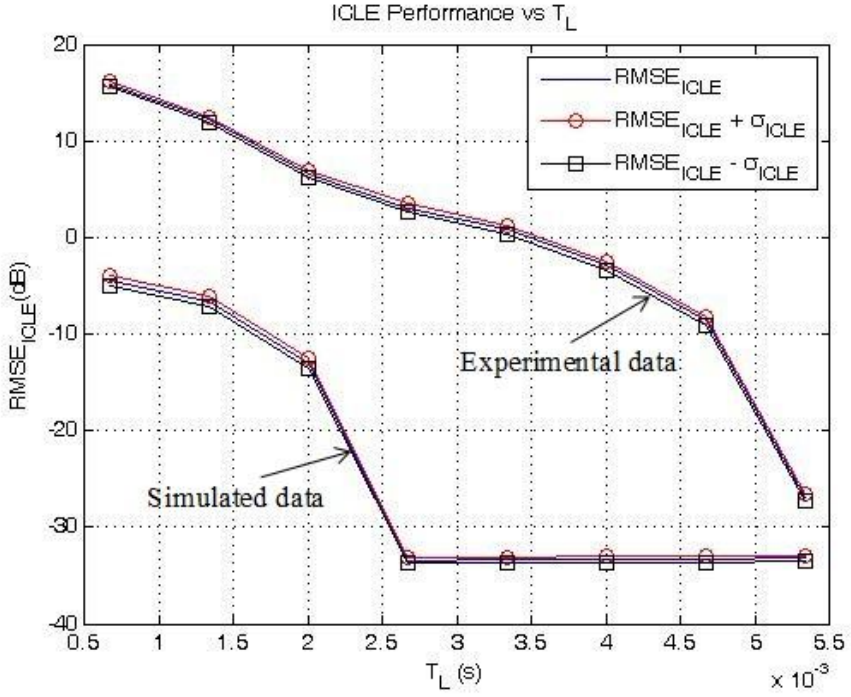

Figure 56: $\mathrm{RMSE}_{MIMO\_ICLE}$ **and** $\mathrm{RMSE}_{MIMO\_ICLE} \pm \sigma_{ICLE}$ **as a Function of** T_L**.**

To conclude with the results presented in this section, the channel estimator and ICLE processes produce fairly similar results in simulation and experimentations. The fact that the performance of the channel estimation process and the ICLE are very comparable indicates that the deconvolution process is very accurate: in this case, the residual errors are not due to the ICLE itself. The LE performs better with simulated data but still brings some benefits to the communication system in the case of field data. The encouraging results indicate that the FAU Hermes underwater acoustic modem could be successfully equipped with MIMO technology.

6.4.5 High-Resolution MIMO Channel Estimation Results using EMD trending

The EMD-based channel impulse response estimation method was first tested using a simulated two path channel. The channel impulse response estimation routine parameters for the simulated data are given in Table 17. The channel paths are separated by 5 samples (or 0.07 ms) and have a respective gain of 1 and 0.5 to match experimental findings. The first path, corresponding to $l = 0$, is labeled $h(t_0)$ while the second path, corresponding to $l = 5$, is labeled $h(t_5)$. Each path is associated with a different Doppler spread to demonstrate that the estimation technique can handle different paths with different Doppler spreads simultaneously. The Doppler spread on the first path is $f_{D0} = 10$ Hz and on the second path is $f_{D5} = 15$ Hz.

Table 17: Simulation parameters.

Parameter	Value
Doppler spread	10 [Hz]
Window length	401 [sample]
Overlap	1 [sample]
Channel gains	[1 0 0 0 0 0.5]
Signal-to-Noise ratio	32 [dB]

The simulated, estimated and the trend of the estimated real and imaginary parts for each path are shown in Figures 57 and 58 as a function of time. Clearly, the least-square channel impulse response estimation routine tracks the time-varying impulse response closely. Applying the trend extraction leads to a substantial improvement. The same observation is made for the PSD plot. The relative RMSE between estimated and theoretical impulse response is summarized in Tables 18 and 19.

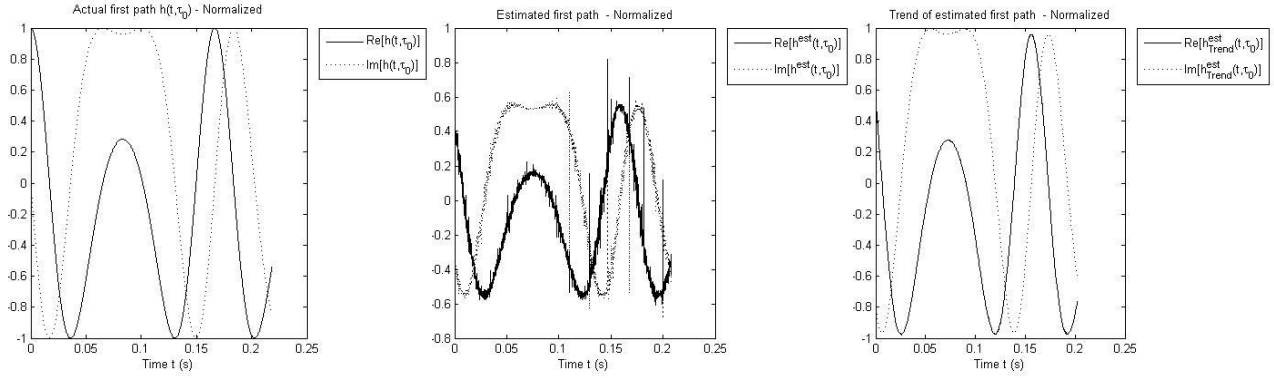

Figure 57: Simulated (left), LS-estimated (center) and EMD-trended (right) Time-Varying Response of the First Echo.

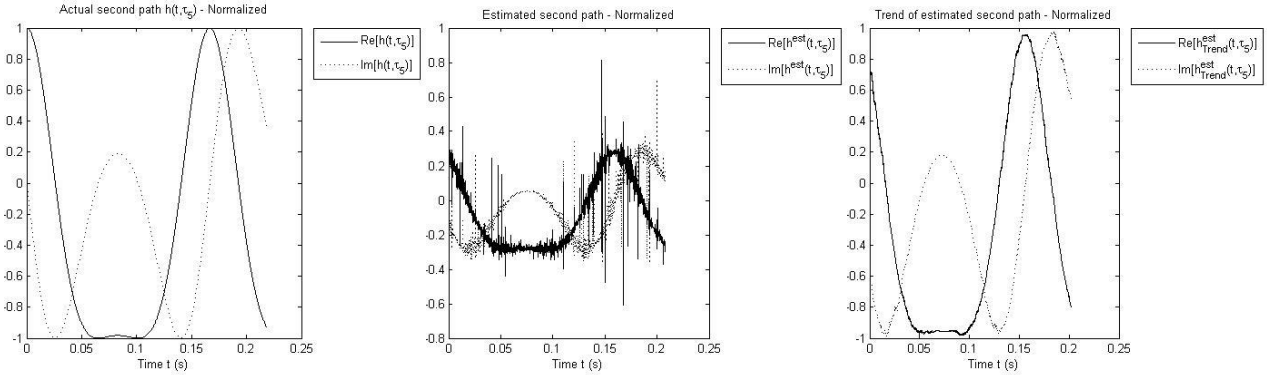

Figure 58: Simulated (left), LS-estimated (center) and EMD-trended (right) Time-Varying Response of the Second Echo.

This technique was applied to the same data set presented in the previous section. Once again, the time-varying response of the two primary echoes was studied. The results are shown in Figures 59 and 60.

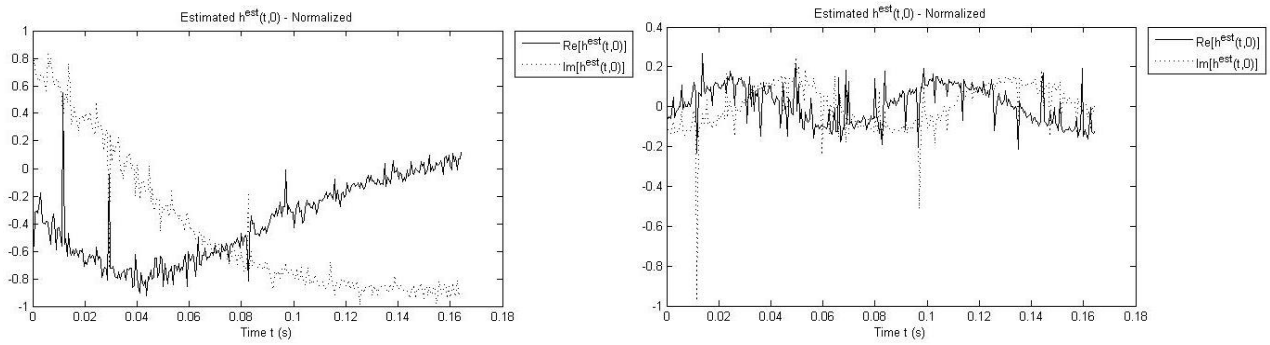

Figure 59: Measured (left), LS-estimated (center) and EMD-trended (right) Time-Varying Response of the First Echo.

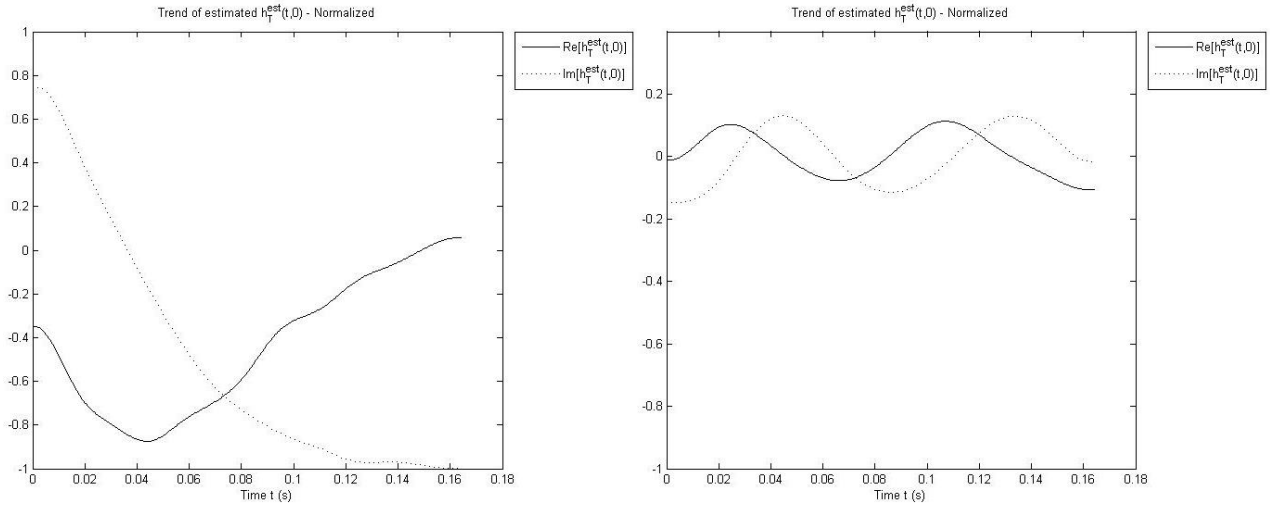

Figure 60: Simulated (left), LS-estimated (center) and EMD-trended (right) Time-Varying Response of the Second Echo.

Table 18: RMSE for the first path.

Parameter	RMSE
Estimation Error with LS method	7.8%
Estimation Error with combined LS and trend method	2.9%

Table 19: RMSE for the second path.

Parameter	RMSE
Estimation Error with LS method	15.7%
Estimation Error with combined LS and trend method	4.7%

The experimental data clearly show that the routine can closely track the time variations of the main echo and provide a meaningful estimate of the Doppler spread. These results also indicate that the combined use of the traditional LS approach with an extraction of the trend to estimate the channel impulse response leads to better results.

7. Publications

- V. Skoro Kaskarovska, P.-P. Beaujean, "Combination of spatial diversity and parallel decision feedback equalizer in a Single Input Multiple Output underwater acoustic communication system operating at very high frequencies", Proceedings SPIE, Vol. 8753, Wireless Sensing, Localization, and Processing VIII, pp. 1-10, May 2013 [published].
- S. Kaddouri, P.-P. Beaujean, P.-J. Bouvet, "Doppler Estimation in Fading Channel for High-Frequency Underwater Acoustic Communications", Proc. of the IEEE Underwater Communications: Channel Modelling & Validation, Sestri Levante, Italy, pp.1-7, Sept. 2012 [published].
- G. Real, P.-P. Beaujean, P.-J. Bouvet, "MIMO Underwater Acoustic Communications in Ports and Shallow Waters at Very High Frequency", Proc. of the IEEE Underwater Communications: Channel Modelling & Validation, Sestri Levante, Italy, pp.1-9, Sept. 2012 [published].
- P. Kathiroli, P.P. Beaujean, N. Xiros, "Source Speed Estimation using a Pilot tone in a High Frequency Acoustic Modem", Proc. of the MTS/IEEE Oceans'2011, Kona, Hawaii, pp. 1-8 [published].
- G. Real, P.P. Beaujean, P.J. Bouvet, "A Channel Model and Estimation Technique for MIMO Underwater Acoustic Communications in Ports and Very Shallow Waters at Very High Frequencies", Proc. of the MTS/IEEE Oceans'2011, Kona, Hawaii, pp. 1-9 [published].
- P.P. Beaujean, E. Carlson, "Combined Vehicle Control, Status Check and High-Resolution Acoustic Images Retrieval using a High-Frequency Acoustic Modem on a Hovering AUV", Proc. of the MTS/IEEE Oceans'2010, Seattle, Washington, September 2010, pp. 1-10 [published].
- P.P. Beaujean, "Multiple-Input Multiple-Output Capability Assessment using a High-Bit-Rate Underwater Acoustic Modem (Hermes)", Unmanned Maritime Systems Technology (UMST) Review 2013, Panama City, Florida, Jan. 2013 [published].
- P.P. Beaujean, "High-Data Rate Acoustic Communications for Transmission of ATR Images, Mosaics, 3-D Images and Vehicle Status in Complex and Non-Complex Search Areas", Unmanned Maritime Systems Technology (UMST) Review 2012, Panama City, Florida, Jan. 2012 [published].
- P.P. Beaujean, "High-Data Rate Acoustic Communications for Transmission of ATR Images, Mosaics, 3-D Images and Vehicle Status in Complex and Non-Complex Search Areas", Unmanned Maritime Systems Technology (UMST) Review 2011, Panama City, Florida, Jan. 2011 [published].

- P.P. Beaujean, "Broadband, High-Frequency Acoustic Communications for Sonar Data Transmission from UUV's in Ports and Shallow Waters", Unmanned Maritime Systems Technology (UMST) Review 2010, Panama City, Florida, Jan. 2010 [published].
- P.P. Beaujean, "Broadband, High-Frequency Acoustic Communications for Sonar Data Transmission from Unmanned Underwater Vehicles's in Ports and Shallow Waters", Unmanned Maritime Systems Technology (UMST) Review 2010, Panama City, Florida, Jan. 2010 [published].
- P.P.J. Beaujean, E.A. Carlson, J. Spruance, "High Bit-Rate Underwater Acoustic Communications in Difficult Environments", Sea Technology, pp. 17-21, May 2009 [published].
- P.-P. Beaujean and E. Carlson, "HERMES – A High Bit-Rate Underwater Acoustic Modem Operating at High-Frequencies for Ports and Shallow Water Applications", Marine Technology Society Journal, Vol. 43, no. 2, 2009, pp. 21-32 [published].
- P.-P. Beaujean, M. Pajovic, E. Carlson, J. Spruance, "Frequency-Hopped Frequency Division Multiplexed Signaling for Underwater Acoustic Communications between 60 and 90 kHz in Ports and Very Shallow Waters", Proc. of the MTS/IEEE Oceans'2009, Biloxi, Mississippi [published].
- M. Pajovic, P.-P. Beaujean, "Turbo-Coded Frequency-Hopped Frequency Division Multiplexed Signaling For Underwater Acoustic Communications between 60 and 90 kHz in Ports and Very Shallow Waters", Proc. of the MTS/IEEE Oceans'2009, Biloxi, Mississippi [published].
- M. Pajovic, "Turbo-Coded Frequency Division Multiplexing for Underwater Acoustic Communications between 60 Khz and 90 Khz", Master's Thesis, Florida Atlantic University, August 2009 [published].
- P.-P. J. Beaujean and E. Carlson, "HERMES – A High Bit-Rate Underwater Acoustic Modem Operating at High-Frequencies for Ports and Shallow Water Applications", Marine Technology Society Journal, Vol. 43, no. 2, 2009, pp. 21-32 [published].
- P.P.J. Beaujean, E.A. Carlson, J. Spruance, "High Bit-Rate Underwater Acoustic Communications in Difficult Environments", Sea Technology, pp. 17-21, May 2009 [published].
- P.P.J. Beaujean, "A Performance Study of the High-Speed, High-Frequency Acoustic Uplink of the HERMES Underwater Acoustic Modem", *Proceedings of OES/IEEE Oceans'09 Europe*, May 2009, Bremen, Germany [published].
- P.P. Beaujean, "Broadband, High-Frequency Acoustic Communications for Sonar Data Transmission from UUV's in Ports and Shallow Waters", AUVSI's Unmanned Maritime Systems Technology (UMST) Review 2009, Orlando, Florida, Jan. 2009 [published].
- P.P. Beaujean, "High-Speed Underwater Communications using Broadband, High-Frequency Acoustics", AUVSI's Unmanned Maritime Systems Technology (UMST) Review 2009, Orlando, Florida, Jan. 2009 [published].
- P.P.J. Beaujean, E.A. Carlson, J. Spruance and D. Kriel, "HERMES – A High-Speed Acoustic Modem for Real-Time Transmission of Uncompressed Image and Status Transmission in Port Environment and Very Shallow Water", Proceedings of MTS/IEEE Oceans'08, September 2008, Québec, CA. [published].
- P.P.J. Beaujean, "Real-Time Image and Status Transmission from a Hull-Inspection UUV using a High-Speed High-Frequency Acoustic Modem in a Port Environment", Proceedings of the 8th International Symposium on Technology and the Mine Problem, May 2008, Naval Post-Graduate School, Monterey, CA. [published].
- D. Kriel, P.P. Beaujean, "Hermes, a Broadband Acoustic Communications System for Shallow Water Applications", AUVSI's Unmanned Maritime Systems Technology (UMST) Review 2008, Orlando, Florida, Feb. 2008 [published].
- P.M. Blue, "High-speed High-Frequency Acoustic Communications in Ports and Very Shallow Water", Master's thesis, Florida Atlantic University, December 2007 [published].

- P.P.J. Beaujean, "Real-Time Image and Status Transmission from a UUV during a Ship Hull Inspection in a Port Environment using a High-Speed High-Frequency Acoustic Modem", Proceedings of MTS/IEEE Oceans'07, October 2007, Vancouver, CA. [published].
- P.P.J. Beaujean, "High-Speed High-Frequency Acoustic Modem for Image Transmission in Very Shallow Waters", Proceedings of OES/IEEE Oceans'07 Europe, June 2007, Aberdeen, UK. [published].
- P.P. Beaujean, "Imaging Sonar Data Transmission from UUVs using the High-Speed High-Frequency Acoustic Modem", ONR Joint Review of Unmanned Systems Technology Development, Panama City, Florida, Jan. 2007. [published].
- P.P.J. Beaujean, P.M. Blue and D. Kriel, "A High-Speed High-Frequency Acoustic Modem (HS-HFAM) for Ports and Shallow Water Operation", 13th International Congress on Sound and Vibrations, Vienna, Austria, July 2006. [published].
- P.P. Beaujean, T. Nguyen, "High-Speed High-Frequency Acoustic Modem coupled with a Wavelet-Based Embedded Compression", ONR Joint Review of Unmanned Systems Technology Development, Panama City, Florida, Feb. 2006. [published].
- P.P. Beaujean, "High Data Rate, Short Range Communications", ONR Joint Review of Unmanned Systems Technology Development, Panama City, Florida, Feb. 2005. [published].

8. Appendix A - Topside Acoustic Modem Hardware

The topside acoustic modem component consists of a notebook computer, a rugged self-contained portable topside unit, and two topside transducers: one to project the downlink transmissions and the other to receive the uplink transmissions.

8.1 Notebook computer

The notebook computer's built-in LCD display, keyboard, mouse and ports provide the operator's visual display and command/control interfaces. Default Microsoft Windows device drivers are leveraged to interface the notebook hardware to the modem software.

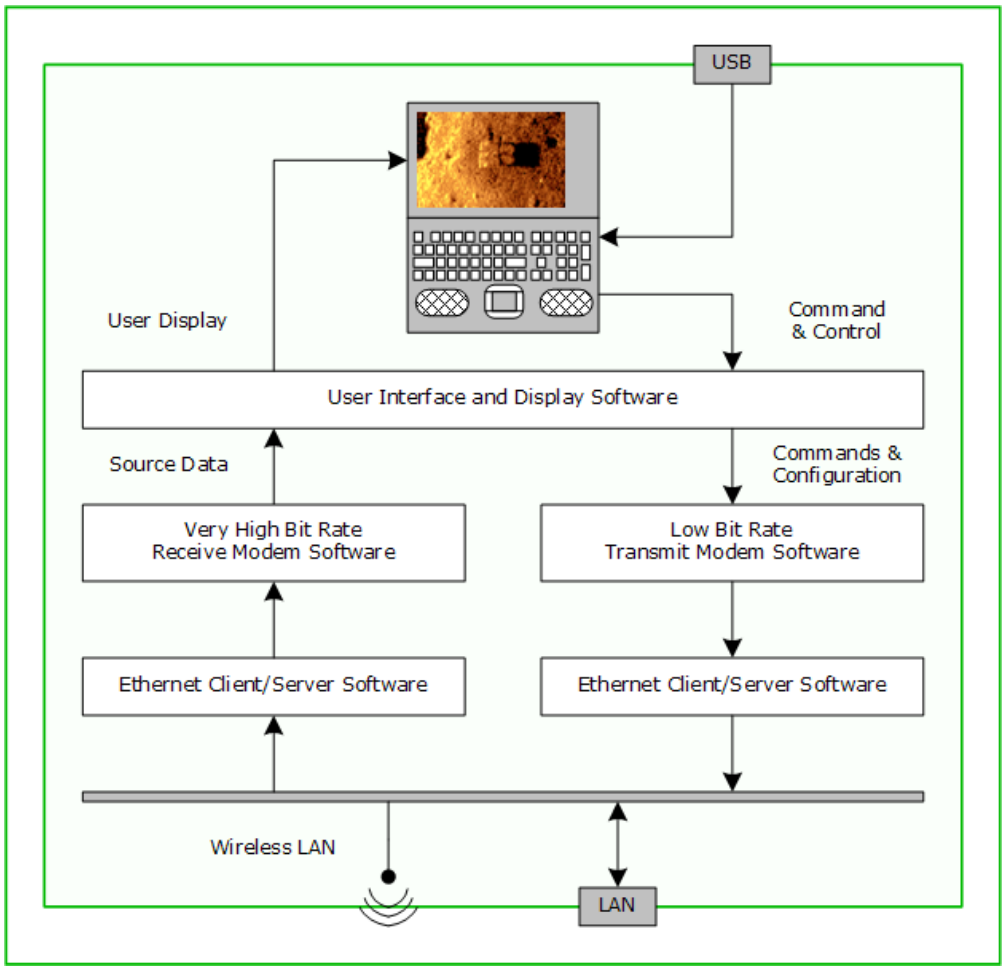

Figure 61: Notebook computer block diagram.

8.2 Portable topside unit

The portable topside unit is a rugged self-contained unit containing the hardware and software to establish a connection between the notebook computer and the topside transducers. It contains the analog interfaces and transmit/receive functions to implement the topside modem acoustic communication channels.

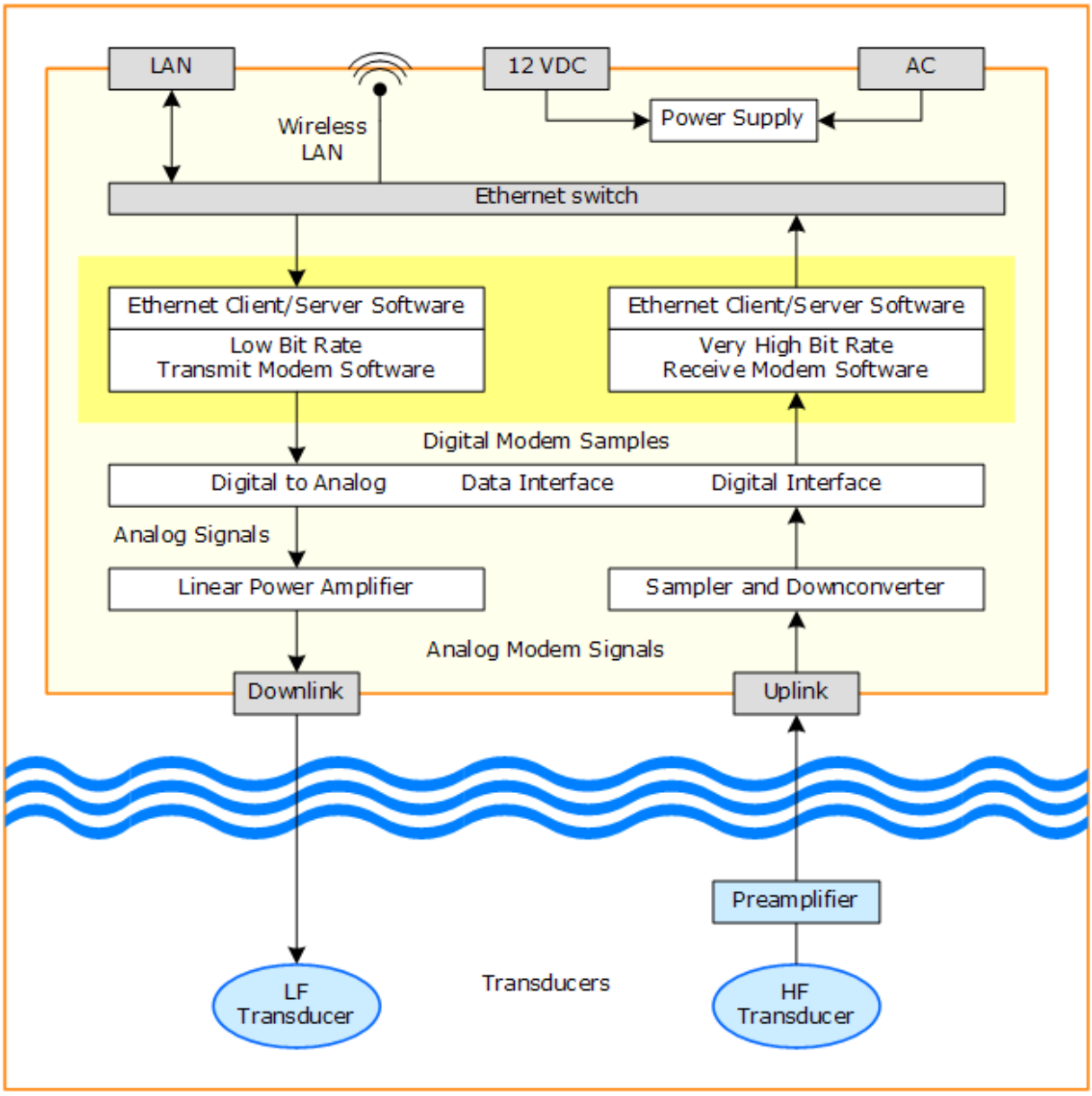

Figure 62: Portable topside unit block diagram.

The portable topside is contained in a Hardigg Storm Case™, customized by EdgeTech. This housing provides a waterproof enclosure for the topside electronics hardware and software components, and is fitted with custom bezels, trimmings, connectors, mounting plates and brackets.

Physical Dimensions
Dimensions .. 390 D x 490 W x 190 H (mm) / 15.2 D x 19.2 W x 7.3 H (inches)
Weight .. 11.6 kg (25.5 lbs)
Construction .. High-impact structural polypropylene
Sealing .. Watertight cover O-ring seal with purge valve

Environment
Operating temperature .. 0°C to 40°C (32°F to 104°F) (shade conditions)
Storage temperature .. -20°C to 60°C (-4°F to 140°F)
Relative humidity .. Operating 0 to 80% (non-condensing); Non-operating 0 to 100%

Power requirements
DC input .. 12 to 15 Vdc .. Peak startup: 12V/25A, Average operating: 12V/4A
AC input .. 120/240 Vac (Auto) .. Peak startup: 12V/2.5A, Average operating: 12V/0.4A

Ethernet interfaces
Ethernet LAN .. 10/100BaseT
Wireless Ethernet .. 802.11 b/g

8.2.1 Portable topside electronics

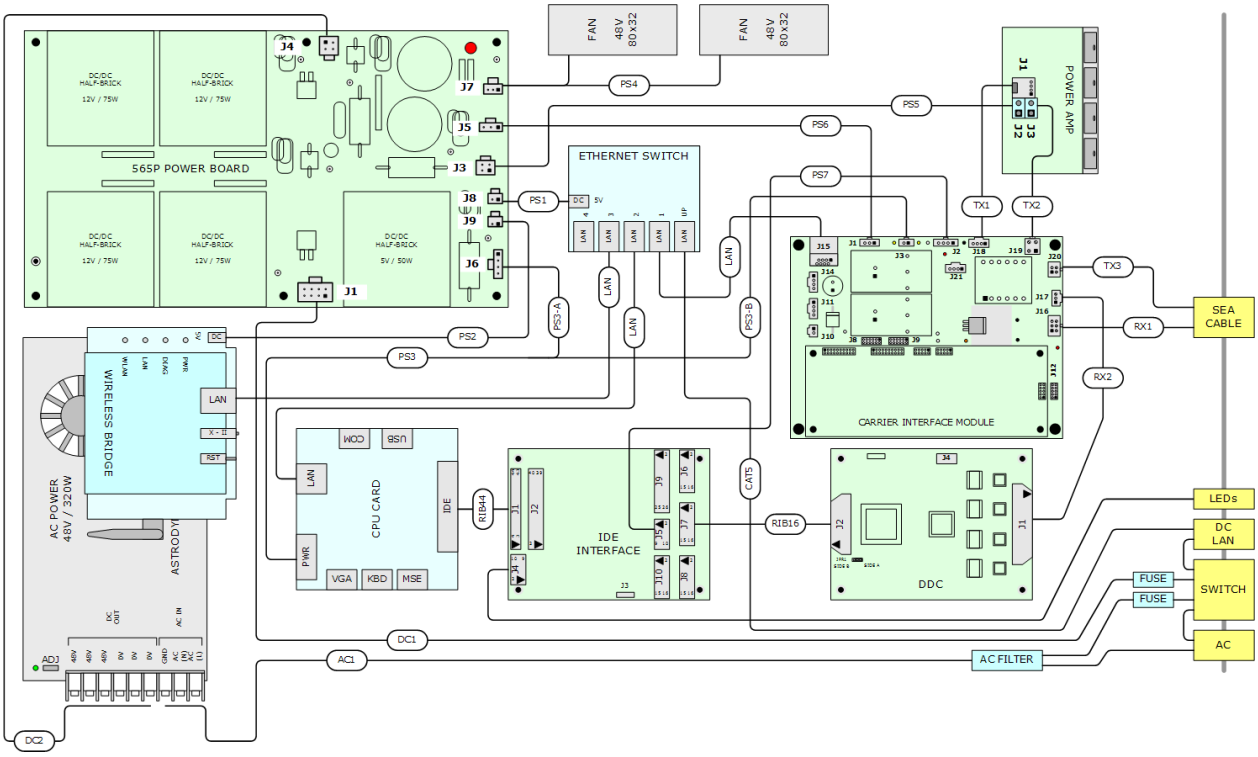

Figure 63: Portable topside electronics block diagram.

Preamplifier module

An external preamplifier, developed by FAU, encapsulated in a waterproof housing that connects inline with the transducer cable. This preamplifier greatly improves the receiver signal-to-noise (S/N) ratio.

Dimensions .. 1.25 x 0.5 x 0.5 inches
Power supply .. 5V/50mA (filtered analog supply via hydrophone cable)

565P power supply module

A standard EdgeTech portable power supply module to provide power to the power amp and portable topside electronics.

Dimensions .. 10.5 x 6.0 x 2 inches
Power inputs
DC input .. 12 to 15 Vdc .. Peak startup: 12V/25A, Average operating: 12V/4A
AC input .. 120/240 Vac (Auto) .. Peak startup: 12V/2.5A, Average operating: 12V/0.4A
Power outputs
Power amp .. 48V @ 75W
Electronics .. 5V @ 50W

CPU card

An Advantech model PCM-3370 PC/104+ module, with 933 MHz LV Pentium III processor with 512MB SDRAM. Operating system: Windows XP Embedded executing from a write protected partition on a 512MB fixed disk CompactFLASH card.

Dimensions .. 96 x 115 mm
Power supply .. 5V/5A (max.)
.. 12V/500mA (max.)

Ethernet switch

An off-the-shelf 5-port 10/100 Mbps auto-sensing N-way switch.

Dimensions .. 82 x 66 x 20 mm
Power supply .. 5V/300mA

Note: Newer models of the wireless Ethernet bridge include a 5-port Ethernet switch, which eliminates the need for this standalone Ethernet switch.

Wireless Ethernet bridge

An off-the-shelf module, typically supplied by Linksys, and used as a standard component in most of EdgeTech's portable topside units.

Dimensions .. 126 x 107 x 27 mm
Power supply .. 5V/2A

Note: Newer models of the wireless Ethernet bridge include a 5-port Ethernet switch, which eliminates the need for the standalone Ethernet switch.

Linear Power Amplifier module

A standard EdgeTech linear power amplifier module.

Dimensions .. 3.6 x 2.4 x 1.4 inches
Power supply .. 48V/1A
Bandwidth .. 50kHz to 500kHz (-3dB)

Carrier and Interface module

A custom motherboard module, developed by EdgeTech, to provide interfaces and power distribution for the modem hardware.

Dimensions .. 6.75 x 5.0 x 1.25 inches
Power inputs .. 5V, 48V (from 565P power supply)
Power outputs
Data Interface .. Digital 5V/1A
Preamplifier .. Analog 5V/100mA
CPU card .. 12V/500mA

Data Interface module

Part of a standard EdgeTech/FAU board set that provides a functional building block for EdgeTech's analog interface and data acquisition requirements. The Data Interface module is implemented by the IDE Interface module of the board set. This module provides an IDE interface to the portable topside processor to receive digital modem samples from the DDC module, and to send digital modem samples via a transmit buffer to a digital-to-analog converter. This board requires some drop-in component modifications to match the acoustic modem gain and frequency requirements.

Dimensions .. 5 x 3.75 x 1 inches
Power supply .. 5V/1A

Sampler & Downconverter module

Part of a standard EdgeTech/FAU board set that provides a functional building block for EdgeTech's analog interface and data acquisition requirements. The Sampler & Downconverter module is implemented by the Direct Digital Downconverter (DDC) module of the board set. This module samples and downconverts the received analog modem signals. This board requires some drop-in component modifications to match the acoustic modem gain and frequency requirements.

Dimensions .. 5 x 3.75 x 1 inches
Power supply .. powered from the Data Interface module

9. Appendix B - Topside software architecture

The topside software consists of the User Interface and Display software, the Very High Bit Rate Receive Modem software, the Low Bit Rate Transmit Modem software, and the topside components of the Modem Driver software.

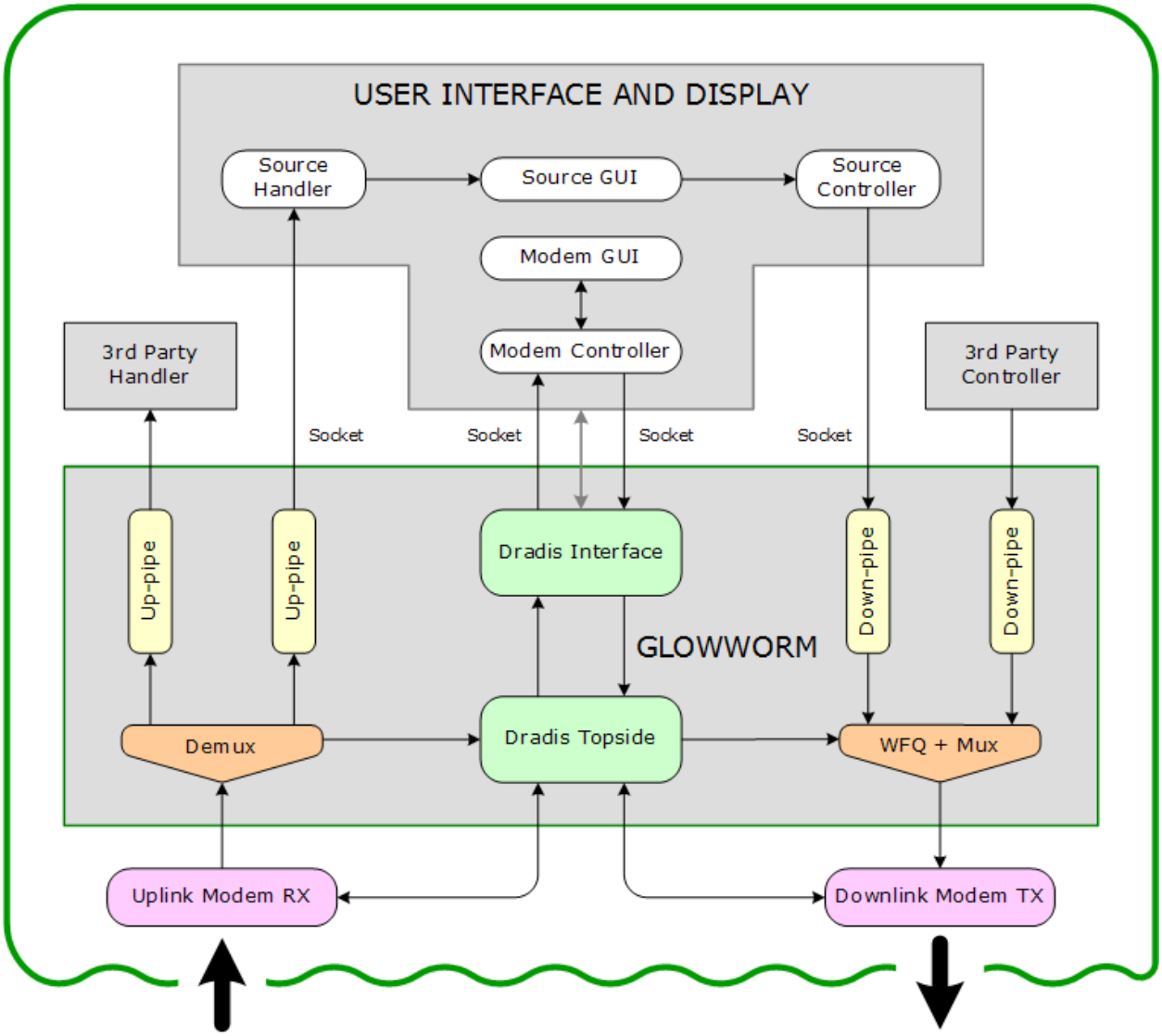

Figure 64: Topside software architecture.

User Interface and Display software

The User Interface and Display software runs under Microsoft Windows XP on a notebook computer and implements a graphical user interface (GUI) that allows the user to configure, control and monitor the entire acoustic communications system.

Very High Bit Rate Receive Modem software

The Very High Bit Rate Receive Modem software runs as multiple sequential processes on one or more Ethernet connected Windows XP platforms, such as the notebook computer and the portable topside. This software detects and synchronizes incoming modem messages, demodulates and decodes them into modem data, and demultiplexes the modem data into multiple source data streams. It then distributes the source data streams to topside destinations such as the User Interface and Display software.

Low Bit Rate Transmit Modem software

The Low Bit Rate Transmit Modem software runs as multiple sequential processes on one or more Ethernet connected Windows XP platforms, such as the notebook computer and the portable topside. This software multiplexes user commands and configuration data from multiple topside inputs, and encodes and modulates the data into modem messages. It then outputs the modem messages to the Data Interface module for analog conversion and transmission.

Modem Driver Software

The topside Modem Driver software consists of the topside portion of the Modem Control software (Dradis) and the Topside Modem Driver software (Glowworm). Dradis forms the underlying control software of the acoustic communications software. Dradis commands are the only way to control the acoustic link. Glowworm provides the topside interface to Dradis. The User Interface and Display software sends Dradis commands to Glowworm to control the acoustic communications link.

10. Appendix C - Wetside Acoustic Modem Hardware

The wetside acoustic modem consists of a submersible wetside unit and two wetside transducers: one to project the uplink transmissions and the other to receive the downlink transmissions.

10.1.1 Wetside electronics

The wetside electronics consists of the preamplifier module, the power amplifier assembly, the wetside carrier module, and the Traquair electronics stack. The Traquair stack consists of a modem processor module, an ethernet module, and an analog interface module. The power amplifier assembly consists of the power amplifier and its power supply.

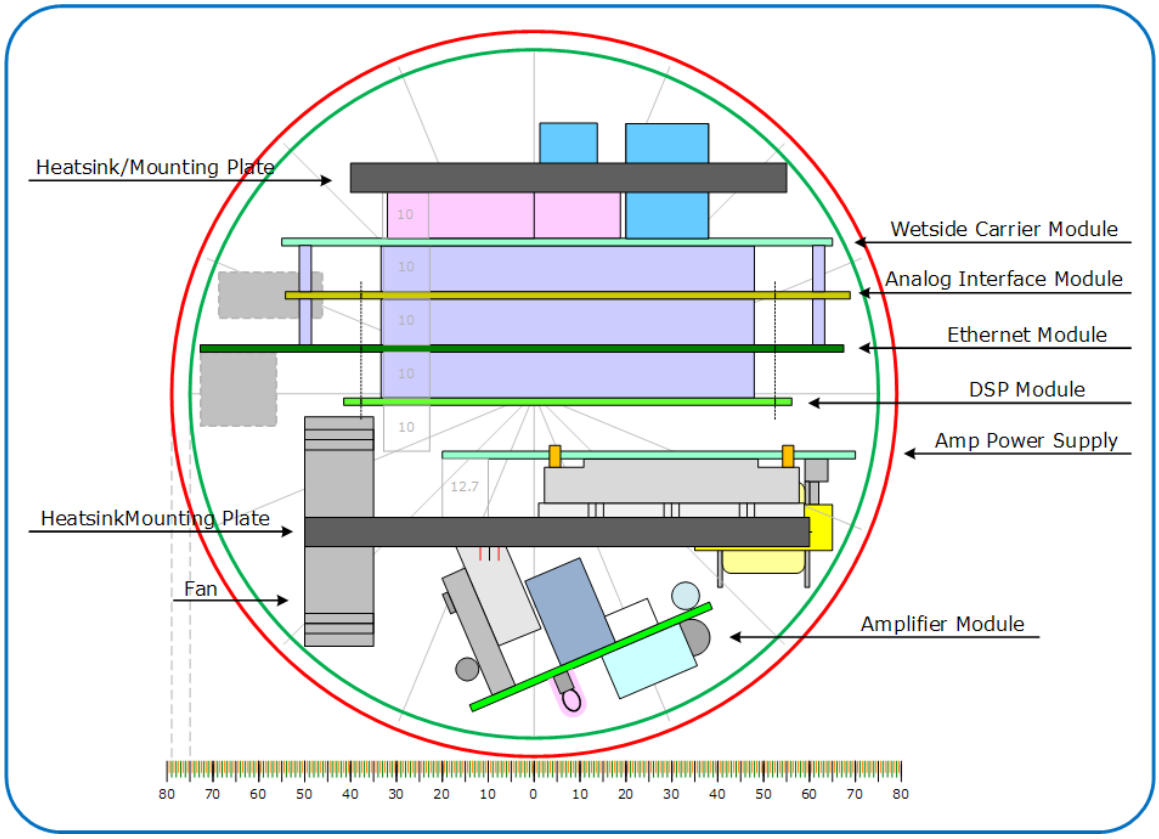

Figure 65: Cross-section of the wetside module electronics.

Wetside Carrier module

A custom motherboard module, developed by EdgeTech, to carry the Traquair micro-line electronics stack, and provide the interfaces and power supplies for the wetside electronics.

Dimensions .. 120 x 86 x 15 mm (preliminary)
DC power input .. 18V to 36V @ 25W
Power outputs
Digital .. 3.3V/3A
Analog .. 12V/500mA
Interfaces

Serial port .. RS-232, RS-422 (preliminary)
Digital inputs .. Opto-isolated (preliminary)
Digital outputs .. Open-drain MOSFET (preliminary)

Preamplifier module

An external preamplifier, developed by FAU, encapsulated in a waterproof housing that connects inline with the transducer cable. This preamplifier greatly improves the receiver signal-to-noise (S/N) ratio.
Dimensions .. 1.25 x 0.5 x 0.5 inches
Power supply .. 3.3V/75mA (filtered analog supply via hydrophone cable)

Amplifier Power Supply module

A custom power supply module, developed by EdgeTech, to supply the linear power amplifier. This amplifier power supply module, with the linear power amplifier and fan, mounted together on a heat transfer plate, make up the power amplifier assembly.
Dimensions .. 80 x 80 x 20 mm (preliminary)
DC power input .. 18V to 36V @ 75W
Power output 48V/1A

Linear Power Amplifier module

A standard EdgeTech linear power amplifier module. This amplifier module, with its power supply module and fan, mounted together on a heat transfer plate, make up the power amplifier assembly.
Dimensions .. 92 x 60 x 36 mm
Power supply .. 48V/1A
Bandwidth .. 50kHz to 500kHz (-3dB)

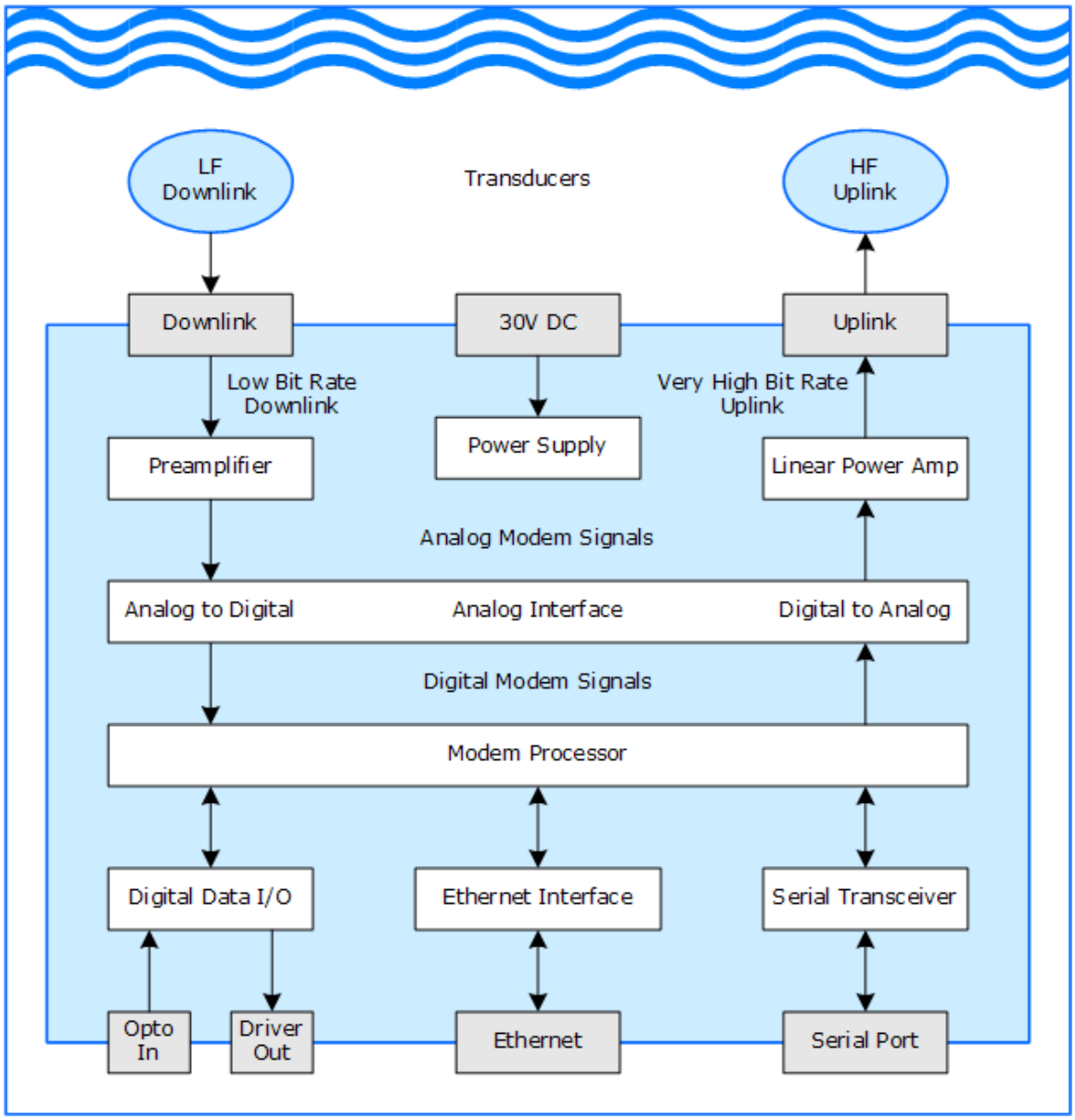

Figure 66: Submersible wetside unit block diagram

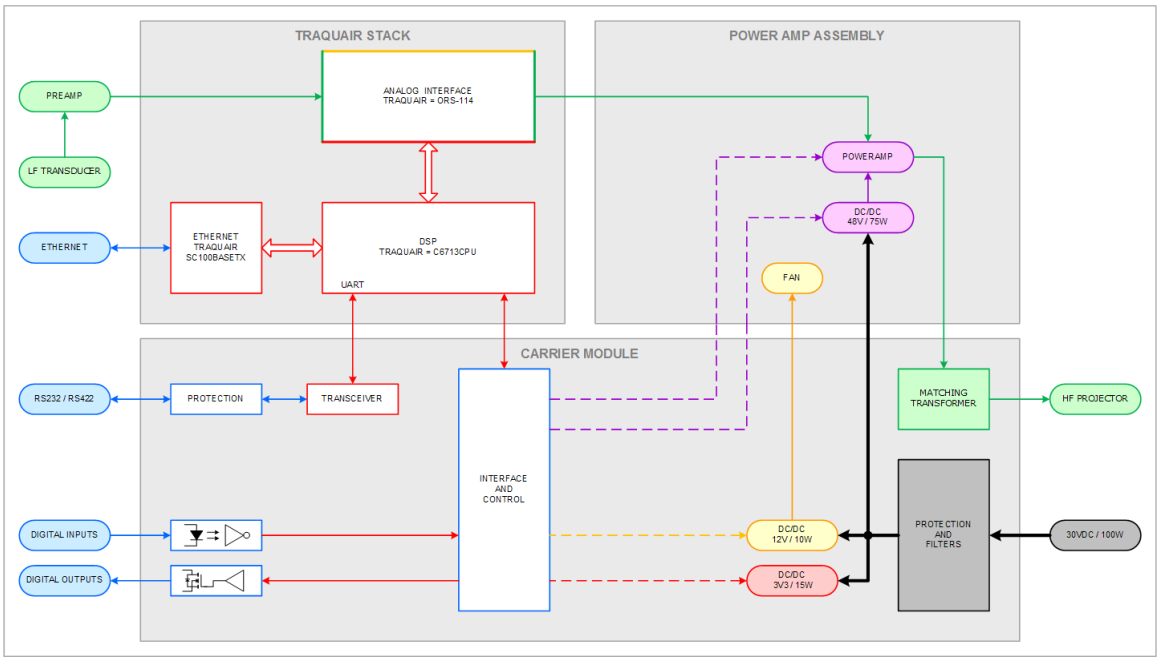

Figure 67: Wetside electronics block diagram

Modem Processor module

A Traquair micro-line C6713CPU/4 DSP module, supplied by Traquair Data Systems, Inc.
Dimensions .. 100 x 68 x 10 mm (stack spacing)
Power supply .. 3.3V/750mA (typical)

The micro-line C6713CPU/4 is a high performance DSP board suitable for high speed data processing:
TMS320C6713 DSP with 256 KB internal fast SRAM, 300Mhz clock (2400 MIPS / 1800 MFLOPS)
Xilinx Spartan 3 FPGA with up to 1M gates
64 MB SDRAM in standard versions and 128 MB on request
2 MB flash memory for non-volatile program, data and FPGA design storage

The C6713CPU/4 module is supplied with a board support package (BSP) that consists of a preinstalled micro-line BusMaster BSP in the FPGA, and a board support library. The development tools are Texas Instruments' Code Composer Studio and XDS510 JTAG emulator/debugger.

Ethernet Interface module

A Traquair micro-line SC100BaseTx module, supplied by Traquair Data Systems, Inc.
Dimensions .. 140 x 68 x 10 mm (stack spacing)
Power supply .. 3.3V/300mA (typical)

The SC100BaseTx module supports full-duplex switched Ethernet at 10/100 Mbps, and is supplied with the bf3Net TCP/IP protocol stack by Windmill Innovations, which is eXpressDSP-compliant.

Analog Interface module

A Traquair micro-line ORS-114 module, supplied by Traquair Data Systems, Inc.
Dimensions .. 123 x 68 x 10 mm (stack spacing)
Power supply .. Digital: 3.3V/500mA (typical); Analog: 12V/100mA (typical)

The ORS-114 module provides a transformer coupled 2-channel A/D converter and a 2-channel D/A converter. These converters are available in 12-bit or 14-bit models. The A/D channels operate simultaneously and independently up to 65 MS/s. The D/A channels operate up to 125 MS/s on each channel. The ORS-114 is supplied with an FPGA logic configuration for the micro-line bus interface.

11. Appendix D - Wetside software architecture

The wetside software consists of the Very High Bit Rate Transmit Modem software, the Low Bit Rate Receive Modem software, and the wetside components of the Modem Driver software.

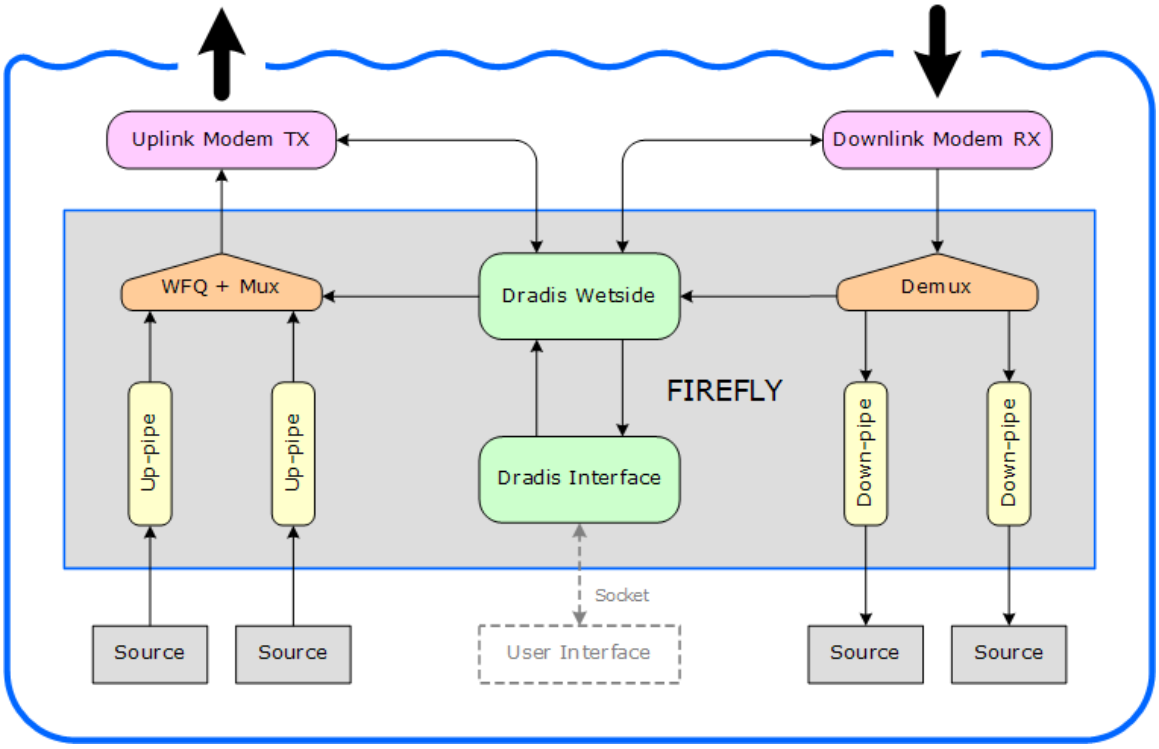

Figure 68: Wetside software architecture

Very High Bit Rate Transmit Modem software

The Very High Bit Rate Transmit Modem software runs on the Modem Processor module. This software multiplexes incoming data streams from multiple wetside sources, and encodes and modulates the data into modem messages. It then outputs the modem messages to the Analog Interface module for analog conversion and transmission.

Low Bit Rate Receive Modem software

The Low Bit Rate Receive Modem software runs on the Modem Processor module. This software detects and synchronizes incoming modem messages, demodulates and decodes them into modem data, and demultiplexes the modem data into multiple topside commands and configuration data streams. It then distributes and applies the commands and configuration data to the modem hardware and software, and to other wetside sources and destinations.

Modem Driver software

The wetside Modem Driver software consists of the wetside portion of the Modem Control software (Dradis) and the Wetside Modem Driver software (Firefly). Dradis forms the underlying control software of the acoustic communications software. Dradis commands are the only way to control the acoustic link. Firefly is configured and controlled by Dradis commands it receives via Glowworm over the acoustic link. These commands typically originate from the User Interface and Display software.

12. Appendix E - Transducers Specifications

12.1 Acoustic Uplink

The very high bit rate uplink topside receiver and wetside receiver use an off-the-shelf model ITC-1089D spherical hydrophone. This hydrophone has a broadband omni-directional receive response, with resonance at about 280 kHz. To improve the receive SNR, an external preamplifier was developed and deployed in line with the hydrophone cable.

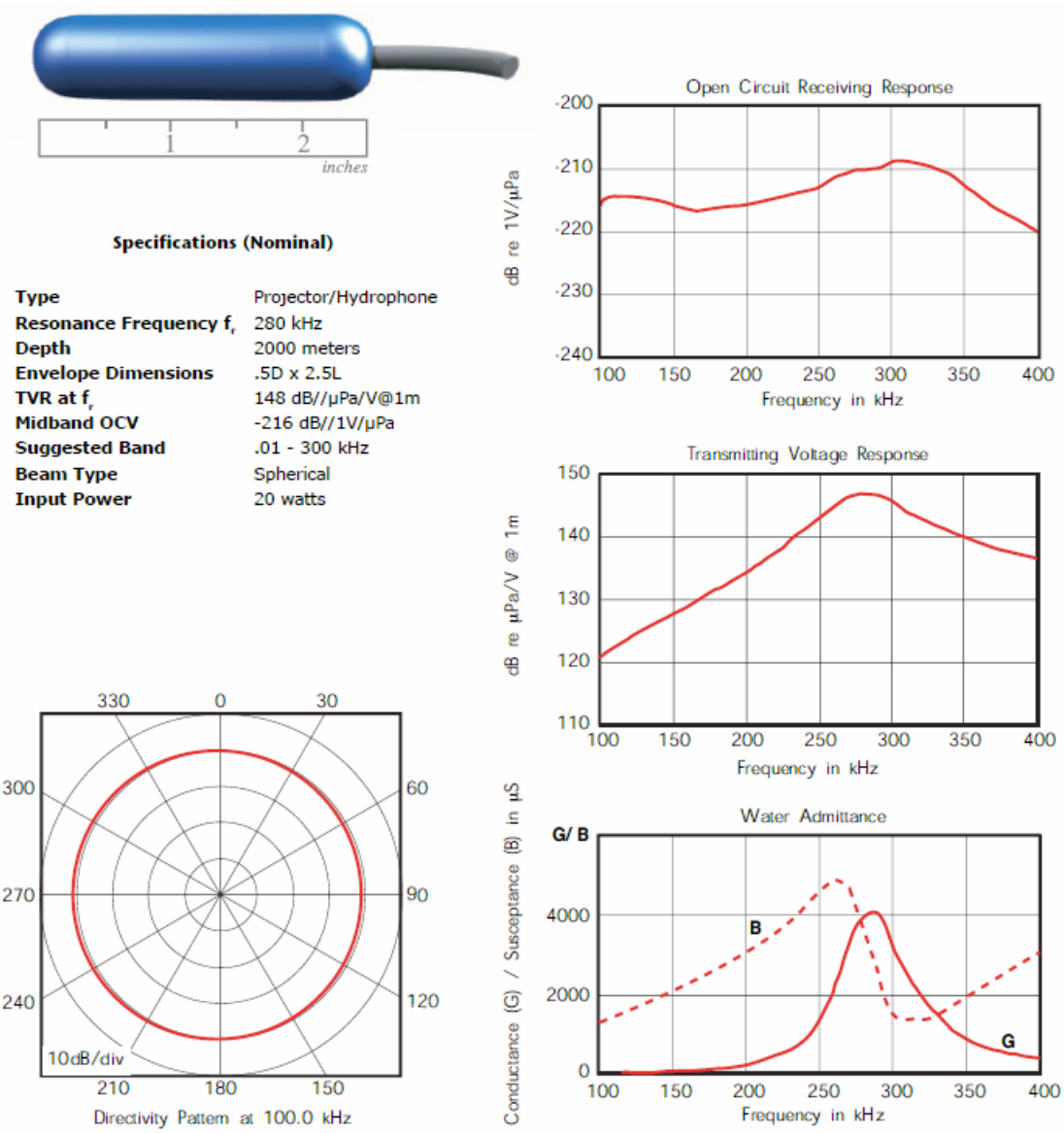

Figure 69: ITC-1089D Hydrophone

12.2 Acoustic Downlink Topside and Wetside Transducers

The acoustic downlink uses identical topside and underwater transducers: off-the-shelf model ITC-1042 spherical transducers. These transducers have a broadband omni-directional transmit/receive response, with resonance at about 80 kHz.

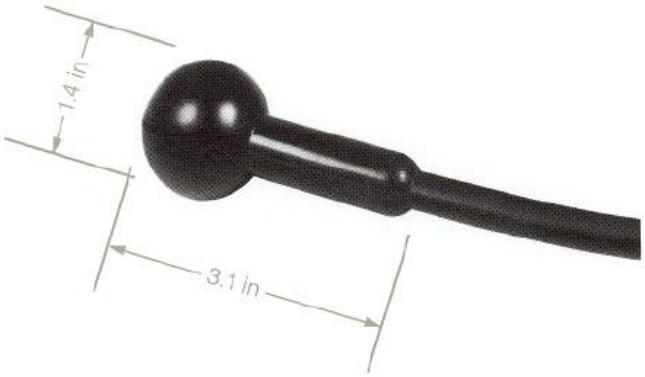

Resonance Frequency. ~80 kHz
Operating Frequency.
Receiving.(see graph)
Usable Receiving Frequency Range. 1 Hz - 120 kHz
Transmitting. (see graph)
Admittance. (see graph)
Beam Pattern.
Horizontal. omni ± 0.5 dB to 80 kHz
Vertical. omni ± 1.5 dB to 80 kHz
Efficiency. 50 kHz to 100 kHz (50% minimum) at resonance = 70%
Input Power. 100 watts (around resonance at <10% D.C.).
Operating Depth. to 4,000 feet
Cable. DSS-2 (10 ft.)
Weight (water). ~1.2 lbs.
Weight (air). ~2.2 lbs.

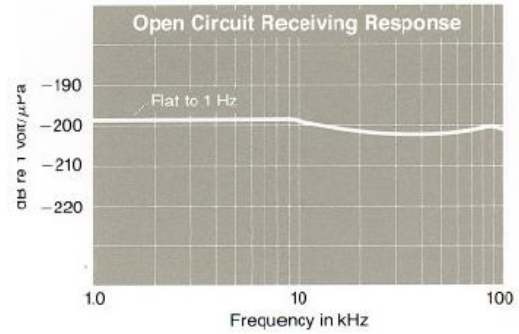

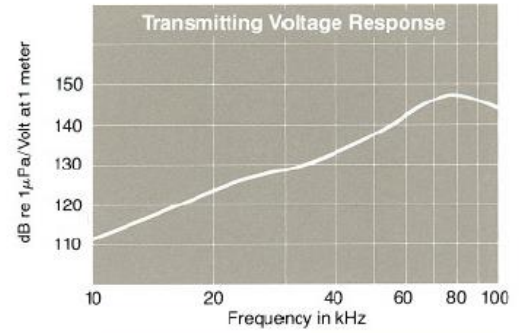

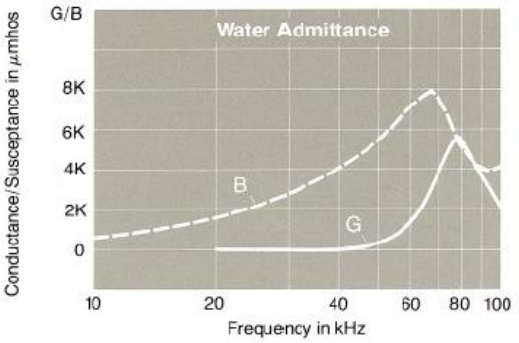

Figure 70: ITC-1042 Transducer